Evaluation and improvement of the single diode model's parameters used for solar PV modelling

by

Pieter Johannes Johnson Botha

Thesis presented in partial fulfilment of the requirements for the degree of Master of Engineering (Electical and Electronic) in the Faculty of Engineering at Stellenbosch University

Department of Electrical and Electronical Engineering,
University of Stellenbosch,
Private Bag X1, Matieland 7602, South Africa.

Supervisor: Dr. Arnold Johan Rix

December 2017

Declaration

By submitting this thesis electronically, I declare that the entirety of the work contained therein is my own, original work, that I am the sole author thereof (save to the extent explicitly otherwise stated), that reproduction and publication thereof by Stellenbosch University will not infringe any third party rights and that I have not previously in its entirety or in part submitted it for obtaining any qualification.

Date: December 2017

Abstract

Evaluation and improvement of the single diode model's parameters used for solar PV modelling

PJJ. Botha

Department of Electrical and Electronical Engineering,
University of Stellenbosch,
Private Bag X1, Matieland 7602, South Africa.

Thesis: MEng (Electrical and Electronic)

September 2017

Solar photovoltaics are one of the leading renewable energy generators that are being installed in South Africa. The understanding of how this technology works and how it responds to radiation, is important. This thesis evaluates the different parameters that influence the performance of a solar cell. The parameter extraction method is of interest as it tells the story of what is happening internally in a solar cell when subjected to environmental conditions. The response of the cell to certain light is part of this study to evaluate the influence of different light and how it relates to the testing condition on the data sheet of the solar module.

The solar cell parameters of the single diode equivalent circuit model are studied. The data originate from a testing facility in the Northern Cape. The data were examined to extract the five parameters from the current voltage curve, measured in 10 minute intervals on the site. The parameter extraction method of De Soto is presented and implemented to compare the induced errors made with this method. The error was an overestimation of 13.71% in the maximum power point. The evaluation of the error resulted in an observation of a linear error with regards to temperature and irradiance. The output of the method was adjusted with a function to result in an improvement of a percentage error of -2.99%. The adjustment function was optimised and the error in extracting the maximum power point was reduced to only -0.062%. The individual parameters are examined and adjusted, to present five new equations for the parameter extraction that are developed from De Soto's method. The new equations have shown an increase in parameter accuracy. When the new parameter extraction equations are used together, the maximum power point error is -1.73%.

An automated spectrum and solar module performance monitoring system was developed. The system measures the current voltage curve from the solar module with the solar spectrum at an interval of 10 minutes. The data are stored on a local and web-based database for analysis. The data were firstly analysed in the different bands of wavelength

that each colour in the spectrum occupies. This has shown that red light is the dominant colour in the spectrum that was measured. The relationship between the average photon energy and the current and voltage of the module are examined and have shown that the voltage is high regardless of the amount of energy, as long as there is direct sunlight on the module. The current increases as the average photon energy quantification parameter increases.

From this study it is evident that the spectrum also plays a role in the modelling of photovoltaics, especially when the conditions are not standard test conditions. The solar spectrum can change considerably and it is important to take it into consideration when accurate modelling of photovoltaics is conducted.

Uittreksel

Evaluering en verbetering van die enkel diode model se parameters wat gebruik word vir sonkrag FV modellering

("Evaluation and improvement of the single diode model's parameters used for solar PV modelling")

PJJ. Botha

Departement Elektries en Elektroniese Ingenieurswese,
Universiteit van Stellenbosch,
Privaatsak X1, Matieland 7602, Suid Afrika.

Tesis: MIng (Elektries en Elektronies)

September 2017

Son fotovoltaïese tegnologie is een van die gewildste hernubare energie opwekkers wat tans in Suid-Afrika geïnstalleer word. Dit is belangrik om te verstaan hoe hierdie tegnologie werk en hoe dit op bestraling reageer. Hierdie tesis ondersoek die verskillende parameters wat die prestasie van 'n sonsel beïnvloed. Die parameter ekstraksie metode is van belang, aangesien dit verduidelik wat binne-in 'n sonsel aangaan wanneer dit blootgestel word aan verskeie omgewingstoestande. Deel van die studie is om die invloed van verskillende lig en die verband daarvan met betrekking tot standaard toets toestande, op die sonpaneel se data blad, te evalueer.

Die enkeldiode ekwivalente stroombaanmodel se parameters word bestudeer. Die data is afkomstig van 'n toetsfasiliteit in die Noord-Kaap. Die data is ondersoek om vyf parameters van die stroom-spanningskurwe, wat in 10 minute intervalle op die perseel gemeet word, te onttrek. De Soto se parameter ekstraksie metode word voorgelê en toegepas om die foute wat hierdie metode maak, te ondersoek. Die metode bied 'n oorskatting van 13.71% van die maksimum drywingspunt. Toe die fout ondersoek is, is 'n lineêre fout ten opsigte van die temperatuur en bestraling gevind. Die metode se uittree is met 'n funksie aangepas, wat tot 'n verbetering van 'n $-2,99\%$ fout gelei het. Die aanpassingsfunksie is geoptimeer en die fout van die maksimum drywingspunt is verminder na slegs -0.062%. Die individuele parameters is ondersoek en aangepas om vyf nuwe vergelykings vir die parameter ekstraksie te bied wat van De Soto se metode ontwikkel word. Die nuwe vergelykings toon 'n toename in akkuraatheid. As die nuwe parameter ekstraksie vergelykings saam gebruik word, is die fout van die maksimum drywingspunt -1.73%.

'n Geoutomatiseerde spektrum en sonpaneel prestasie moniteringstelsel is ontwikkel. Die stelsel meet die stroom-spanningskurwe van die sonpaneel in 10 minute intervalle. Die data word op 'n plaaslike en web-gebaseerde databasis gestoor vir analise. Die data is eerstens

in verskillende bande golflengtes van elke kleur in die spektrum ontleed. Dit het getoon dat rooi lig die dominante kleur in die gemeetde spektrum is. Die verhouding tussen die gemiddelde fotonenergie en die stroom en spanning van die sonpaneel is ondersoek en het aangetoon dat die spanning hoog is, ongeag die hoeveelheid energie, mits daar direkte sonlig op die sonpaneel skyn. Die stroom neem toe soos die gemiddelde fotonenergie kwantifisering parameter toeneem.

Dit is duidelik dat die spektrum ook 'n rol speel in fotovoltaïese modellering, veral as die toestande nie standaard toets toestande is nie. Die sonspektrum kan aansienlik verander en daarom is dit belangrik om dit in ag te neem as akkurate fotovoltaïese modellering gedoen word.

Acknowledgements

Foremost, I would like to thank my thesis supervisor Dr. Arnold Johan Rix of the Electrical and Electronic Engineering faculty at Stellenbosch University. He consistently allowed this thesis to be my own work, but steered me in the right direction whenever he thought I needed it. He believed in my abilities when my motivation to work further and harder was low.

This work would not have been possible without the financial support from Scatec Solar.

I would also like to thank the engineering experts who worked with me and with whom I shared an office with: Armand du Plessis, Brian de Beer, Carmen Lewis, Tafadzwa Gurupira and Tashriq Pandy. Without their passionate advice and input, this thesis could not have been a success. Coffee breaks, which always lasted too long, and the Friday beers made difficult times better.

I must express my very profound gratitude to my parents, Gerhard and Sanet, to my brothers, Wihan and Leon, and sisters, Anjali and Marihanca, whose love and guidance are with me in everything I pursue. Their continuous encouragement throughout my years of study and through the process of researching and writing this thesis. It would not have been possible without them.

I would like to thank Corné van Graan for her unconditional love and motivation throughout this thesis. Without your encouragement and ideas only half of this thesis would have been done by this time.

Last but not the least, above all, God for Your spiritual guidance and the path I walked with You to grow in every aspect of life through this year.

Author

John-Pieter Botha

Dedications

This thesis is dedicated to my parents, Gerhard and Sanet Botha.

Contents

Declaration i

Abstract ii

Uittreksel iv

Acknowledgements vi

Dedications vii

Contents viii

List of Figures xii

List of Tables xvi

Nomenclature xvii

1 Introduction 1
- 1.1 Background . . . 1
  - 1.1.1 History of photovoltaics . . . 1
  - 1.1.2 Why photovoltaics . . . 2
  - 1.1.3 Photovoltaics in the world . . . 2
  - 1.1.4 Photovoltaics in South Africa . . . 3
- 1.2 Problem Statement . . . 4
  - 1.2.1 Objectives and Goals . . . 5
- 1.3 Thesis Outline . . . 6
  - 1.3.1 Chapter 2 . . . 7
  - 1.3.2 Chapter 3 . . . 7
  - 1.3.3 Chapter 4 . . . 7
  - 1.3.4 Chapter 5 . . . 7

2 Fundamental Background 8
- 2.1 The Sun . . . 8
  - 2.1.1 Earth's Orbit . . . 8
  - 2.1.2 Solar Angles . . . 9
  - 2.1.3 Sun's Position . . . 11
- 2.2 Solar Spectrum . . . 12
  - 2.2.1 Irradiance . . . 12
  - 2.2.2 Air Mass (AM) . . . 13

2.2.3 Radiation . . . 16
2.3 Photovoltaic Effect and Models . . . 19
2.3.1 Photovoltaic Effect . . . 19
2.3.2 Basic Single Diode Model . . . 20
2.3.3 Single Diode Model . . . 21
2.3.4 Double Diode Model . . . 23
2.4 Current-Voltage (IV)-Curve . . . 23
2.4.1 Maximum Power Point (MPP) . . . 23
2.4.2 Temperature Impact . . . 24
2.4.3 Irradiance Impact . . . 25
2.4.4 Parasitic Resistances . . . 26
2.4.5 Fill Factor . . . 28
2.4.6 Summary . . . 29

3 Solar PV Parameter Extraction and Parameter Evaluation 30
3.1 Introduction . . . 30
3.2 Location . . . 31
3.2.1 Facility . . . 31
3.2.2 Climate and Weather . . . 31
3.3 Hardware . . . 32
3.3.1 Solar Module . . . 32
3.3.2 Active Load . . . 34
3.3.3 Weather Data . . . 35
3.3.4 Communication . . . 37
3.3.5 System Integration . . . 37
3.4 Software . . . 38
3.4.1 SQL Language . . . 38
3.4.2 Python Language . . . 39
3.4.3 Query execution function . . . 39
3.4.4 General Computation . . . 40
3.5 Parameter Extraction and Optimisation . . . 40
3.5.1 Parameter Extraction Method . . . 41
3.5.2 Approximation . . . 42
3.5.3 Optimisation . . . 43
3.5.4 Implementation . . . 43
3.5.5 Extraction Result . . . 45
3.6 De Soto's Parameter Extraction and Prediction . . . 45
3.6.1 Parameter Extraction Model . . . 45
3.6.2 Implementation of De Soto's Method . . . 45
3.6.3 Parameter Comparison . . . 47
3.7 Parameter Extraction Results . . . 48
3.7.1 Error Adjustment . . . 51
3.7.2 Adjustment Optimisation . . . 52
3.7.3 Verification Study . . . 53
3.8 Individual Parameters . . . 54
3.8.1 Error Calculation . . . 54
3.8.2 Series Resistance . . . 55
3.8.3 Shunt Resistance . . . 58

3.8.4 Photo Current . . . 61
3.8.5 Diode Saturation Current . . . 65
3.8.6 Ideality Factor . . . 66
3.8.7 New Parameter Equation Set . . . 69
3.8.8 Total Performance Influence . . . 70
3.9 Summary . . . 71

4 Automated Spectrum Data Acquisition and Analysis 72
4.1 Introduction . . . 72
4.1.1 Spectral Response . . . 72
4.1.2 Quantum Efficiency . . . 73
4.1.3 Spectral Evaluation . . . 74
4.1.4 Spectral Conversion Efficiency . . . 76
4.2 Location of the Measuring Set-up . . . 76
4.2.1 Facility . . . 76
4.2.2 Shading Analysis . . . 78
4.2.3 Weather . . . 79
4.2.4 SAURAN - External Data . . . 80
4.3 Hardware Utilisation and Design . . . 80
4.3.1 Spectrometer . . . 80
4.3.2 Active Load . . . 81
4.3.3 Communication Breakout Board - RS485 . . . 81
4.3.4 Shutter . . . 83
4.3.5 Data Server . . . 84
4.3.6 Raspberry Pi (RPi) . . . 85
4.3.7 System Integration . . . 85
4.4 Software . . . 86
4.4.1 Controlling Software . . . 86
4.4.2 Graphical User Interface . . . 90
4.4.3 Database . . . 94
4.4.4 Server . . . 94
4.5 Data Validation . . . 95
4.5.1 Calibration File . . . 95
4.5.2 Data Conversion . . . 96
4.5.3 Measured Data Categorisation . . . 97
4.5.4 AM1.5G Comparison . . . 97
4.5.5 SAURAN Comparison . . . 98
4.6 Data Analysis . . . 99
4.6.1 Colour Analysis . . . 99
4.6.2 Average Photon Energy . . . 104
4.6.3 Temperature analysis of a clear day . . . 106
4.6.4 Bypass diode observation . . . 107
4.7 Summary . . . 109

5 Conclusion 110
5.1 Parameter extraction . . . 110
5.1.1 Conclusion and remarks . . . 110
5.1.2 Problems and possible improvements . . . 111
5.2 Spectral analysis . . . 111

5.2.1 Conclusion and remarks 111
5.2.2 Problems and possible improvements 112

Appendices **113**

A Spectrometer Bracket Design **114**

B RAID1 Set-up Guide **117**
B.1 Introduction 117
B.2 RAID1 Set-up Guide 117
B.2.1 Step 1 117
B.2.2 Step 2 117
B.2.3 Step 3 118
B.2.4 Step 4 118
B.2.5 Step 5 118
B.3 RAID Status 118

List of References **120**

List of Figures

1.1 Latest solar cell technologies and their efficiencies [53] . . . 2
1.2 Cumulative capacity of grouped regions in 2015 [4] . . . 3
1.3 Cumulative capacity of South Africa in 2016 . . . 4
1.4 REIPPPP bidding round prices per kW in South Africa [44] . . . 4

2.1 The tilt of the earth's rotation axis on the Elliptical plane . . . 9
2.2 Declination angles of the sun throughout the year . . . 10
2.3 Altitude, declination and zenith angle of the sun at solar noon . . . 11
2.4 The position of the sun illustrated . . . 12
2.5 Irradiance differentiated rays . . . 13
2.6 AM0, AM1.5 Global and AM1.5 Direct spectrum . . . 14
2.7 Explanation of air mass ratio calculation . . . 15
2.8 Absorption and scattered sunlight radiation for a typical AM1.5 global . . . 16
2.9 AM0 and the black-body radiation . . . 18
2.10 Colour bands on the black-body radiation spectrum . . . 19
2.11 Photovoltaic effect in a solar cell. . . . 20
2.12 Basic solar cell equivalent circuit . . . 21
2.13 Single diode equivalent circuit model . . . 22
2.14 Double diode equivalent circuit model . . . 23
2.15 The impact on the IV-curve of temperature . . . 25
2.16 The impact of irradiance on the IV-curve . . . 26
2.17 The impact on the IV-curve due to series resistance . . . 27
2.18 The impact on the IV-curve due to shunt resistance . . . 28
2.19 Fill factor graphical explanation . . . 28

3.1 Air photo showing the research facility. Photo: Kurt Krog . . . 31
3.2 Active load installed in an electric box at the research facility . . . 35
3.3 Met One-485 weather station and Met One-372-series precipitation gauge . . . 36
3.4 Kipp and Zonen SMP10 pyranometer fixed on the POA . . . 37
3.5 The research facility's system integration . . . 38
3.6 Database execution function flow diagram . . . 40
3.7 Initial parameter approximation from the measured data . . . 43
3.8 Software flowchart of the parameter extraction method . . . 44
3.9 Flow diagram of the implementation of De Soto's method . . . 47
3.10 Comparison between De Soto's method and the measured data at different irradiance and temperature conditions . . . 48
3.11 Histogram of the percentage error De Soto's method makes to measured data . 49
3.12 Influence on the percentage error with temperature . . . 50
3.13 Influence on the percentage error with varying irradiance . . . 50

3.14 3D curve fitting with Matlab 51
3.15 Histogram of the percentage error after the adjustment function is applied to De Soto's method 52
3.16 Percentage error of De Soto's method compared to the error in the adjustment to the method 53
3.17 Comparison of the day's power with different methods 54
3.18 The relationship between the actual series resistance and De Soto's method evaluated with varying temperature 55
3.19 The relationship between the actual series resistance and De Soto's method evaluated with varying irradiance 56
3.20 The relationship between the actual series resistance and the improvement on De Soto's method evaluated with varying temperature 57
3.21 The relationship between the actual series resistance and the improvement on De Soto's method evaluated with varying irradiance 57
3.22 Histogram of the percentage error De Soto's method makes to the actual power, compared to the new series resistance parameter relationship 58
3.23 The relationship between the actual shunt resistance and De Soto's method evaluated with varying temperature 59
3.24 The relationship between the actual shunt resistance and De Soto's method evaluated with varying irradiance 59
3.25 The relationship between the actual shunt resistance and the improvement on De Soto's method evaluated with varying temperature 60
3.26 The new relationship between the actual shunt resistance and the improvement on De Soto's method evaluated with varying irradiance 60
3.27 Histogram of the percentage error De Soto makes to the actual power compared to the new shunt resistance parameter relationship 61
3.28 The relationship between the actual photo current and De Soto's method evaluated with varying temperature 62
3.29 The relationship between the actual photo current and De Soto's method evaluated with varying irradiance 62
3.30 The relationship between the actual photo current and the improvement on De Soto's method evaluated with varying temperature 63
3.31 The relationship between the actual photo current and the improvement on De Soto's method evaluated with varying irradiance 64
3.32 Histogram of the percentage error De Soto makes to the actual power compared to the new parameter relationship 65
3.33 The relationship between the actual output current and De Soto's method evaluated with varying temperature 66
3.34 The relationship between the actual output current and De Soto's method evaluated with varying irradiance 66
3.35 The relationship between the actual ideality factor and De Soto's method evaluated with varying temperature 67
3.36 The relationship between the actual ideality factor and De Soto's method evaluated with varying irradiance 67
3.37 The relationship between the actual ideality factor and the improvement on De Soto's method evaluated with varying temperature 68
3.38 The new relationship between the actual ideality factor and the improvement on De Soto's method evaluated with varying irradiance 68

3.39 Histogram of the percentage error De Soto makes to the actual power compared evaluated with the new ideality factor parameter relationship 69
3.40 Total improvement with the new parameter equations used 70

4.1 Spectral Response of a polycrystalline silicon solar module 73
4.2 Quantum Efficiency calculated from the Spectral Response 74
4.3 Photo of the testing facility and set-up 77
4.4 A Google Maps satellite photo with the sun's path at the facility at the beginning of July 78
4.5 Shading analysis of the surroundings of the measuring equipment 79
4.6 First concept of the receptor bracket and how it connects to the solar module 81
4.7 Schematic layout of the RS485 breakout board for the Raspberry Pi 82
4.8 Photo of the breakout board on the Raspberry Pi and the PCB layout 82
4.9 Solenoid shutter concept without fixing bracket 83
4.10 Servo shutter concept attached to the solar module 84
4.11 Raid Set-up diagram 85
4.12 System Set-up 86
4.13 Main software Python script flow diagram 87
4.14 Servo controlling software flow diagram 88
4.15 "*db_execute*" function software flow diagram 89
4.16 Saturated spectrum measurement against AM1.5 global 90
4.17 Flow diagram of the GUI software 91
4.18 Screen-shot of Spectral Counts GUI 92
4.19 Screen-shot of Spectral Irradiance GUI 93
4.20 Screen-shot of Webmin server management software and specifications 94
4.21 Plot of the calibration file of the spectrometer and the band of spectra used in this study 96
4.22 Categorisation of the times of data measured thought out the measuring period 97
4.23 Comparison between the AM1.5 global spectrum and a measurement taken . . 98
4.24 Comparison between the measured integrated spectrum and SAURAN's irradiance data 99
4.25 Spectrum colour divisions 100
4.26 Spectrum colour divisions Pi diagram 100
4.27 Percentage colour throughout the clear sky day 101
4.28 Percentage colour throughout the overcast sky day 101
4.29 Percentage ultra-violet and infra-red light throughout the clear sky day 102
4.30 Percentage ultra-violet and infra-red light throughout the overcast sky day . . 102
4.31 Blue light band percentage in the spectrum 103
4.32 Red light band percentage in the spectrum 103
4.33 Green light band percentage in the spectrum 103
4.34 Yellow light band percentage in the spectrum 103
4.35 Orange light band percentage in the spectrum 103
4.36 Violet light band percentage in the spectrum 103
4.37 Ultra-Violet light band percentage in the spectrum 104
4.38 Infra-Red light band percentage in the spectrum 104
4.39 APE of clear days in the data 105
4.40 APE of cloudy days in the data 105
4.41 APE of a clear day compared to the produced current 106

4.42 APE of a clear day compared to the produced voltage 106
4.43 Temperature analysis of a full day 107
4.44 IV-curve of shading on the solar module 107
4.45 Possible shading on the solar module 108

B.1 Command-line output for the RAID1 server for "cat /proc/mdstat" 119
B.2 Photo of the server hardware 119

List of Tables

2.1 Visible Spectrum 18

3.1 Historical Weather at the research facility 32
3.2 Electrical and influential characteristics of the Renesola VirtusII. 33
3.3 Mechanical characteristics of the Renesola VirtusII. 34
3.4 Active load specifications 34
3.5 Single Diode Model's Reference Parameters 46
3.6 Comparison 53

4.1 Electrical and influential characteristics of the Solairedirect SD Eco Plus. . . . 77
4.2 Components used in the RS485 breakout board 83
4.3 CYS S0009 Analog Servo Specifications 84
4.4 Login parameters for the database 88
4.5 Day's data that are measured and used in the study 95
4.6 Percentage of colour represented in the spectrum of AM1.5 global 100

Nomenclature

Constants

$q =$ $1.602 \times 10^{-19}\,\mathrm{C}$ (Elementary Charge)

$k =$ $1.381 \times 10^{-23}\,\mathrm{J/K}$ (Boltzmann's Constant)

$\sigma =$ $5.670 \times 10^{-8}\,\mathrm{Wm^{-2}K^{-4}}$ (Stefan-Boltzmann Constant)

Variables

I_{MPP}	Current at Maximum Power Point	[A]
δ	Declination Angle	[°]
I_D	Diode Current	[A]
a	Diode Ideality Factor	[ ]
I_O	Diode Reverse Saturation Current	[A]
ϵ	Electron Band-gap Voltage	[V]
H	Hour Angle	[°]
n	Ideality Factor	[ ]
G_{STC}	Irradiance at Standard Test Conditions	[W/m^2]
G	Irradiance	[W/m^2]
L	Latitude Angle	[°]
N_S	Number of cells in Series	[ ]
V_{OC}	Open Circuit Voltage	[V]
I_{PH}	Photo Current	[A]
E_λ	Photon Energy	[J/s]
G_{POA}	Plane of Array Irradiance	[W/m^2]
P_{MPP}	Power at Maximum Power Point	[W]
R_S	Series Resistance	[Ω]
I_{SC}	Short Circuit Current	[A]
I_{SH}	Shunt Resistance Current	[A]

R_{SH}	Shunt Resistance	[Ω]
β	Sun Altitude Angle	[°]
ϕ_S	Sun Azimuth Angle	[°]
T_C	Solar Cell's Temperature	[°C]
T_{STC}	Temperature at Standard Test Conditions	[°C]
V_T	Thermal Voltage	[V]
V_{MPP}	Voltage at Maximum Power Point	[V]
W	Watt	[W]
λ	Wavelength	[nm]

Abbreviations

ABS	Acrylonitrile Butadiene Styrene
AM	Air Mass
AC	Alternating Current
AOI	Angle of Incidence
IV	Current Voltage
DS	Dark Spectrum
DB	Database
DHI	Diffuse Horisontal Irradiance
DC	Direct Current
DNI	Direct Normal Irradiance
FF	Fill Factor
$GPIO$	General Purpose Input Output
GW	Giga-Watt
GHI	Global Horisontal Irradiance
MPP	Maximum Power Point
MW	Mega-Watt
MMF	Mismatching Factor
$NOCT$	Nominal Operating Cell Temperature
OS	Operating System
PV	Photovoltaic
PWM	Pulse Width Modulation

POA Plan of Array

$pc - Si$ Polycrystalline Silicon

PCB Printed Circuit Board

QE Quantum Efficiency

RAM Random Access Memory

RPi Raspberry Pi

$RAID$ Redundant Array of Independent Disks

$SATA$ Serial AT Attachment

SPI Serial Peripheral Interface

SDK Software Development Kit

SI Spectral Irradiance

STC Standard Test Conditions

SQL Structured Query Language

TSI Total Solar Irradiance

$UART$ Universal Asynchronous Receiver Transmitter

USB Universal Serial Bus

UF Useful Fraction

Chapter 1

Introduction

1.1 Background

In this section the background of photovoltaics is discussed. The section will look at where PV began, what their future looks like globally and in South Africa. The importance of PV is discussed, focusing on its benefits to renewable energy. The research goals and outcomes, with a summary of each chapter, follow after the background.

1.1.1 History of photovoltaics

Photovoltaic technology dates back to the 18th century, where Alexandre Edmond Becquerel, as nineteen year old physicist from France, observed the phenomenon of light to electricity conversion in 1839. Over forty years later, Charles Fritts, described the first solar cells that were made from Selenium wafers in 1883. The first patent for the solar cell was awarded to Edward Weston in 1888. In 1901, the well known scientist, Nikola Tesla, received the US patent for the "method of utilising and apparatus for the utilisation of radiant energy". Early in the 19th century Albert Einstein and Robert Millikan worked together to provide the experimental proof of the photovoltaic effect that Einstein published with his paper on relativity theory [6].

Commercial solar cells were developed by Bell Laboratories in 1954. They discovered that Silicon has photoelectric properties and achieved a 6 % efficiency. The first primary use of solar cells were for satellites. Japan developed Silicon solar cell arrays and launched multiple research and development projects in the 1970's [21]. In 1990 Germany and Japan subsidised programs to speed up the adoption of the technology and the efficiencies of solar cells increased to 20 %.

That brought us to the efficiencies of recent years that reached 46 % for multi-junction concentrator solar cells in the constantly growing technology field [3]. The different technologies and their latest efficiencies are shown in Figure 1.1 [53].

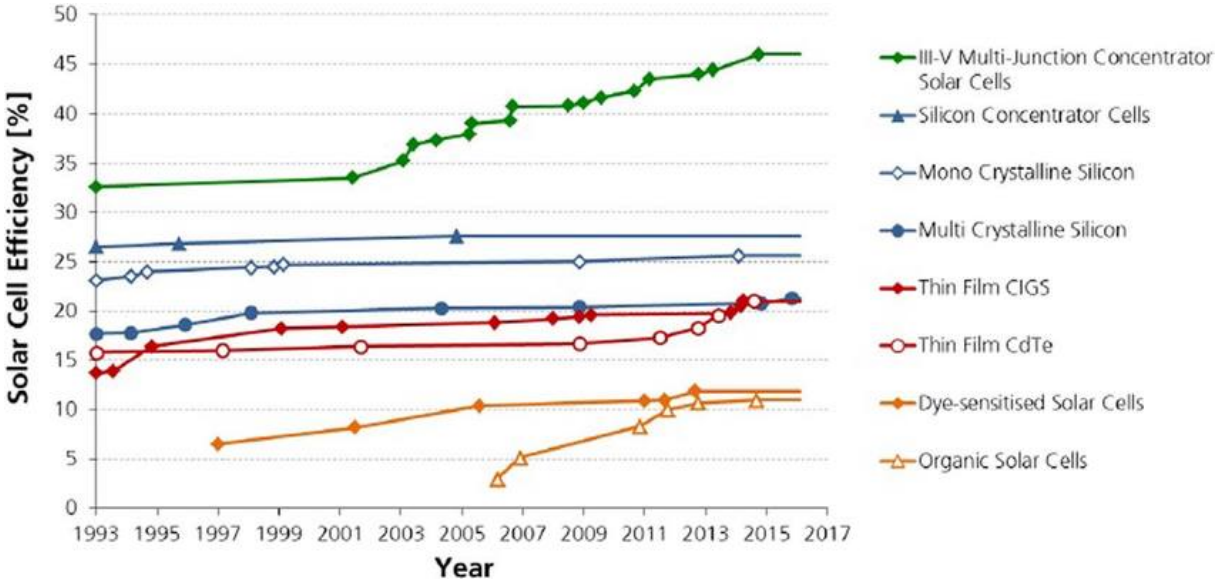

Figure 1.1: Latest solar cell technologies and their efficiencies [53]

1.1.2 Why photovoltaics

Sustainable energy is the field that stakeholders, governments, utilities and consumers are pushing toward. Photovoltaics have the important characteristics that will enable the shift from ineffective, insufficient and costly energy systems to a more sustainable energy system [32]. There are different motivations and arguments of why the shift towards sustainable and renewable energy is beneficial to all, and some of these motivations and arguments are listed below [32]:

- Avoidance of scarce fossil fuel resources and volatility of the fuel price.
- Greenhouse gas emission reduction for environmental benefits.
- Cost reduction benefits by using the local supply chain and labour markets.
- Electric utility benefits by decentralising the energy supply and to avoid peak power generation which is costly.
- Economic and domestic growth with the establishment of employment.
- Customer benefits through the green pricing programmes and the green characteristics.

1.1.3 Photovoltaics in the world

The growth of photovoltaics increased exponentially in the recent decade. Worldwide feed-in tariff programmes were launched by governments to give economic incentives for possible investors in the promising renewable energy field. At the end of 2016 the total global installed solar capacity reached 303 GW [64]. China is currently the world leader in the greatest amount of solar energy produce with a capacity of about 70 GW. A cumulative capacity of grouped regions in megawatts is shown in Figure 1.2, redrawn from [4].

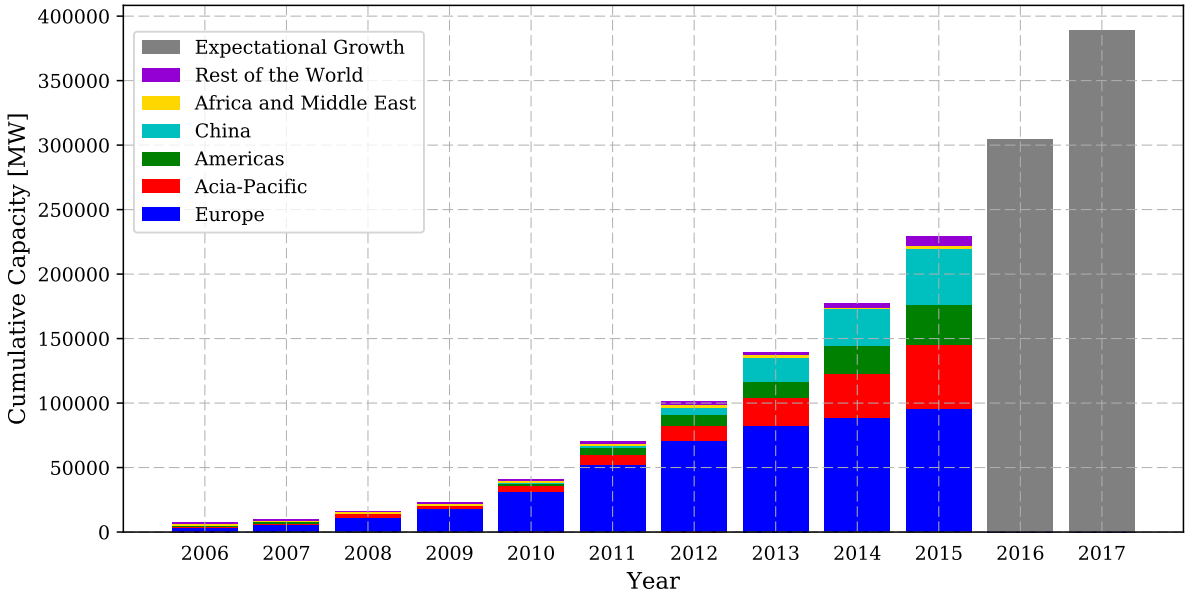

Figure 1.2: Cumulative capacity of grouped regions in 2015 [4]

The outlook for 2020 is promising as it is expected that the world leaders, after China which is first with 100 GW , Germany, Japan and the United States would each contribute between 50 and 60 Gigawatt of power. This would set the global installed solar capacity between 396 and 540 Gigawatt. That will approximately be equivalent to 2.2 % of the global power generation at that time [58].

The average price per watt of solar cells dropped drastically, with a drop of 21 000 % over the last 40 years. The trend of the price of solar cells is supported by Swanson's Law, which says that the price per watt will decrease with 20 % for every doubling of the cumulative photovoltaic production [12].

1.1.4 Photovoltaics in South Africa

South Africa has an average of more than 2 500 hours of sunshine per year. The 24 hours global solar irradiance average per year is 220 w/m^2 in South Africa. This is more than double the average of Europe at 100 W/m^2. There is no doubt that South Africa is one of the highest solar resource rich countries in the world [4].

South Africa's Renewable Energy Independent Power Producer Procurement (REIPPP) programme is a pilot programme that was developed to encourage investors to invest in the development of renewable energy within South Africa. The government set a target for 2020, which states that they will purchase 10% of its electricity from renewable sources [5]. There are multiple big investors that support this programme by installing 75 Megawatt solar plants. The cumulative installed solar power capacity of South Africa of the past few years is shown in Figure 1.3. One of the first plants is the Kalkbult solar power plant which was one of the projects that were awarded in the first bidding round of the REIPPP programme. It was completed three months ahead of schedule in a record time of 9 months. It was commissioned in September 2013. The data used in this thesis is from the testing facility located within the perimeter of this solar plant.

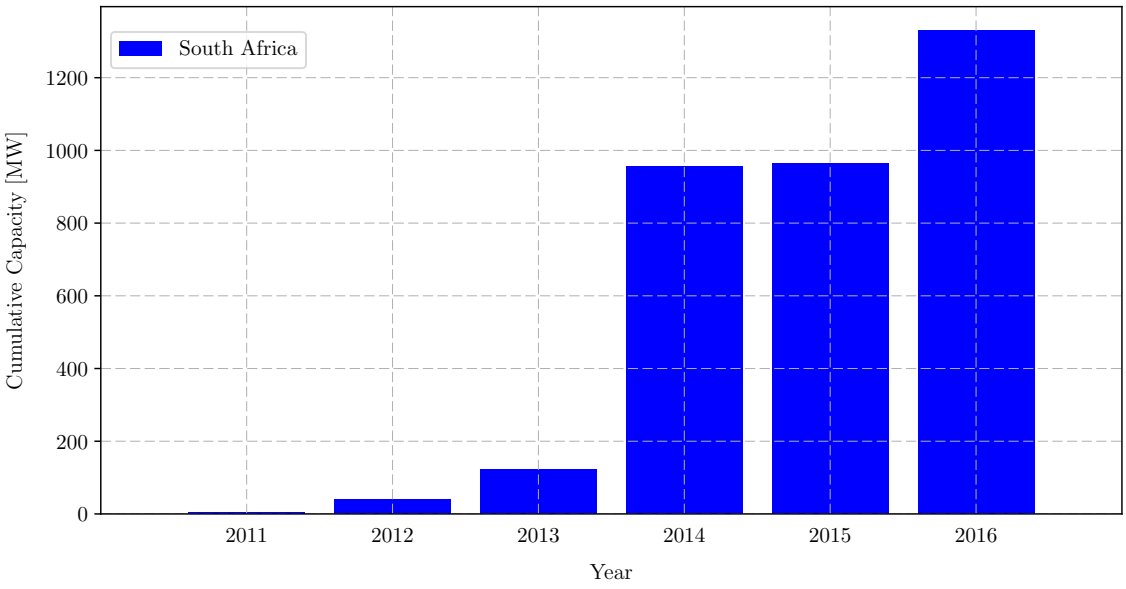

Figure 1.3: Cumulative capacity of South Africa in 2016

The bidding rounds in South Africa is of great concern for independent power producers (IPP). Recent bid round four came in at a price of R 0.786 per kilowatt [44]. Solar PV tariff costs declined in the bidding rounds for South Africa REIPPP in the three years. This is shown in Figure 1.4, with the four bidding rounds.

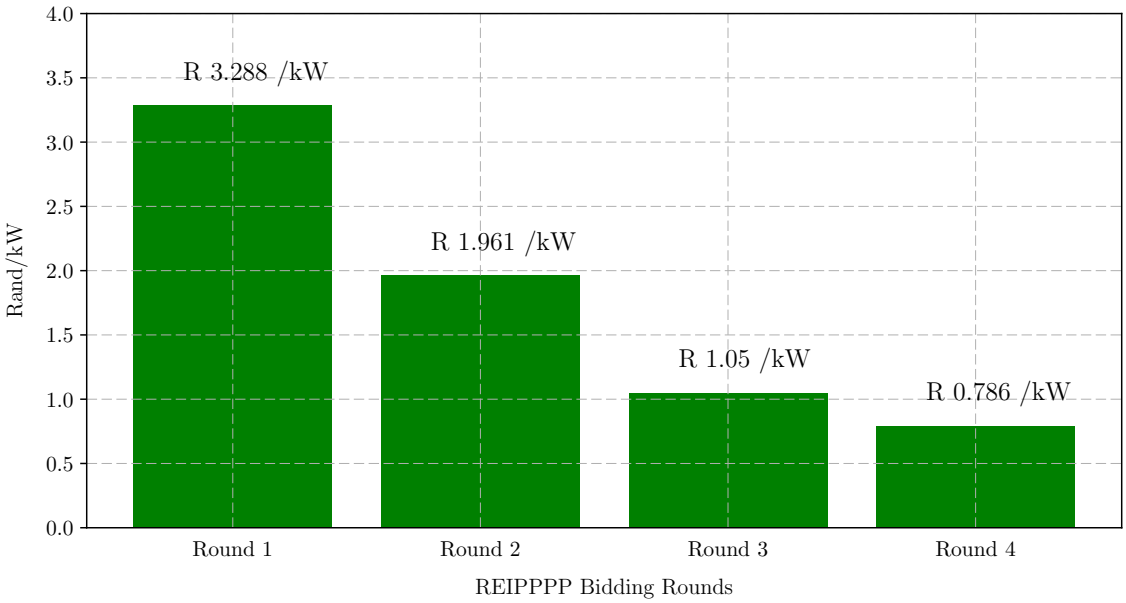

Figure 1.4: REIPPPP bidding round prices per kW in South Africa [44]

1.2 Problem Statement

From Figure 1.4 it is evident that the competitiveness of solar power in South Africa is on the rise. This resulted that the bidding in the following REIPPPP rounds will come in at lower and lower prices per kilowatt and less margins for error capital can be afforded. Thus

to better understand and predict the proposed solar system, accurate prediction of yearly yield is important for the financial model. Accurate prediction requires accurate models which can still be improved significantly. The equivalent model of a solar PV module and the influences different parameters have on the model is investigated. The solar spectrum and the influence on the current and voltage curve is studied. Thus modelling, simulation and field measurements are done to conduct this study.

1.2.1 Objectives and Goals

The objectives and goals of this thesis are divided into two different parts and will be discussed as they are presented in the chapters.

Firstly the investigation into the photovoltaic parameters are discussed with the following objectives and goals:

Goals

- Photovoltaic models with the different equivalent circuits associated with these models must be studied and understood.
- Different parameters and factors that are involved in photovoltaic models will be studied.
- Photovoltaic parameter extraction from current and voltage measurements must be obtained.
- The parameters from the field data will be examined and analysed.
- Comparison between actual field data's parameters and parameter prediction methods must be evaluated.
- A parameter extraction method will be developed to extract parameters accurately without the current and voltage data.
- Investigation of the individual parameters and their comparison to the parameter extraction methods.

Objectives

- Thorough research into photovoltaic equivalent circuits.
- Extract parameters from current and voltage curves.
- Look at the outcome of the extraction methods and the influences.
- Develop an adjustment to correct possible errors.
- Investigate the individual parameters to find the parameters which cause the error made by the extraction method studied.

Secondly the spectral data acquisition and analysis is discussed with the following objectives and goals:

Goals

- Development of a system to evaluate the spectrum with the performance output of a solar module must be developed with possible data analysis of the data measured by the developed system.
- Investigation into a method that measure spectral distribution of a photovoltaic module.
- Development of an automated system that measures the spectrum and the current voltage curve of a photovoltaic module.
- Study the different methods to quantify spectral quality and distribution.
- Analyse the data that are measured to find correlations.

Objectives

- Look into the different ways solar spectrum can be measured.
- List the different quantification methods used in spectral analysis.
- Use available resources to build a system that can measure the desired data automatically.
- Analyse the data by applying the different quantification methods.
- Compare the measured data to reference spectra to draw conclusions.

There are many software packages available on the market to do accurate performance analysis for a specific solar plant. All these packages require very accurate and intensive weather data to do a power prediction. Researchers have shown much interest in the extraction of photovoltaic parameters in the past years [39]. The use of available data are an advantage to develop an accurate parameter extraction method that can extract parameters accurately, without many weather data or current voltage curves. With this research a better understanding about the photovoltaic cell's parameters can be developed and a simpler method can be used to predict the power of a solar farm. A method to predict the power yield with only few data history points is important for quick and accurate power estimation without expensive software packages.

Factors that influence the variation in parameters are the environmental conditions. Manufacturers test photovoltaic modules in lab conditions at STC. These conditions almost never exist in real life solar farms. Thus the understanding of the spectrum and the way it differs throughout the day is important. This spectral data can be compared to the lab conditions to see if there are not better and more accurate testing conditions that photovoltaic manufacturers can use to test the performance of modules.

1.3 Thesis Outline

A short summary of the contents of each chapter is given. Chapter 2 consists of background information. Chapter 3 and 4 outline the research and measurements done. Chapter 5 concludes this thesis with further recommendations.

1.3.1 Chapter 2

This chapter contains the fundamental background information for this thesis. The chapter begins with the sun and the angles involved in solar photovoltaics, which are necessary to do the calculations required at stages throughout the thesis. The solar spectrum, which is the source of the irradiance on Earth, is discussed and key concepts are explained. The influence of the different environmental and photovoltaic parameter factors on the current-voltage curve is shown, to give the reader insight into the importance of the parameters of a photovoltaic cell.

1.3.2 Chapter 3

The main focus of this chapter is the parameters associated with a photovoltaic module. The data used in this study are from a research facility in the Northern Cape. The hardware used to acquire the data is discussed. The parameters of the measured current-voltage curves are extracted and examined. A well known researcher in photovoltaics, De Soto, has developed an extraction method, which extracts the parameters with only the irradiance and cell temperature known. De Soto's method is implemented and the results for each parameter is compared to those of the actual parameters extracted from the current-voltage curve.

Thereafter improvements on the power output of De Soto's extraction method is done with the use of an adjustment function. This adjustment function is optimised to give an average percentage error, for the extraction of the output power, close to zero. The parameters are studied further by looking at each parameter individually and comparing it with the actual parameters measured. The individual parameter extraction equations of De Soto's method are adjusted to correlate better with the actual measured parameter data.

1.3.3 Chapter 4

The main focus of this chapter is to develop an automated spectrum measurement system for the analysis of spectral data, with the combination of performance data from a solar module. The development of the hardware used to achieve this automated measurement system is explained in detail. The software for developing communication and storing data is shown.

Spectral analysis for the facility is done. Firstly, important and known spectral evaluation and quantification methods is examined. This is then used to analyse the spectrum that was measured. The analysis of the colour bands showed interesting factors about the spectrum. The short circuit current and the open circuit voltage is then studied with the spectrum to show correlations between the source, the sun, and the output power of a photovoltaic module. The chapter is finished off with interesting observations made in the recorded data.

1.3.4 Chapter 5

This chapter gives the summary of the results and conclusions made in this thesis. The recommendations for each study and final remarks are made.

Chapter 2

Fundamental Background

In this chapter the background needed for this thesis is discussed. The angles of the sun with the Earth as reference are shown. The solar spectrum with the airmass values of reference spectra is defined. The different equivalent circuit models for PV are explained and analysed. Influences that the different environmental conditions have on the current voltage-curve are shown.

2.1 The Sun

Our solar system is situated in the Milky Way. The sun is one of more than one billion stars. According to scientists, the sun was formed about 4.6 billion years ago by the solar Nebula [13]. The sun consists of 99.8 % of our solar system's mass and it is estimated that the sun's diameter is 109 times the earth's [13]. The distance from the earth to the sun is about 150 million kilometres [47]. Driven by nuclear reactions, to convert hydrogen to helium in a huge thermonuclear fusion reaction, the temperature of the part of the sun that is visible, is about 5500 ^oC [43]. The sun consists of a predominance of hydrogen with a mixture of other gases [43]. The solar energy source is primarily from the sun's radiant energy, which is measured and known as the solar radiation [66]. The radiation, in total, is known as the total solar irradiance (TSI), and when it is measured as a function of the wavelength, it is called the spectral irradiance (SI). The sun is one of the earth's renewable energy sources and thus very important to the photovoltaic study field. The different angles and positions of the sun with the Earth as reference, is discussed in the following sections.

2.1.1 Earth's Orbit

The earth's movement around the sun is in an elliptical orbit, thus the distance to the sun differs throughout the year. The Perihelion is when the earth is the nearest to the sun and it occurs on the 2nd of January with a distance of $\pm$147 million kilometres. The Aphelion is when the earth is the furthest away from the sun and occurs on the 3rd of July with a distance of $\pm$152 million kilometres [41]. The elliptical movement does not vary much from a circular path, thus the distance can be averaged for all practical means to 149.6 million kilometres [43]. However, when accurate calculations have to be done, the correct distance is necessary and very important. The distance from the earth to the sun, d, can be described and calculated by equation 2.1.

$$d = 1.5 \times 10^8 \left[1 + 0.017 sin\left(\frac{360(n-93)}{365} \right) \right], \tag{2.1}$$

where n is the number of the day in a year, where the 1st of January is day 1 and the 31st of December is day 365.

The earth also rotates around its own axis once each day, with the axis tilted by 23.45^o to the plane of orbit around the sun, called the Elliptical plane. The tilted axis is the cause of the seasons each year. In a 24 hour day, the earth actually rotates 360.99^o, which is why a year actually has 365.25 days and thus there is a 366 day year each 4 years called the Leap year. In Figure 2.1, the rotation is illustrated. A line is formed from the centre of the sun to the centre of the earth, where the equator is on the 21st of March and the 21st of September. These days are known as the Equinox, where the whole earth's day-time and night-time are equal to 12 hours. The winter solstice is on the 21st of June in the Southern hemisphere and the summer solstice is on the 21st of December [41]. Note that the 21st is used, although the days vary each year.

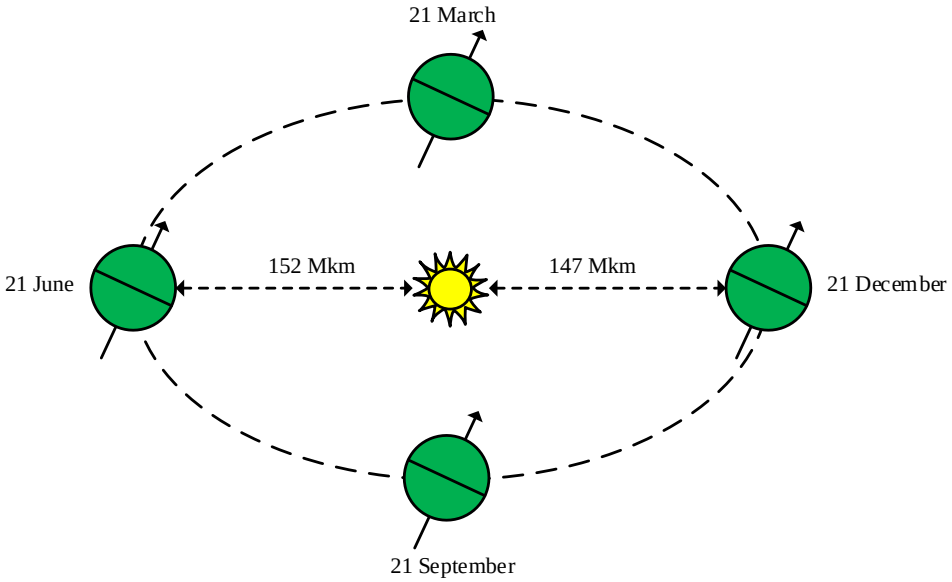

Figure 2.1: The tilt of the earth's rotation axis on the Elliptical plane

2.1.2 Solar Angles

The ability to predict the position of the sun at any location, at any time of the day and any day of the year, is very useful to simulate and calculate the expected yield of a solar plant. To help with the understanding of the position of the earth and its position around the sun, the earth is seen as the fixed observation point spinning around the North-South axis. The sun is shown at different declination angles in Figure 2.2. The variation in the angle of the sun's radiation from the position directly above the equator to $\pm 23.45^o$, is called the declination angle, δ [43]. With the convention of angles to the North as positive and angles to the South as negative, equation 2.2 can be used to calculate the declination angle of the sun at any day of the year.

$$\delta = 23.45sin\left[\frac{360}{365}(n-81)\right], \tag{2.2}$$

where n is the number of days, if 1 January is $n = 1$, the same as it was defined previously.

The literature's theory is based on the Northern hemisphere so it is important to remember that the location of this study is based in South Africa, which is in the Southern hemisphere. Thus the winter and summer is the other way around compared to the Northern hemisphere. The specific latitude, known as the Tropic of Capricorn, is when the sun is located 23.45^o below the equator and the specific latitude, known as the Tropic of Cancer, is when the sun is situated 23.45^o above the equator. This is shown in Figure 2.2. Take note that the measurement of all angles must be in degrees for the use of the equations.

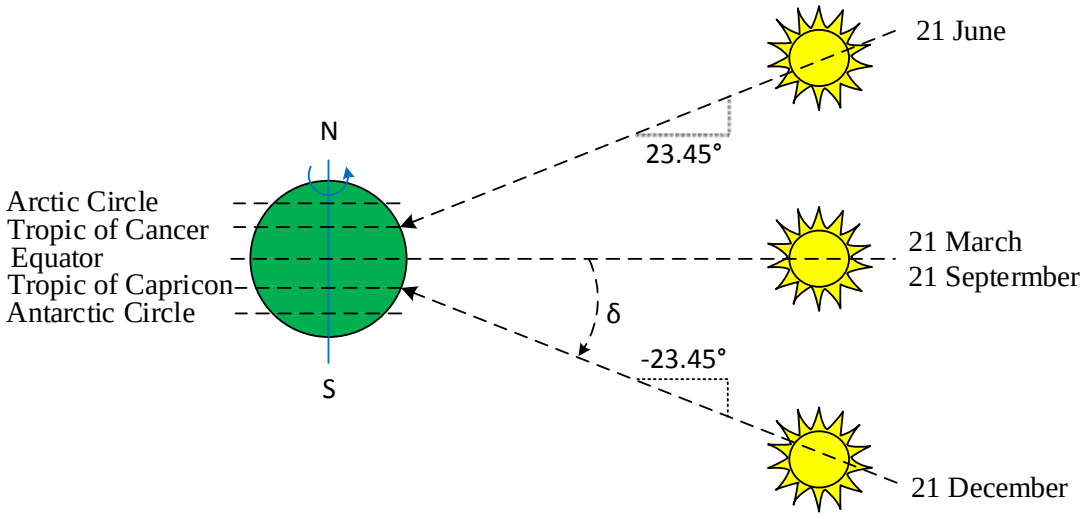

Figure 2.2: Declination angles of the sun throughout the year

The altitude angle is described as the angle between the sun and the local horison beneath the sun, at a specific time. The difference between the declination and altitude angles, is that the declination angle is measured from the equator as reference and the altitude angle is measured anywhere on the earth's surface as reference. The altitude angle is a key solar angle and can help to understand the earth-sun system [41]. This angle can be calculated with equation 3.3 as β for the sun's altitude angle. Figure 2.3 shows the angles in equation 3.3 that are of importance. The zenith is introduced in the equation and it refers to an axis that is drawn directly overhead a location.

$$\beta = 90^o - L + \delta \tag{2.3}$$

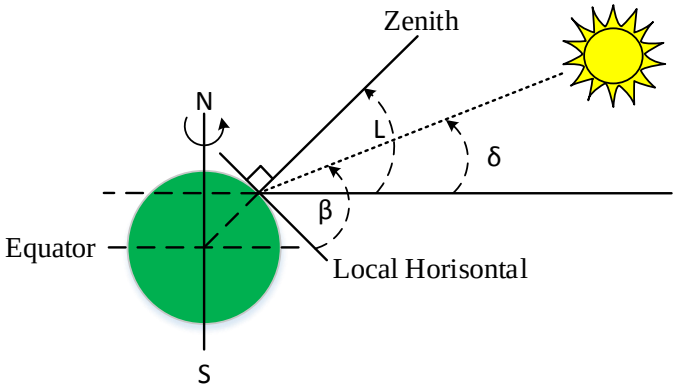

Figure 2.3: Altitude, declination and zenith angle of the sun at solar noon

The difference between the sun's meridian and the earth's meridian, is defined as the hour angle, H [41]. A better description of the hour angle is that it is the number of degrees the earth must rotate for the sun to be directly above a specific longitude. With the assumption that the earth rotates 360^o in a 24 hour day, this is $15^o/hour$, and equation 2.4 can be used to calculate the hour angle.

$$H = \left(\frac{15^o}{hour}\right) \times Hours\ before\ solar\ noon \tag{2.4}$$

2.1.3 Sun's Position

With the altitude and azimuth angle, the location of the sun can be described at any time. The convention used, is that the azimuth angle is positive in the morning when it rises from the East and negative in the afternoon when the sun sets in the West. When calculating the position of the sun, the latitude of the position influences the result. The latitude must be known, as well as the day of year for which the position is to be calculated. The number of hours before or after the solar noon are also needed. From this information you can calculate the azimuth and altitude angles of the sun. The derivation of equation 2.5 and 2.6 can be seen in [41].

$$\sin(\beta) = \cos(L)\cos(\delta)\cos(H) + \sin(L)\sin(\delta) \tag{2.5}$$

$$\sin(\phi_S) = \frac{\cos(\delta)\sin(H)}{\cos(\beta)}\,, \tag{2.6}$$

where ϕ_S is the azimuth angle of the sun, β is the altitude angle, δ is the declination angle, H is the hour angle and L is the latitude.

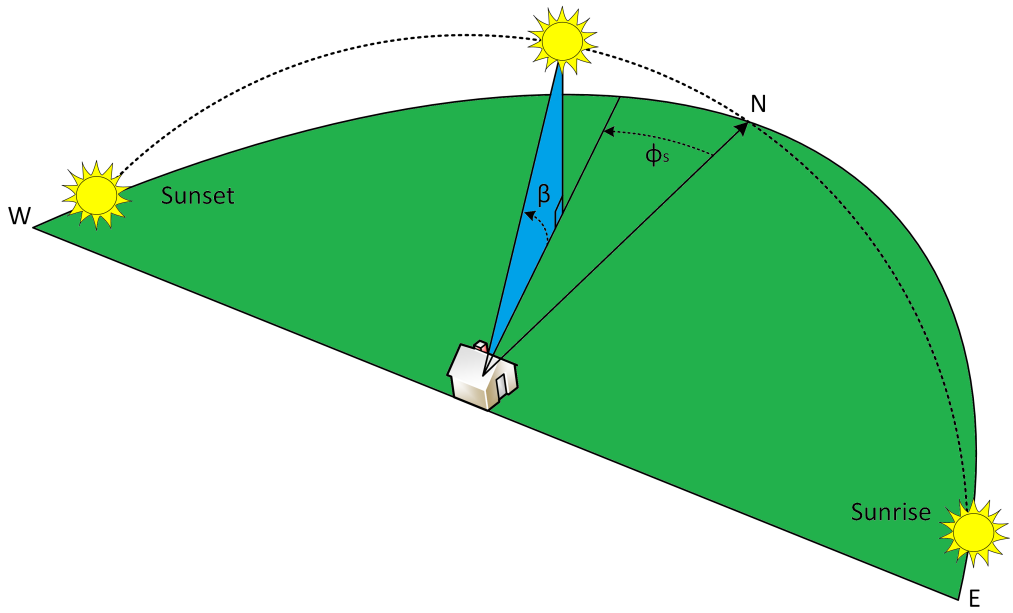

Figure 2.4: The position of the sun illustrated

During spring and summer in the early mornings and late afternoons, when the azimuth angle is more than 90^o away from North, equation 2.6 for sine, does not give the correct answer. A test needs to be used to determine whether the azimuth is greater or less than 90^o from North. The test is defined in equation 2.7.

$$If \quad \cos(H) \geq \frac{\tan(\delta)}{\tan(L)} \quad then \quad \theta_s \leq 90^o \tag{2.7}$$
$$otherwise \quad \theta_s \geq 90^o$$

2.2 Solar Spectrum

The sun's radiation reaches the earth's surface, but it travels a long way to get here. The path brings about losses and is not uninterrupted. In this section, the key concepts about the solar radiance is discussed. Different measurement definitions are discussed and the light, as the spectrum that reaches the earth's surface, is shown.

2.2.1 Irradiance

The radiation received per unit area on the earth's surface can be categorized in different categories, as the atmosphere and other natural elements, like dust and humidity, influence the radiation a unit area receives. The categories are defined as the direct normal irradiance (DNI), the diffuse horisontal irradiance (DHI) and the global horisontal irradiance (GHI).

The DNI is the rays that are received by a surface area that is perpendicular to the sun's rays. It is simply the rays that are coming from a straight line from the sun's position in the sky. These rays are the purest without any, or very little objects in their path.

The DHI is the rays scattered by molecules and particles in the atmosphere and can come from all directions. This excludes the rays that come directly from the sun.

The GHI is the radiation received by a horizontal (parallel) surface to the earth's surface. This value includes both the DHI and DNI [59]. This is typically what a solar module will receive as a source to generate electricity if the solar module is mounted horizontally. POA is the component that the solar module will receive from the GHI, when it is mounted at an angle.

The relationship between DNI, DHI and GHI are shown and illustrated in Figure 2.5.

$$GHI = DNI\cos(\phi) + DHI$$

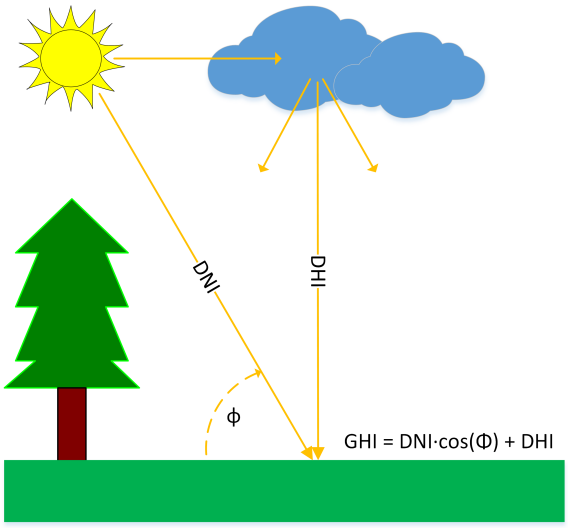

Figure 2.5: Irradiance differentiated rays

2.2.2 Air Mass (AM)

The radiation intensity just above the earth's atmosphere, extraterrestrial, is $\pm 1353 W/m^2$ and the radiation spectrum is referred to as the air mass zero (AM0) spectrum [38]. As the radiation reaches the earth, some of the radiation is absorbed in the atmosphere, thus the reason for the irregular bumpy shape of the terrestrial spectrum [41]. The spectrum reaching the earth's surface depends on the amount of atmosphere the radiation has to pass through. An average the solar spectrum is assumed with a ratio of AM1.5 at the earth's surface and is used to compare radiation data with. The AM1.5 is divided into two different categories, called the AM1.5 global and AM1.5 direct. AM1.5 global consists of all the rays received from direct to diffused, and AM1.5 direct only consists of the direct rays measured. At AM1.5 level of radiation, the incoming solar energy is 2 % ultra-violet, 54% visible and 44% infra-red. The different spectra of the different AM ratio's are shown in Figure 2.6

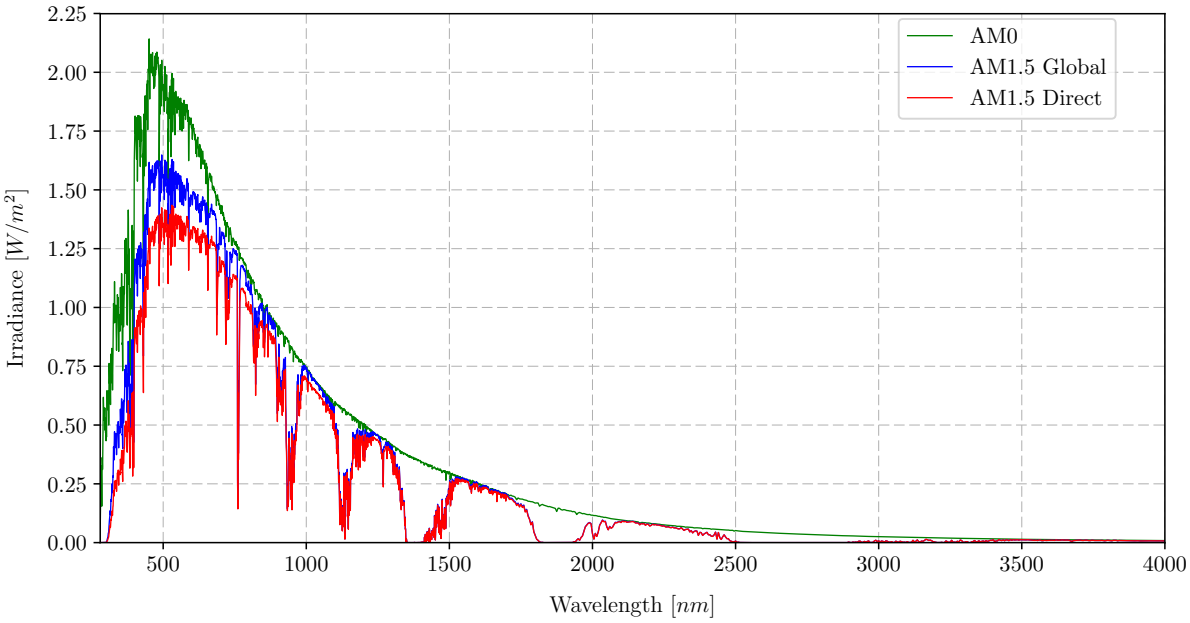

Figure 2.6: AM0, AM1.5 Global and AM1.5 Direct spectrum

The air mass ratio, m, is the length of the path that the sun's rays pass through to reach the earth, divided by the minimum possible path length. An air mass of zero happens when the sun is directly above you. The equation is just valid for altitude angles greater than 10^o. It is visually shown in Figure 2.7. From equation 2.8 it is evident that the longer the path is that the sunlight must pass through the atmosphere, the less energy arrives at the earth's surface. This causes the spectrum received to shift towards the longer wavelengths side of the spectrum [41]. The higher the AM value, the longer the path is for the sun's rays to pass through to reach you. Thus the lower the AM value, the higher the irradiance is that is received. In equation 2.8 the relationship is shown and a graphical illustration is shown in Figure 2.7.

$$m = \frac{L_2}{L_1} = \frac{1}{sin(\beta)}\,, \tag{2.8}$$

where L_1 is the path length through the atmosphere with the sun directly overhead, L_2 is the path length through the atmosphere to reach the point of view and β is the altitude angle of the sun.

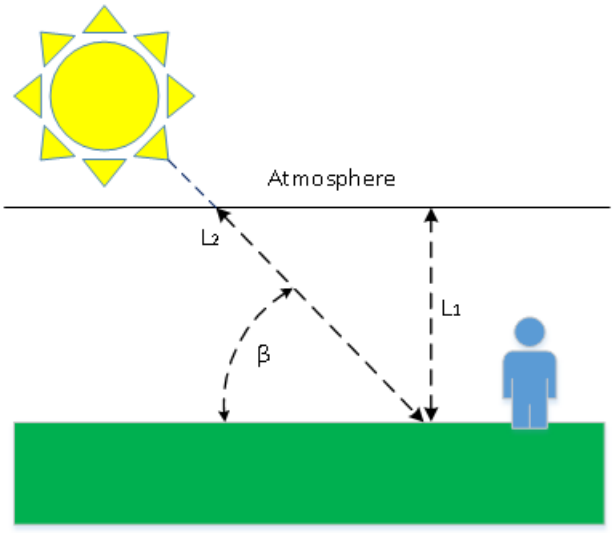

Figure 2.7: Explanation of air mass ratio calculation

The air mass ratio can easily be estimated by equation 2.9.

$$m = \sqrt{1 + (S/H)^2}\,, \tag{2.9}$$

where S is a shadow length caused by an object of a height, H.

In Figure 2.8 a Sankey diagram shows the path of the sun's radiation to the earth with the losses and scattering. It is shown that only 70 % of the radiation from the sun reaches the earth. The biggest contributors to the loss in radiation, are the impurities in the atmosphere. The impurities of the atmosphere differ at different locations and the effect is dependant on environmental conditions.

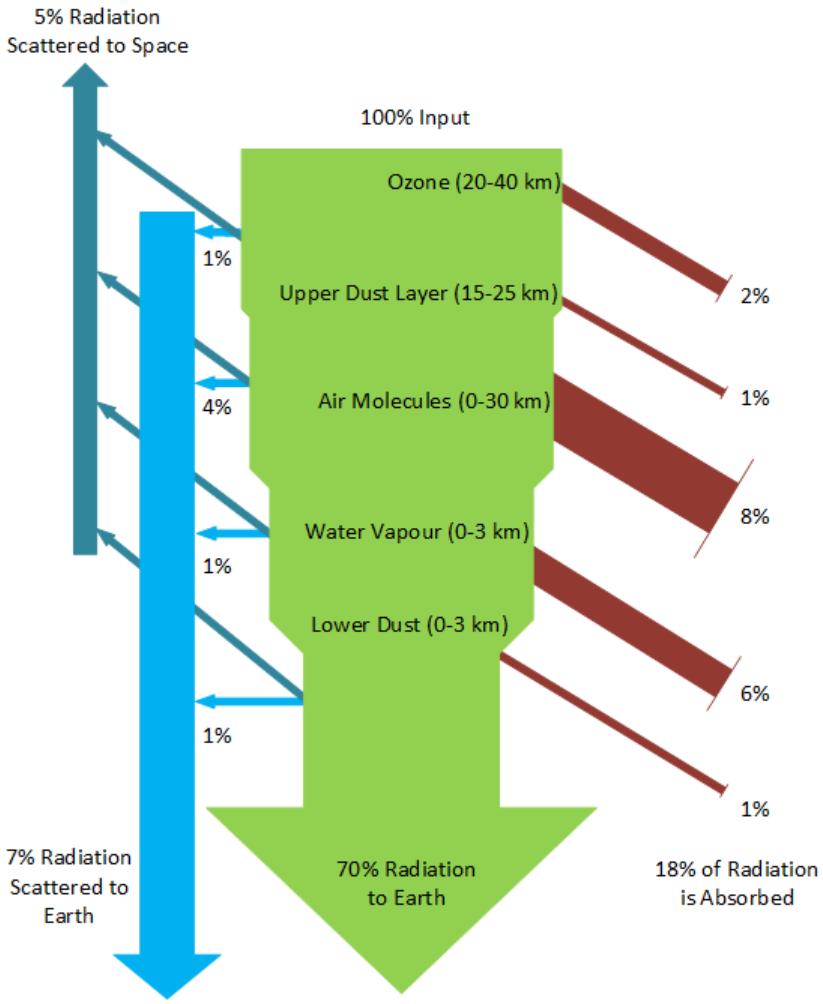

Figure 2.8: Absorption and scattered sunlight radiation for a typical AM1.5 global

2.2.3 Radiation

The electromagnetic radiation, that includes sunlight, consists of particles called photons. The amount of energy that the photons carry are determined by their source's spectral properties. The photon energy, E_λ, can be expressed as in equation 2.10. Equation 2.10 is referred to as the particle-wave duality [16].

$$E_\lambda = \frac{hc}{\lambda}\,, \tag{2.10}$$

where h is Plank's constant ($6.62607004\times10^{34}m^2kg/s$), c is the speed of light ($299792458m/s$) and λ is the wavelength.

The electromagnetic radiation energy an object emits, is a function of the object's temperature to quantify the radiation an object emits, it is compared to a theoretical abstraction. This abstraction is defined as an ideal emitter and absorber, called a black-body [41]. This ideal abstraction in essence does not reflect or transmit radiation, it absorbs all radiation. A black-body's emitted wavelengths depend on its temperature and is described by Planck's law as in equation 2.10.

$$E_\lambda = \frac{3.74 \times 10^8}{\lambda^5 \left[e^{\frac{14400}{\lambda T}} - 1 \right]} , \tag{2.11}$$

where E_λ is the emissive power per unit area, T is the absolute temperature in Kelvin and λ is the wavelength.

The power emitted by a group of wavelengths can be calculated by integration, in order to get the area under Plank's curve. The total radiation power emitted thus is the total area under the curve [41]. The total power emitted can be expressed by the Stefan-Boltzmann law of radiation as shown in equation 2.12.

$$E = \sigma A T^4 , \tag{2.12}$$

where E is the total power emission rate, σ is the Stefan-Boltzmann constant, T is the absolute temperature of the black-body and A is the surface area of the black-body.

Wien's displacement rule can be applied conveniently to the black-body radiation curve to give the wavelength of the maximum spectrum point [41]. Wien's displacement rule is shown in equation 2.13.

$$\lambda_{max}(\mu m) = \frac{2898}{T(K)} \tag{2.13}$$

The surface of the sun has a temperature of 5762 K. The radiation spectrum of the sun can be approximated by the use of a black-body radiator at that temperature [38]. At the earth's surface, the spectral content of sunlight also has scattering and reflection components, which is called the diffused light. The diffused light can account for up to 20% of the incident light that a solar cell receives [38].

The black-body radiation consists of 7 % ultraviolet, 47 % visible and 46 % infra-red light. The solar radiation on the earth's surface does not look the same as the extraterrestrial radiation, because of various constituents in the atmosphere, as was already shown and discussed. The black-body radiation is shown in Figure 2.9 with the AM0 as reference spectra.

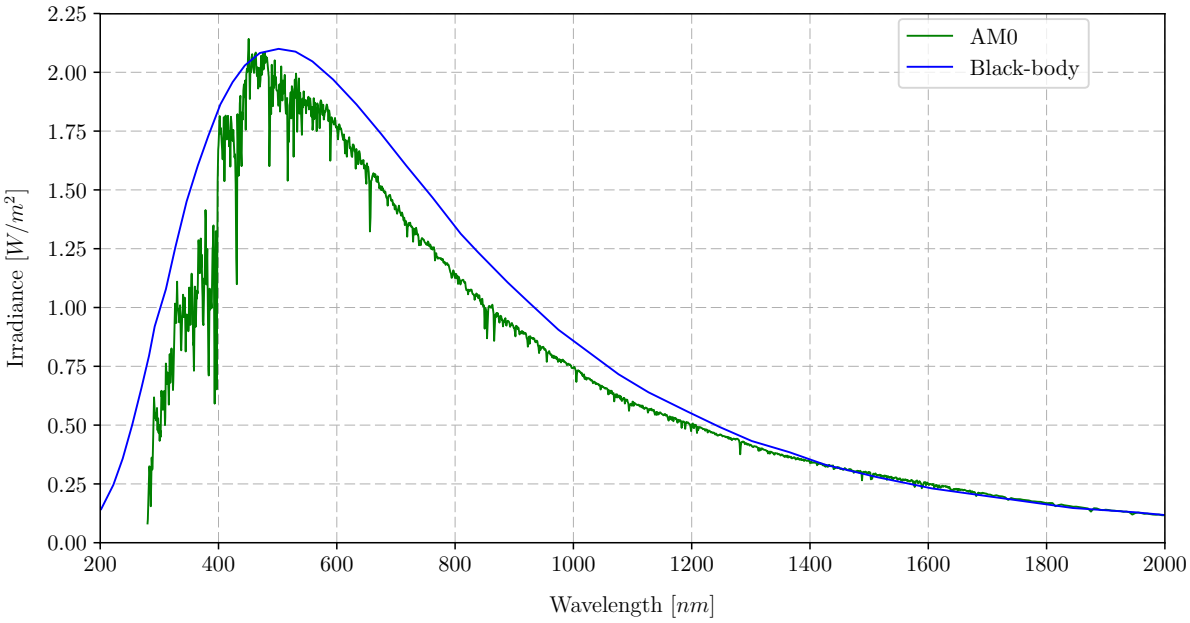

Figure 2.9: AM0 and the black-body radiation

The visible light spectrum can be divided into six main colour divisions according to their wavelength or frequency. Table 2.1 shows the colour represented by the wavelength, as well as the photon energy. The wavelengths below 380 nm are the Ultra-violet band of the spectrum and the wavelengths above 750 nm are the Infra-red band. The different bands are shown in Figure 2.10.

Table 2.1: Visible Spectrum

Colour	Wavelength	Frequency	Photon Energy
Violet	380 - 450 nm	668 - 789 THz	2.75 - 3.26 eV
Blue	450 - 495 nm	606 - 668 THz	2.50 - 2.75 eV
Green	495 - 570 nm	526 - 606 THz	2.17 - 2.50 eV
Yellow	570 - 590 nm	506 - 526 THz	2.10 - 2.17 eV
Orange	590 - 620 nm	484 - 508 THz	2.00 - 2.10 eV
Red	620 - 750 nm	400 - 484 THz	1.65 - 2.00 eV

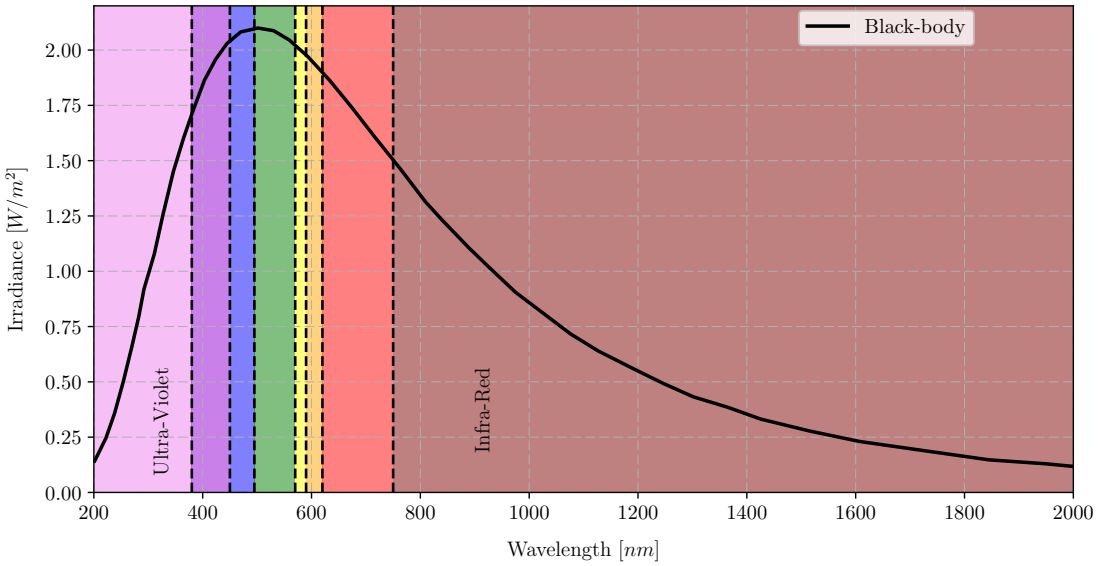

Figure 2.10: Colour bands on the black-body radiation spectrum

2.3 Photovoltaic Effect and Models

In this section, the different models of solar PV cells relevant to this thesis, are given and explained. It is important to understand the fundamental model of a solar cell to evolve to a model that defines the solar cell more accurately. Thus, this section explains the basic working of photovoltaics and thereafter the different models.

2.3.1 Photovoltaic Effect

Electron-hole pairs are produced by photons of sunlight when the energy of the photon is greater than the band-gap energy of the Silicon. The excess photons are dissipated as heat. Different solar cell technologies respond different to the sunlight spectrum.

The number of electrons excited from the valence to the conduction band per photon, is defined as the quantum efficiency (QE). Sunlight in the band-gap range between $1.0 - 1.6\,eV$ can be optimally used. This effect, known as the Shockley-Queisser limit, limits the maximum achievable efficiency of a solar cell to 33%. Silicon has a band-gap of $1.1\,eV$, which is close to the optimum [16].

The spectral response of a solar cell ideally increases with the increase of the wavelength. In reality the long wavelengths are absorbed far away from the collection junction and with the finite diffusion length of the material, the cell's response is limited. At short wavelengths, the energy of the photons cannot be used by the cell [16].

Photons with greater energy than the band-gap energy, E_g, will create an electron-hole pair that contributes to the energy conversion process. It is important to consider the sunlight's spectral nature when designing efficient solar cells [38].

The photovoltaic effect is when certain materials are exposed to a light source and an electric current is produced. This effect was observed back in 1839 by Becquerel [7]. Semiconductor materials are used in solar cells, which is known for the characteristic of insulation at low temperatures and conduction when placed at high temperatures or if it

absorbs energy [16]. Thus semiconductors in solar cells, absorb light and deliver the energy of the absorbed photons to the electrons and holes. A semiconductor pn-junction is used to separate and collect the current carriers. The current carriers are conducted by the semiconductor in a specific direction to form an electrical current [38]. The semiconductor material generally used, is silicon based.

The photovoltaic effect is best described with an illustration of the movement of the holes and electrons in the Silicon based material. The simplest solar cell structure is shown in Figure 2.11. In this figure, the sunlight reaches the top of the solar cell. The metal grid on top of the Silicon and the metal contact at the bottom form the electrical contact of the diode. The metal grid on top allows light to fall onto the semiconductor, which then absorbs the light and converts it into electrical energy [38]. A p-n junction is formed when the n-type and p-type semiconductor are brought together to form the diode. This p-n junction is achieved through diffusion or by the implantation of impurities, known as dopants.

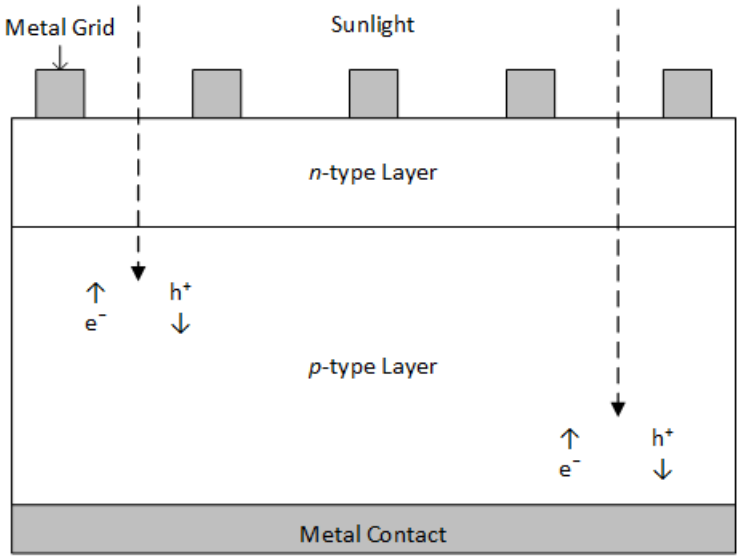

Figure 2.11: Photovoltaic effect in a solar cell.

To simulate a solar cell, an equivalent electric circuit is used to characterise the photovoltaic effect. The different equivalent circuit models are shown and the electric components used to model a solar cell is explained with each model in the following sections.

2.3.2 Basic Single Diode Model

A basic equivalent electric circuit of a solar cell is shown in Figure 2.12. The governing equation for this circuit is equation 2.14. In this equivalent circuit, no resistance is taken into account. The circuit consists of a diode in parallel with an ideal current source [65]. A non-ideal diode is used to introduce the effects of the diode on the basic equivalent circuit. The current source delivers a current in proportion to the irradiation to which the cell is exposed.

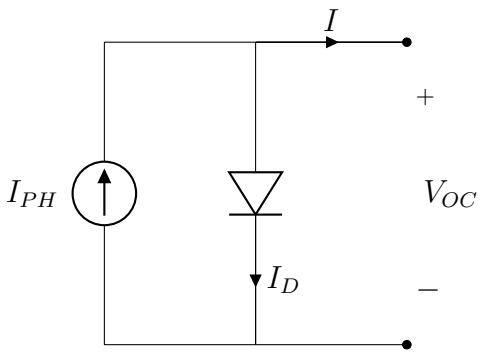

Figure 2.12: Basic solar cell equivalent circuit

Two conditions are of interest for the basic single diode model without a load connected namely, the current that flows when the terminals are shorted together and the voltage across the terminals when it are left open. The short circuit current is equal to I_{SC}. The magnitude of the current through the current source must also be equal to I_{SC}. Kirchhoff's current law is used to give the governing equation for this equivalent circuit [50].

$$I = I_{PH} - I_D \,, \tag{2.14}$$

where I_{PH} is the photo current and I_D is the current flowing through the diode.

The Shockley diode equation is given in equation 2.15. This is the generally known equation for the ideal diode.

$$I_D = I_O\left[e^{\left(\frac{qV_D}{kT}\right)} - 1\right], \tag{2.15}$$

where V_D is the voltage across the diode terminals, k is Boltzmann's constant, q is the elementary charge and T is the cell's temperature and I_O is the reverse saturation current of the diode.

This results in the current equation as shown in equation 2.16.

$$I = I_{SC} - I_O\left[e^{\left(\frac{qV_D}{kT}\right)} - 1\right] \tag{2.16}$$

The other condition, where the terminals are open, the current produced is zero. Thus the open circuit voltage is shown in equation 2.17.

$$V_{OC} = \frac{kT}{q} ln\left(\frac{I_{SC}}{I_O} + 1\right) \tag{2.17}$$

2.3.3 Single Diode Model

The single diode model is a matured version of the basic model. The single diode model offers a good compromise between accuracy, in terms of the circuit representation of a cell, and simplicity, in terms of the characteristic equation, and it is used as the standard

model in PV [65] [14]. The governing equation is given in equation 2.20. The equivalent circuit representation of the single diode model is shown in Figure 2.13.

The light that reaches the cell, is represented as a generated current in the cell called the photo current, I_{PH}. The voltage dependent current that is lost due to recombination occurring in the pn-junction, is represented by the diode and has a current flowing called I_D. The diode's reverse saturation current is referred to as I_O. A resistor, R_{SH}, is part of the circuit to account for the shunt leakage resistance, which causes a leakage current, I_{SH}, to flow. This current will leak to ground. The series resistance, R_S, represents the bonding between the cells, its wire leads and the resistance of the semiconductor itself. The influence these resistances have on the IV-curve is discussed in section 2.4.4. The diode has an ideality factor called a [41]. V_T is the thermal voltage given by equation 2.18.

$$V_T = \frac{kT_c}{q}\,, \tag{2.18}$$

where k is Boltzmann's constant and q is the elementary charge. T_c is the solar cell's temperature [41].

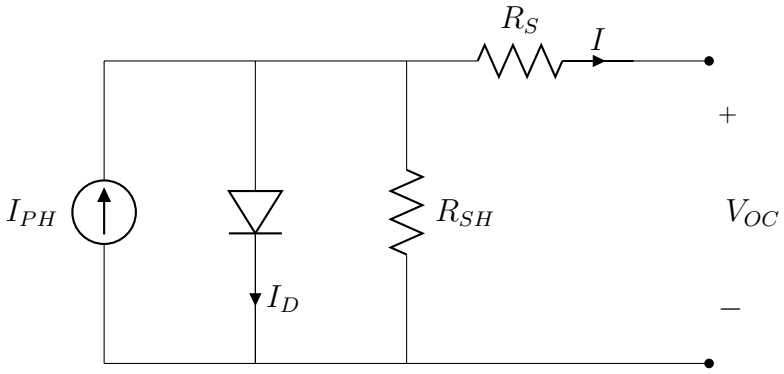

Figure 2.13: Single diode equivalent circuit model

$$I = I_{PH} - I_D - \frac{V + IR_S}{R_{SH}}\,, \tag{2.19}$$

where I_{PH} is the photo current, I_D is the current through the diode, R_S is the series resistance and R_{SH} is the shunt resistance. Equation 2.19 is expanded with the diode current in equation 2.20.

$$I = I_{PH} - I_O\left[e^{\left(\frac{V+IR_S}{aV_T}\right)} - 1\right] - \frac{V + IR_S}{R_{SH}}\,, \tag{2.20}$$

where I_O is the diode's reverse saturation current, a is the diode ideality factor and V_T is the thermal voltage.

The characteristic equation for the circuit is complex and there is no explicit solution for the current or the voltage [41]. The single diode circuit's characteristic equation, equation 2.20, is obtained by using Kirchhoff's current law and the Shockley diode equation, equation 2.15 [35].

2.3.4 Double Diode Model

The double diode model has an additional diode to add the effect of junction recombination in the depletion region [65]. The equivalent circuit representation of the double diode model, is shown in Figure 2.14. Greater accuracy can be achieved by the use of this model, but the computation of the seven unknowns is complex [29].

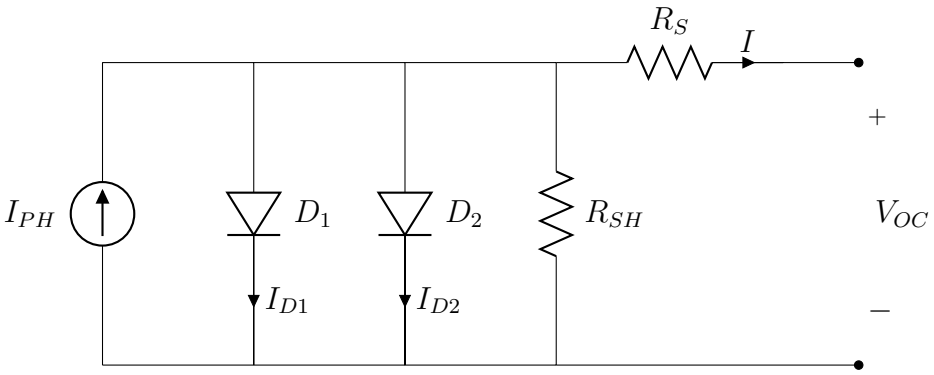

Figure 2.14: Double diode equivalent circuit model

The additional diode adds complexity to the governing equation as can be seen in equation 2.21.

$$I = I_{PH} - I_{D_1} - I_{D_2} - \frac{V + IR_S}{R_{SH}}\,, \tag{2.21}$$

where I_{D_1} is the first diode's current and I_{D_2} is the second diode's current.

When the diode equation is substituted into equation 2.21, the result is equation 2.22.

$$I = I_{PH} - I_{O1}\left[e^{\left(\frac{V+IR_S}{a_1 V_T}\right)} - 1\right] - I_{O2}\left[e^{\left(\frac{V+IR_S}{a_2 V_T}\right)} - 1\right] - \frac{V + IR_S}{R_{SH}}\,, \tag{2.22}$$

where a_1 and a_2 is the ideality factor of the two diodes and I_{O1} and I_{O2} is the diode saturation current of the two different diodes.

2.4 Current-Voltage (IV)-Curve

In the previous section the different models were discussed. This equivalent circuit models are used to represent the IV-curve of the solar cell. The equation for a chosen model describes the behaviour as a continuous function for the different operating conditions the module is subjected to in the solar plant. The function is influenced by a change in temperature or irradiance, which changes the IV-curve.

2.4.1 Maximum Power Point (MPP)

The maximum power point is the point on the IV-curve where the current multiplied by the voltage is the highest. This will give the maximum power that can be produced by the solar module for the conditions it is subjected to. In the ideal case, the MPP is the short circuit current multiplied by the open circuit voltage. This is not true for the

non-ideal case where series and shunt resistance, diode non-ideality and saturation form part of the equivalent circuit. The MPP is used as an comparison parameter for different environmental conditions that influence the IV-curve.

2.4.2 Temperature Impact

Solar cells are very sensitive to temperature, like all semiconductor materials. The increase in temperature will reduce the band-gap of the semiconductor and result in an increase in the electron energy of the material. The temperature of the solar cell is determined by the ambient temperature, the intensity of the sunlight that falls onto the cell, the characteristics of the cell's holder and variables like the wind's velocity [16]. Temperature has an influence on the saturation current, I_O. With the increase in temperature, I_O increases. The relationship is shown in equation 2.23.

$$I_O = BT^3 e^{\left(\frac{-E_{g0}}{kT}\right)}, \tag{2.23}$$

where B is a constant which is independent of the temperature and defined by the diffusivity of the minority carries for silicon and the diffusion length and E_{g0} is the band-gap energy linearly extrapolated to an absolute zero [37].

The increase in temperature results in a small increase in short circuit current, I_{SC}. The number of electron-hole pairs increase, because of the decrease in band-gap energy with the increase of temperature [16]. This effect on silicon cells is small and shown in equation 2.24.

$$\frac{1}{I_{SC}}\frac{dI_{SC}}{dT} \approx +0.06\ \%^oC^{-1} \tag{2.24}$$

The main effect that the increase in temperature has, is on the open circuit voltage. The higher the temperature, the lower the open circuit voltage becomes [41]. The temperature dependency for silicon is shown in equation 2.25.

$$\frac{1}{V_{OC}}\frac{dV_{OC}}{dT} \approx -0.3\ \%^oC^{-1} \tag{2.25}$$

The total effect on the power output is shown in equation 2.26.

$$\frac{1}{P_{MPP}}\frac{dP_{MPP}}{dT} \approx -0.4\ to\ -0.5\ \%^oC^{-1} \tag{2.26}$$

Figure 2.15 shows the impact of increased temperature on the IV-curve as a reduction in the MPP, an increase in temperature and a decrease in voltage.

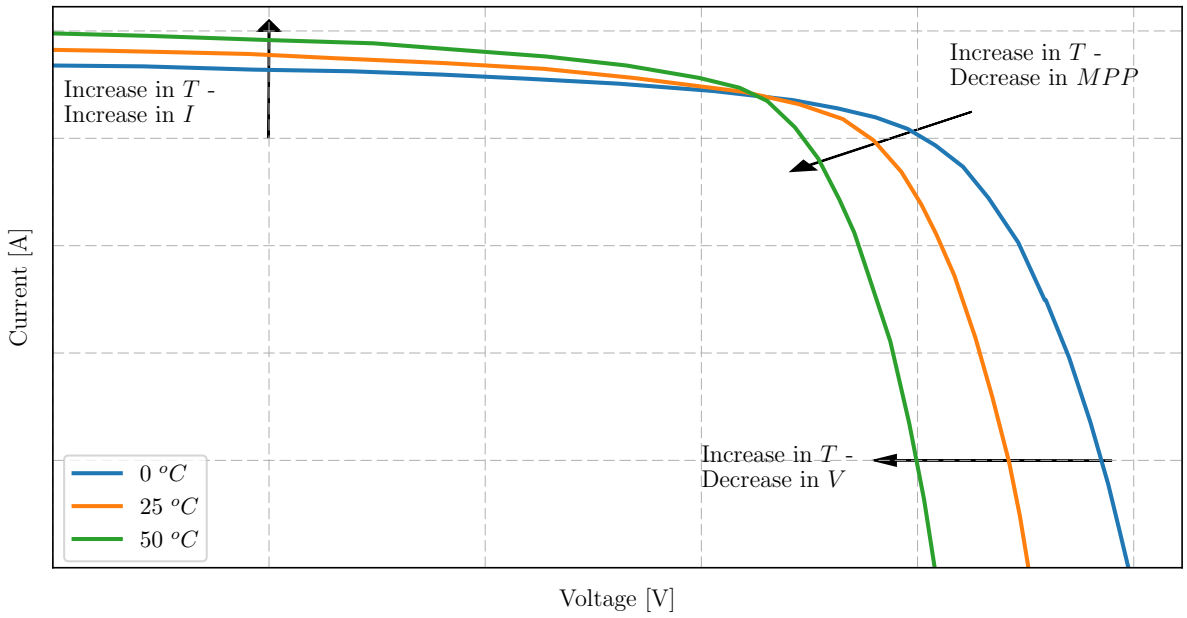

Figure 2.15: The impact on the IV-curve of temperature

2.4.3 Irradiance Impact

The standard spectrum at AM1.5, is referred to as one sun or $1000\,W/m^2$. Irradiance has a direct impact on the short circuit current of a solar cell as shown in equation 2.27. This means that if the irradiance is halved, the short circuit current will also halve. The open circuit voltage drops slightly with a drop in irradiance. Figure 2.16 shows the impact that the increase in irradiance has on the IV-curve. The effect on the maximum power of a cell, is almost linear with the approximation shown in equation 2.28 [37].

$$I_{SC} \propto G \tag{2.27}$$

$$P_{MPP} = G_{POA}\frac{P_{STC}}{1000\,W/m^2} \tag{2.28}$$

The light intensity varies throughout the day, with an irradiance power that varies from 0 to above 1 kW/m^2. With this variation in the light, the shunt resistance becomes important, as it influences the performance the most at low light. The equivalent resistance of the solar cell, tends to approach the shunt resistance as the bias point and the current in the solar cell decreases. When this occurs the fraction of power lost, due to the shunt resistance, is increasing. Under cloudy conditions, early in the morning or late in the afternoon, a solar cell with a high shunt resistance provides a greater fraction of the power normally produced, than a solar cell with a small shunt resistance does [10].

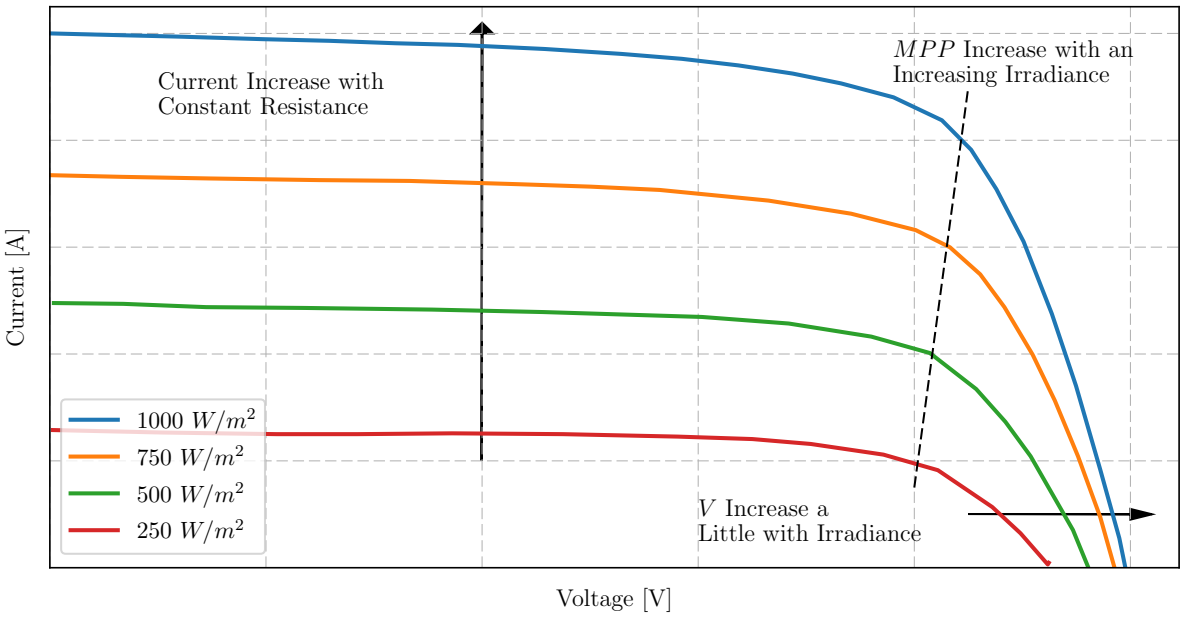

Figure 2.16: The impact of irradiance on the IV-curve

2.4.4 Parasitic Resistances

Parasitic resistances are split into two, known as the series resistance and the shunt resistance. Both these resistances reduce the fill factor of the solar cell [16]. This is important to know, because these resistances influence the MPP on the IV-curve and decrease the fill factor.

2.4.4.1 Series Resistance

The series resistance consists mainly of the bulk resistance of the semiconductor material, metallic connections, carrier transport through the top diffused layer and contact resistances between the metallic contacts and the semiconductor material used in the solar cell [16]. The effect of series resistance is shown in Figure 2.17. The series resistance does not change the open circuit voltages, because with an open circuit, no current flows through the series resistor. For moderate values of series resistance, the influence on the maximum power can be determined by using the power without a series resistor, minus the influence on the power by the series resistor. This approximation is shown in equation 2.29.

$$P_{R_S} = P_{MPP}\left(1 - \frac{I_{SC}}{V_{OC}} R_S\right), \tag{2.29}$$

where P_{R_S} refers to the power output if the series resistor is taken into account.

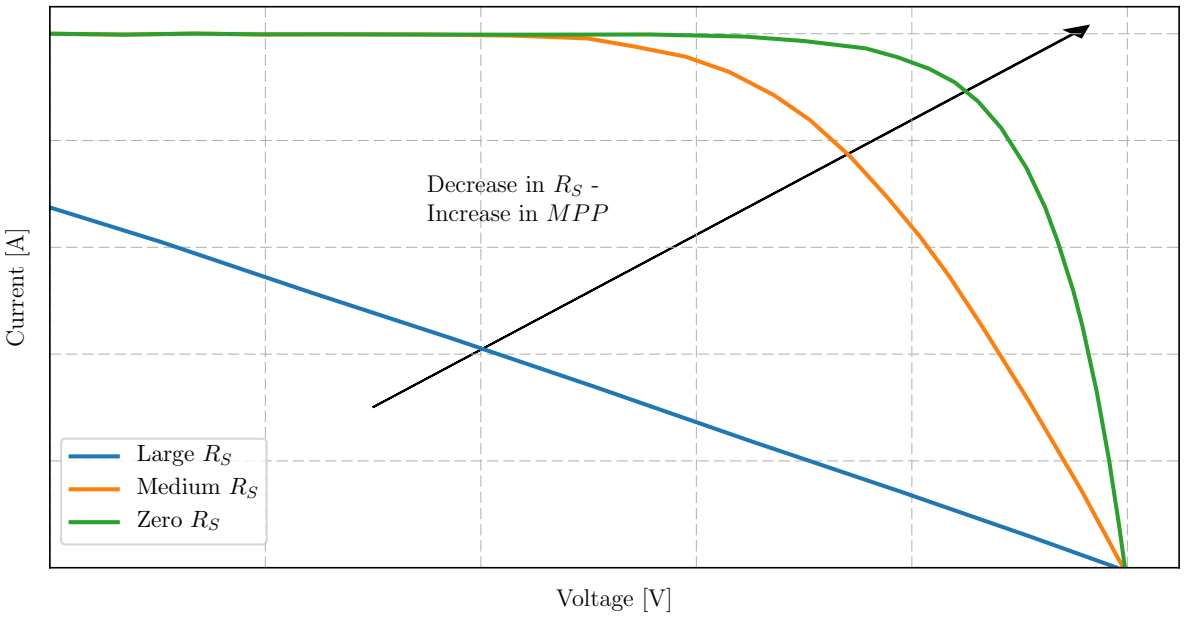

Figure 2.17: The impact on the IV-curve due to series resistance

2.4.4.2 Shunt Resistance

The shunt resistance exists because of the pn junction's non-ideality and impurities at the junction. The impurities cause partial short circuits at the cell edges at the junction [16]. The power loss through the shunt resistor is typically caused by manufacturing defects. If the shunt resistance is too low, it provides another path for the current to flow through and causes the voltage to drop. The effect on the IV-curve is high when there is low light [37]. The effect that the shunt resistance has on the maximum power, can be estimated in the same manner as in the series resistance. The equation is shown in equation 2.30. The effect of shunt resistance on the IV-curve is shown in Figure 2.18.

$$P_{R_{SH}} = P_{MPP}\left(1 - \frac{V_{OC}}{I_{SC}}\frac{1}{R_{SH}}\right), \tag{2.30}$$

where $P_{R_{SH}}$ refers to the power output if the shunt resistor is taken into account.

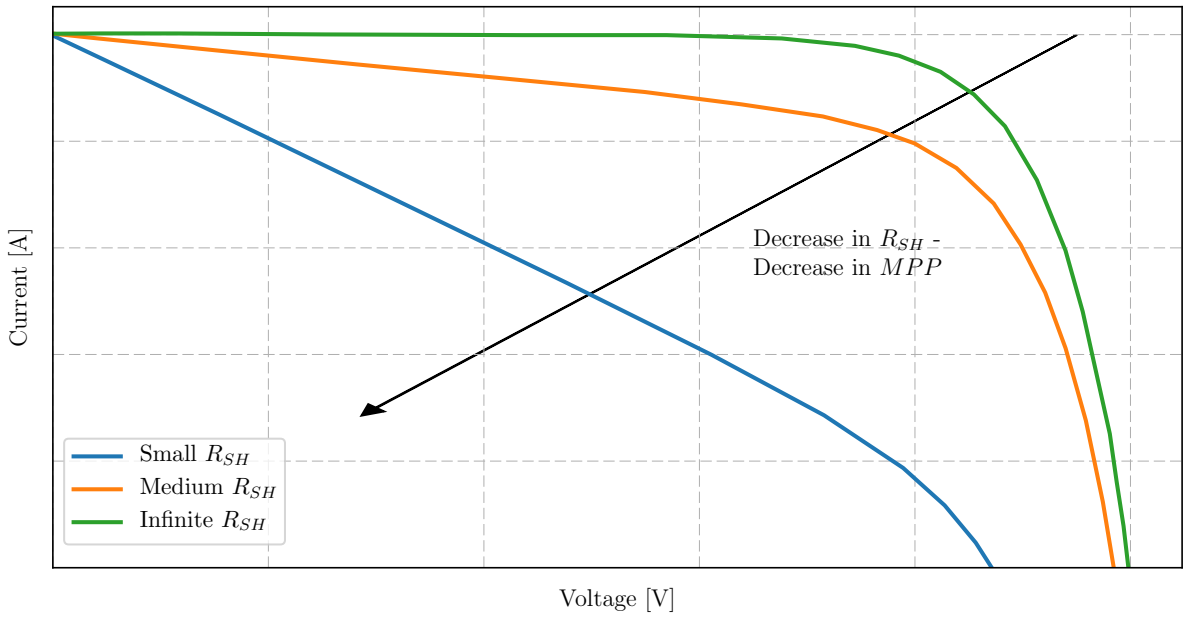

Figure 2.18: The impact on the IV-curve due to shunt resistance

2.4.5 Fill Factor

The fill factor abbreviated by FF, is a measure to determine the maximum power and losses of a solar cell. The FF is defined as shown in equation 2.31, and equals the MPP power, divided by the short circuit current times the open circuit voltage. In Figure 2.19, the FF is shown graphically, and the squareness of the IV-curve can be seen.

$$FF = \frac{P_{MPP}}{I_{SC}V_{OC}} \tag{2.31}$$

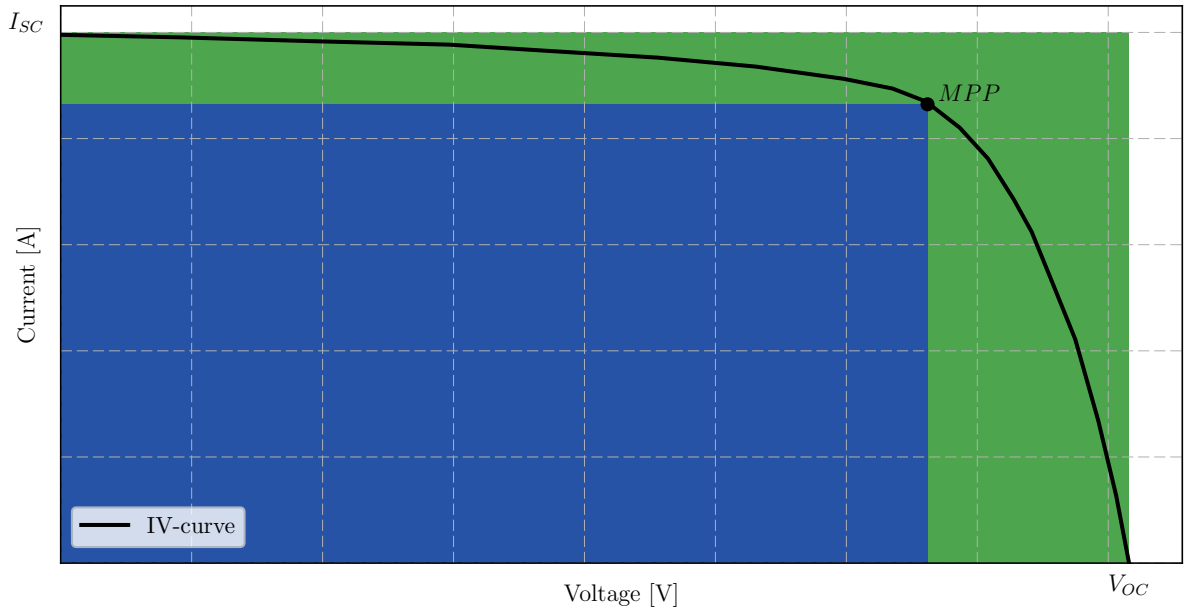

Figure 2.19: Fill factor graphical explanation

2.4.6 Summary

This chapter looked at the different solar angles that are important when studying PV. The AM ratio and the spectrum are shown together with its relevance to PV. All the influences that environmental conditions have on the IV-curve and MPP are discussed. The study is based on the single diode model, but for a more comprehensive approach, the other existing models are explained. The models are idealised circuits with resistors, diodes and a current source. These discrete components do not actually exist in the solar cell itself, but is a representation of the behaviour of the solar cell. These models are only for cells and can easily be adjusted for solar modules with cells in series and parallel.

Chapter 3

Solar PV Parameter Extraction and Parameter Evaluation

3.1 Introduction

It is important to have a performance prediction method in order to give an accurate prediction of a proposed solar photovoltaic (PV) plant's yield. The yield values are predicted in regards to both irradiance and the temperature of the solar cell [55]. With the market already competitive, and increasing exponentially internationally, installing PV power capacity systems [56], and allowing for lowering of costs is becoming crucial. Greater accuracy leads to a lower cost, due to a smaller error margin which could be added into the tender price. Predicting a solar plant's performance based on irradiance and temperature with more accuracy also has importance when sizing a solar plant [56].

Typically, the manufacturers provide the characteristic parameters of the solar panel at specific operating conditions. Generally standardised test conditions (STC) are used, these conditions are defined as 1000 W/m^2, 25 ^oC and 1.5 AM [57]. Presently, there are reliable prediction software available, like Sandia National Laboratory's SAM and PVsyst, but this software requires typical meteorological year (TMY) weather data. However, this weather data is not generally available for solar PV plant sites [57]. The prediction software utilizes the single diode model to forecast performance [55].

De Soto developed a five parameter extraction method using only data sheet values. This method is of great use if only limited data is available. The only variables needed to obtain the IV-curve are: the temperature of the cell and the irradiance. Using the IV-curve the maximum power the module can produce can be found. This method can also be used to predict a modules performance at different levels of irradiance and temperature conditions.

The extracted IV-curves of De Soto's method could be seen as acceptable at STC. However, at different conditions the resulting IV-curves do not match the measured IV-curves. In this study we look into the difference between De Soto's parameter extraction method [57], and the actual parameters measured at a test facility in the Northern Cape. The difference is evaluated by implementing the single diode model, and comparing it to the maximum power point (MPP) resulting from the different parameters. The aim is to present an adjustment to De Soto's parameter extraction, (as) to improve the accuracy of the extracted yield, thus the MPP. The goal is to limit the inputs needed to only irradiance and the solar cell's temperature, thus not changing the complexity of De Soto's

method.

3.2 Location

The research facility is a standalone system (off-grid) that is located within the perimeter of the Kalkbult solar plant near De Aar in the Northern Cape. (30.161 Latitude and 24.132 Longitude). In this study only one of the research facility's modules data were used. Because of the other studies conducted on the facility, a reference module from the facility was also used. This module is cleaned regularly, without any coating sprayed onto it. This section will only include information about the facility which is directly relevant to this study, further information about the facility can be seen in A. du Plessis's thesis [51]. Obtaining the data and the hardware used and installed on the facility is discussed. This includes hardware used to acquire the data that are used and analysed.

3.2.1 Facility

The research facility consists of 32 solar modules. Some modules are used just to charge on site batteries, but 24 of the modules have their own monitoring system. The research facility was constructed in 2016 with the objective to enable students to conduct studies in the specific environment. The standalone system enables full control over the research plant and research, without the risk of interfering with a commercial PV plant. In Figure 3.1 the location of the facility is shown, with the Kalkbult solar plant to the left and the grid connecting substation to the right.

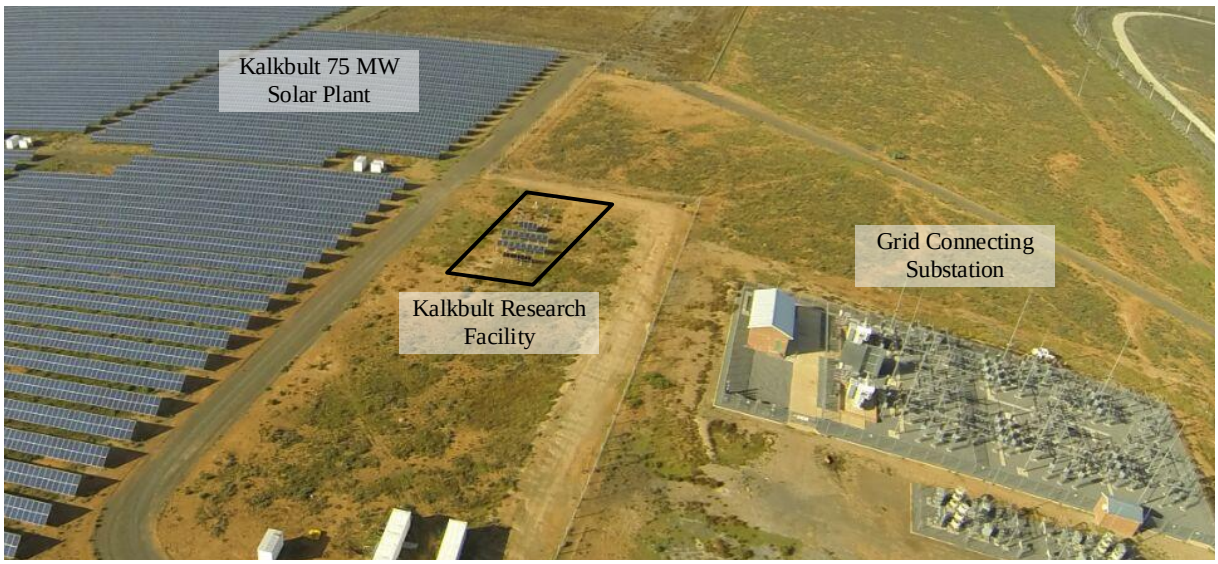

Figure 3.1: Air photo showing the research facility. Photo: Kurt Krog

3.2.2 Climate and Weather

The climate at the facility is typically semi-arid. The days are mostly sunny and the nights are cool [62]. The summers are very hot and the winters very cold, thus extreme temperatures are experienced at this location. The precipitation is mostly in the summer months with an average yearly rainfall of 336 mm.

Historical weather at the location from MyWeather2 [26], is tabulated in Table 3.1. From the table, it is evident that the maximum temperature occurs in January and February at 40 ^oC, and the minimum at -8 ^oC in July. The average wind speed varies between 14 and 20 km/h throughout the year.

Table 3.1: Historical Weather at the research facility

Month	T_H	T_L	T_{max}	T_{min}	H	R	S	W_{avg}	W_{max}
January	33	16	40	6	44	50	12	18	65
February	33	17	40	6	46	39	11	17	69
March	29	14	37	4	51	49	11	16	56
April	25	10	34	1	53	32	10	14	61
May	21	7	29	-3	55	16	9	14	61
June	18	3	24	-4	52	9	9	14	61
July	18	3	26	-8	49	16	9	15	67
August	20	4	29	-6	42	8	10	16	65
September	25	7	34	-3	36	17	10	17	81
October	28	11	36	0	37	20	11	19	67
November	30	13	37	2	38	36	12	20	70
December	32	15	38	4	39	37	13	19	98
	^oC	^oC	^oC	^oC	%	mm	Hours	km/h	km/h

T_H	Highest Avg Temperature	T_L	Lowest Avg Temperature
T_{max}	Maximum Temperature	T_{min}	Minimum Temperature
H	Humidity	R	Rain
S	Sun shine	W_{avg}	Average wind speed
W_{max}	Maximum wind speed		

3.3 Hardware

The hardware that is used to measure the data used in this study, is primarily a solar module, an active load and a weather station. These components are discussed and the full system is described and shown in the following sections. The understanding of the hardware is fundamental, because the data used are obtained from it. Thus tolerances on the hardware must be taken into consideration when the data are used and conclusions are made.

3.3.1 Solar Module

The facility has thin-film and poly-crystalline silicon (pc-Si) modules installed. For this study a pc-Si module will be examined. The pc-Si module is a Renesola Virtus II JC255M-24/Bb module [22]. The electrical and influential characteristic coefficients of the module are shown in Table 3.2 and the mechanical characteristics are shown in Table 3.3. These characteristics are at STC (1000 W/m^2, 25 ^oC, 1.5 AM).

The optimal tilt of a solar module is at solar noon and it is calculated with the use of the altitude angle of the sun. The mounting of the modules are fixed, thus an average tilt needs to be calculated. To do this, the declination angle, δ, is calculated for the 21st of June, $n = 172$, and the 21st of December, $n = 355$. Equation 2.2 is used.

$$\delta = 23.45^o sin\left[\frac{360}{365}(172 - 81)\right] = 23.15^o \tag{3.1}$$

$$\delta = 23.45^o sin\left[\frac{360}{365}(355 - 81)\right] = -23.45^o \tag{3.2}$$

The declination angle of 0^o is used in equation 3.3, because the two extremes in the winter and summer cancel each other to give an average of zero.

$$\beta = 90^o - L + \delta = 59.84^o \tag{3.3}$$

The optimal tilt angle is calculated by equation 3.4. Thus the solar modules are mounted at 30^o.

$$Optimal\ \ Tilt = 90^o - \beta = 90^o - 59.84^o = 30.16^o \tag{3.4}$$

Table 3.2: Electrical and influential characteristics of the Renesola VirtusII.

Characteristic	Description	Value	Unit
P_{MPP}	Power at the MPP	255 ($\pm$5)	W
V_{OC}	Open Circuit Voltage	37.5	V
I_{SC}	Short Circuit Current	8.86	A
V_{MPP}	Voltage at MPP	30.4	V
I_{MPP}	Current at MPP	8.39	A
$T_{V_{OC}}$	Temperature influence on V_{OC}	-0.3	$\%/^oC$
$T_{I_{SC}}$	Temperature influence on I_{SC}	+0.04	$\%/^oC$
$T_{P_{max}}$	Temperature influence on P_{max}	-0.4	$\%/^oC$

The mechanical characteristics are shown in Table 3.3.

Table 3.3: Mechanical characteristics of the Renesola VirtusII.

Characteristic	Description
Cell Type	Polycrystalline 156 x 156 mm, 60 pcs in Series
Glass	Hi-Transmission, Low Iron, Tempered Glass
Frame	Anodised Aluminum Alloy
Junction Box	IP65/IP67 Rated, With Bypass Dodes
Dimension	1640 x 992 x 40 mm
Output Cable	4 mm^2
Weight	12 Kg

3.3.2 Active Load

The active load is a device that measures the IV-curve of a PV module. The device was developed by Andreas Ndapuka, a previous masters degree student at the University of Stellenbosch [46]. The device has additional functionality, which includes the maximum power point (MPP) function, storage to an on-board SD card and back of the cell temperature measurement capabilities. The MPP function allows for the PV module to be used during the period it is being used for tests, by only extracting the IV-curve on a timed period and generating the power to charge a battery in-between. The active load is fundamentally a DC to DC switch-mode converter, which is able to control the power delivered to the fixed load resistor by altering the duty cycle and extracting the IV-curve. The device is able to extract the IV-curve within two seconds. The device's design and specifications can be seen in Andreas Ndapuka's thesis, [46].

The active load was tested and it was established that the maximum measurement uncertainty was 0.5 %, as shown by Andreas [46]. The device's specifications are shown in Table 3.4.

Table 3.4: Active load specifications

Input Voltage	100/50	V
Input Current	50A/100V	10A/50V
Switching Frequency	40	kHz

The device is able to read the back-of-cell temperatures by the use of a high accuracy ADT7310 digital temperature sensor circuit, which was developed by Douw du Plessis, also a previous masters student [20]. The sensor is fitted to the back of the PV module, which is required by the IEC61724 standard. The sensor digitises the temperature reading to a resolution of 0.0625^oC. The sensor communicates via a serial peripheral interface (SPI) to the active load device to measure the temperature for each IV-curve extraction. A photo of an installed active load is shown in Figure 3.2

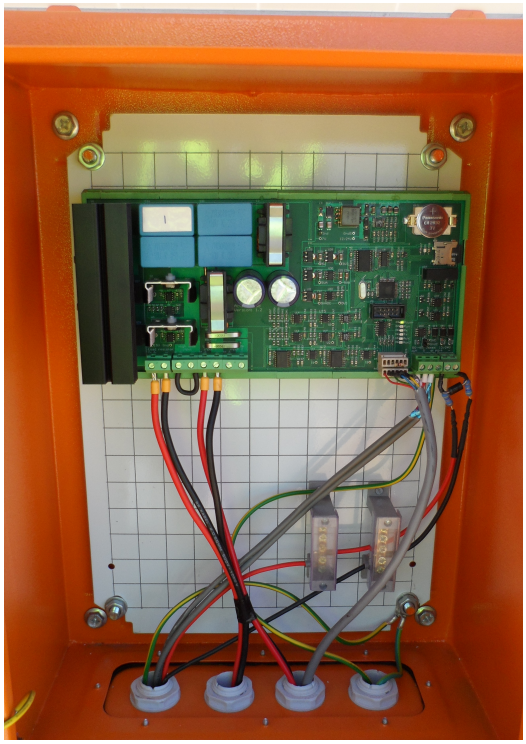

Figure 3.2: Active load installed in an electric box at the research facility

3.3.3 Weather Data

The facility has a full weather station. The weather data were acquired by a product from Met One Instruments Inc. The Met one-485 (MSO-485) weather station [9] is a meteorological data station which complies with the IEC61724 standard. POA irradiance is measured with a Kipp and Zonen SMP10 pyranometer. The rainfall is measured with a Met One Instruments 372-series precipitation gauge [9]. The measurement device works with tipping buckets, which is calibrated to tip for each 0.5 mm of rain. These three devices give the following data:

- Wind Speed
- Wind Direction
- Barometric Pressure
- Ambient Temperature
- Humidity
- Rainfall
- Irradiance

The output data of the weather station were communicated to the Raspberry Pi through a RS-485 serial communication connection. The weather station is located in one corner of the facility's area. It is orientated to true North at a height of 3 meter. The measurement of the wind speed is done with a three cup anemometer and the direction of the wind, with a lightweight vane tail. Figure 3.3 shows a photo of the weather data devices installed at the facility.

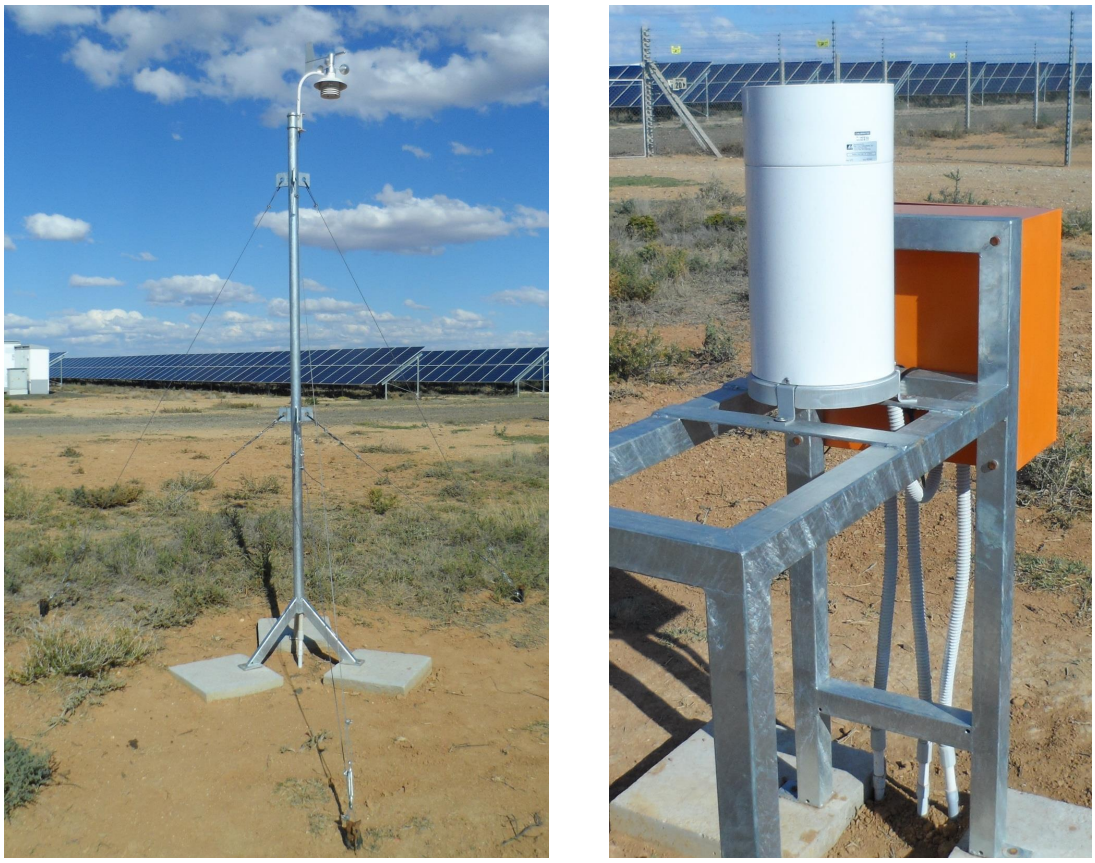

Figure 3.3: Met One-485 weather station and Met One-372-series precipitation gauge

Only the irradiance data of the weather station was used.

There are mainly two different principal type of devices which are used to measure the solar radiation on the earth. The first is called a pyranometer, which is also used at the research facility. It is the most widely used instrument and measures the total radiation, including the direct and diffused radiation. The second device is called a pyrheliometer. This device measures only the direct beam radiation by looking into the sun through a narrow tube. Pyrheliometers' data are more for use in concentrating solar power applications [41].

A pyranometer and pyrheliometer consist of a stack of thermocouples, also known as thermopile, to measure the temperature of a black surface when it is exposed to light. The thermopile is referred to as the detector that responds to the incoming radiation. A difference in voltage is measured between a black and white surface, which is proportional to the isolation. Black surfaces absorb the sunlight, while white surfaces reflect the sunlight. Another method used is to measure only the temperature difference between the ambient temperature and a black surface. There are other devices that use a photo-diode to measure the radiation, but the accuracy is less than the devices based on thermopile, and thus is less expensive [41]. The photoelectric based sensors can only respond to a limited range of wavelengths of the solar spectrum which add to inaccuracy of measurements. These sensors are well calibrated for clear sky conditions, but fail to give any reliable measurement if the sun passes through glass or clouds.

The pyranometer used at the research facility is a Kipp and Zonen SMP10 [9]. It is situated to measure the plane of array irradiance (POA) which is a 30^o tilt angle on the

fixed PV modules. The pyranometer communicates through a RS-485 MODBUS serial output to the active load. The mounting of the pyranometer is shown in Figure 3.4.

Figure 3.4: Kipp and Zonen SMP10 pyranometer fixed on the POA

3.3.4 Communication

The purpose of communication within the facility, is to allow remote-system monitoring, to upload data to an online database and to establish a local inter-device communication network. Communication between devices is done through RS-485 by using the MODBUS protocol with a 9600 bits per second baudrate. A Raspberry Pi is configured to be the master device and the other devices the slaves. The Raspberry Pi is responsible for the handling of the communication from external queries to internal data handling. The hardware is configured to store the data collected on-site and on a cloud database. A local internet service provider (ISP) provides the internet which is then distributed throughout the facility with a router. The master device, Raspberry Pi, acquires the data measured from the slave devices and uploads the data to the database online, where the data are stored and available for interpretation and research.

3.3.5 System Integration

The system is connected together as shown in Figure 3.5. The solar module is also connected to the active load. All the data are recorded with the Raspberry Pi and uploaded to the database. Further information about the software follows in the next section.

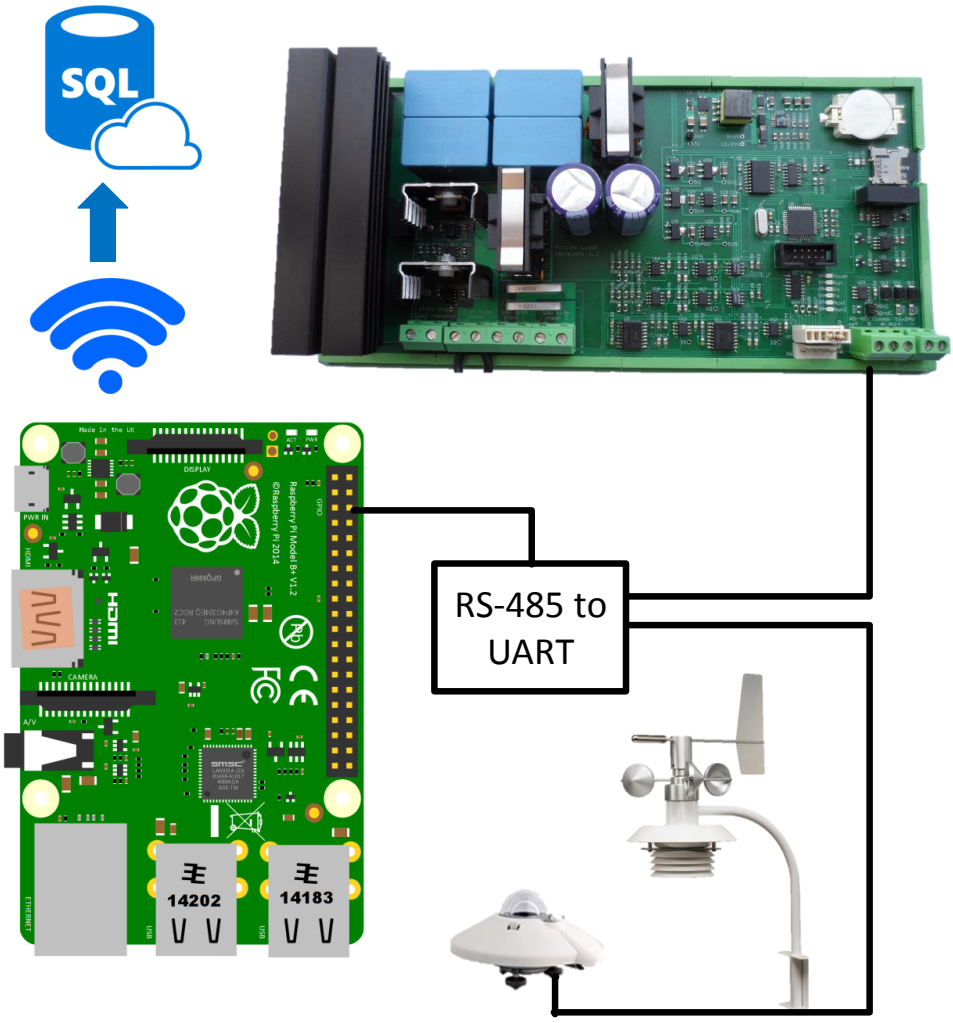

Figure 3.5: The research facility's system integration

3.4 Software

The software languages used to analyse the data, are Python and SQL. Python is used to interact with the database by sending SQL commands. All the data are hosted on a MySQL database on www.pvsoiling.co.za. The data that are needed for this study, is part of different tables within the database, thus data analysis requires a new combined table to process the data faster. An overview of the languages is given and then examples of important functions used are shown.

3.4.1 SQL Language

SQL (Structured Query Language) is the standard language used to communicate with a database. The language is used to store, manipulate and retrieve data of a database. The ANSI (American National Standards Institute) says it is the standard language for relational database management systems [61]. Although some databases have their own proprietary extensions, the standard SQL commands can do almost everything you want to do with a database. Standard SQL commands include: Select, Update, Insert, Create,

Delete and Drop. This language was used in combination with Python to achieve the calculations with the data in the database.

3.4.2 Python Language

Python is an object-orientated, high-level programming language. It is used in this study as it is very attractive for scripting or as a glue language to connect to existing components with its high-level built in data structures. Python is an open source platform which supports modules and packages, including the extensive standard library [61]. This makes it easy to use and learn. Python is used in this study as a platform to communicate with the SQL database, thus being the glue language, and to compute mathematical equations for the use with the database.

3.4.3 Query execution function

All the data are on the database, thus any data analysis function must get the data from the database. Firstly you need a connection to the database. A internet connection is required with the appropriate login details and the table name you want to access in the database.

The option to write and read from the web or local database is given or the query can be sent to both the databases. A flow diagram of the execution function is shown in Figure 3.6. The diagram shows that the function wants to know if the data must be written to the web based database or the local database. It will connect with the required login details and query the database. The query can be sent either to fetch data or write data. The query is committed and the execution is completed.

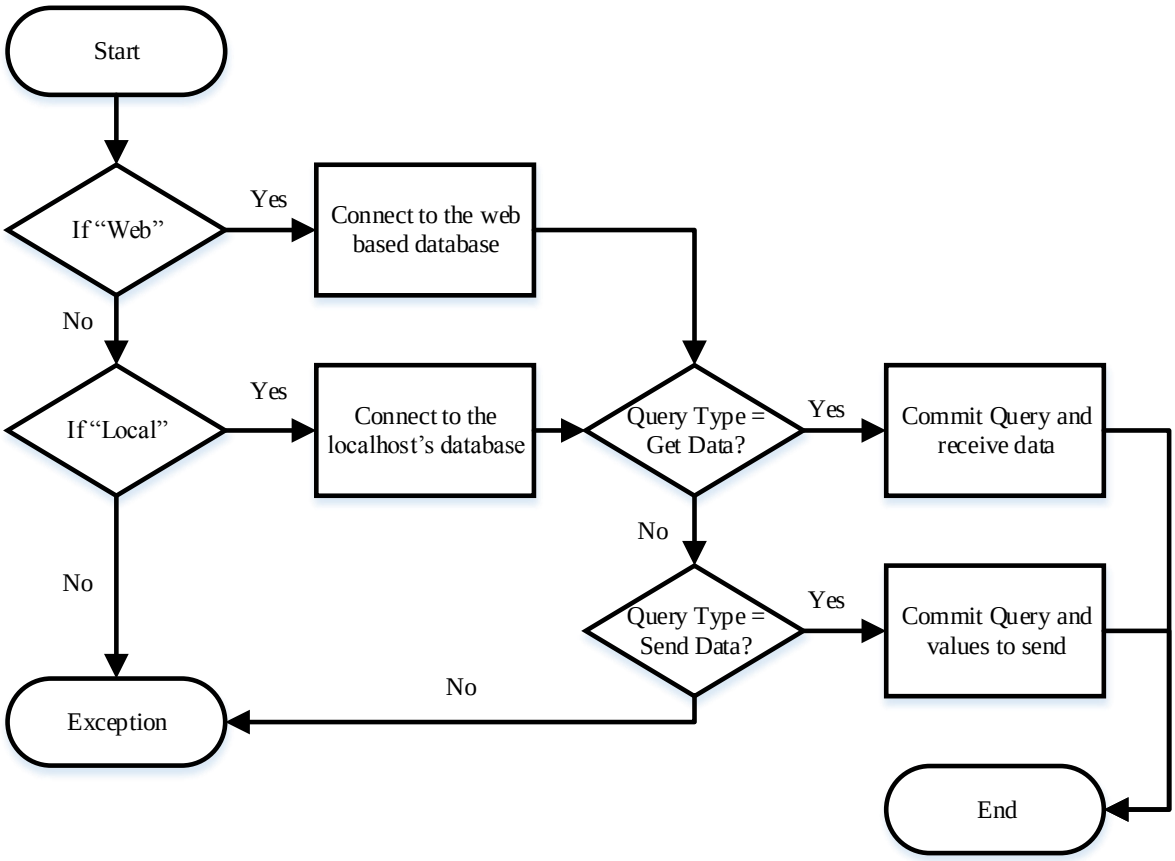

Figure 3.6: Database execution function flow diagram

3.4.4 General Computation

The analysis of the data and the parameter extraction methods, require the data for the algorithms to execute. In the functions the data are accessed with the database execution function, and then executed until the data need to be written back into the database. Thereafter the database execution function is called again.

3.5 Parameter Extraction and Optimisation

The IV-curve of the solar module, which is measured with the active load, is known for 10 minute intervals throughout the day. The five parameters of these IV-curves must be extracted to evaluate the data. To get the exact parameters that present the IV-curve, the single diode model was used. The relationship between the voltage and current of the single diode model is chosen as the governing model because, it is used by the IEC 60891 standard as the standard model in PV due to its accuracy with its simplicity. With the relationship between each parameter the model present, the values were calculated with a combination of curve fitting and optimisation. This process is explained in this section.

The single diode model provides five unknown variables, known as the five parameters: I_O, I_{PH}, R_{SH}, R_S and a. The five unknown parameters can only be solved if five boundary conditions are known. The manufacturers of solar cells provide only the V_{OC}, I_{SC} and the MPP (I_{MPP} and V_{MPP}). Other data about a module that manufacturer's provide, are at STC conditions which are seldom observed in real life operating conditions. Especially

for this study, the variation in irradiance and temperature, and how it influences the parameters are important. This information is not enough to satisfy the five parameter equations and thus there is an initial estimation process that is explained.

3.5.1 Parameter Extraction Method

The boundary conditions for the open circuit voltage and short circuit current are used to lay a foundation for the parameter extraction. The extraction method used, makes use of initial conditions that are approximated and then optimised to fit the measured IV-curve to get the exact parameters. The short circuit equation is shown in equation 3.5.

$$I_{SC} = I_{PH} - I_O\left[e^{\left(\frac{V_T + I_{SC}R_S}{a}\right)} - 1\right] - \frac{V_T + I_{SC}R_S}{R_{SH}} \tag{3.5}$$

Equation 3.5 can be simplified as presented in equation 3.6 by [60].

$$I_{PH} = \frac{R_{SH} + R_S}{R_{SH}} I_{SC} \tag{3.6}$$

The open circuit voltage equation is as follows:

$$0 = I_{PH} - I_O\left[e^{\left(\frac{V_{OC} + I_T R_S}{a}\right)} - 1\right] - \frac{V_{OC}}{R_{SH}} \tag{3.7}$$

Equation 3.7 can be simplified as presented in equation 3.8 [56].

$$I_O = \frac{(R_{SH} + R_S)I_{SC} - V_{OC}}{e^{\left(\frac{V_{OC}}{a}\right)} R_{SH}} \tag{3.8}$$

Equations 3.5 and 3.8 cannot be solved explicitly by using elementary functions. Thus other methods to solve the equation are examined. At a low irradiance the series resistance is high. This causes the exponential part in equation 3.5 and 3.8 to withhold the IV-curve from converging to a solution. The reason for this is that a small variation in the series resistance will cause a big variation in the iterations [39]. The method used in the realisation of this method is the Newton Raphson method. This method is also referred to as Newton's method (equation 3.10). It is a root finding algorithm that makes use of the first few terms of the Taylor series (equation 3.9) of the function $f(x)$. This method can be unstable if the initial choice is not close to the root's position and may keep the result from converging to a solution [63].

$$e^x = f(0)\frac{x^0}{0!} + f'(0)\frac{x^1}{1!} + f''(0)\frac{x^2}{2!} + f'''(0)\frac{x^3}{3!} + \cdots \tag{3.9}$$

$$x_{n+1} = X_n - \frac{f(x_n)}{f'(x_n)} \tag{3.10}$$

The single diode model's equation can be written in the Newton Raphson format as shown in equation 3.11.

$$f(I_T) = 0 = I_{PH} - I_T - I_O\left[e^{\left(\frac{V_T + I_T R_S}{a}\right)} - 1\right] - \frac{V_T + I_T R_S}{R_{SH}} \tag{3.11}$$

The derivative of equation 3.11 is shown in equation 3.12

$$f'(I_T) = -1 - I_O\frac{R_S}{a}\left[e^{\left(\frac{V_T + I_T R_S}{a}\right)} - 1\right] - \frac{R_S}{R_{SH}} \tag{3.12}$$

With the application of Newton Raphson, equation 3.13 is recursively applied to the new value.

$$I_{T(n+1)} = I_{T(n)} - \frac{I_{PH} - I_{T(n)} - I_O\left[e^{\left(\frac{V_T + I_{T(n)} R_S}{a}\right)} - 1\right] - \frac{V_T + I_{T(n)} R_S}{R_{SH}}}{-1 - I_O\frac{R_S}{a}\left[e^{\left(\frac{V_T + I_{T(n)} R_S}{a}\right)} - 1\right] - \frac{R_S}{R_{SH}}} \tag{3.13}$$

The recursive loop is stopped when the difference between two answers is within a tolerance. This tolerance can be adjusted to add accuracy to the convergence.

3.5.2 Approximation

The shunt resistance, R_{SH}, can be approximated by using the first part of the IV-curve. The gradient between point 1 and 2 in Figure 3.7, is calculated for the initial guess. The gradient is calculated by taking the difference in the current, divided by the difference in the voltage at each point as shown in Figure 3.7. The R_{SH} value is the negative inverse of the gradient, but the resistance cannot be negative, so the absolute value is used. Equation 3.14 shows the formula.

$$R_{SH} = \left|\frac{V_2 - V_1}{I_2 - I_1}\right| \tag{3.14}$$

The second part of the IV-curve is used to approximate the series resistance, R_S. The gradient in this part is also used in the same way as with the shunt resistance. The relationship is shown in Figure 3.7 and equation 3.15 gives the formula.

$$R_S = \left|\frac{V_4 - V_3}{I_4 - I_3}\right| \tag{3.15}$$

The cell ideality factor, a, is approximated by equation 3.16. The back of cell temperature measurement, T, is used and converted to Kelvin.

$$a = \frac{nN_S kT}{q}\,, \tag{3.16}$$

where the constants q and k are known. N_S is the number of cells connected in series and n, the diode ideality factor, is estimated to be 1.

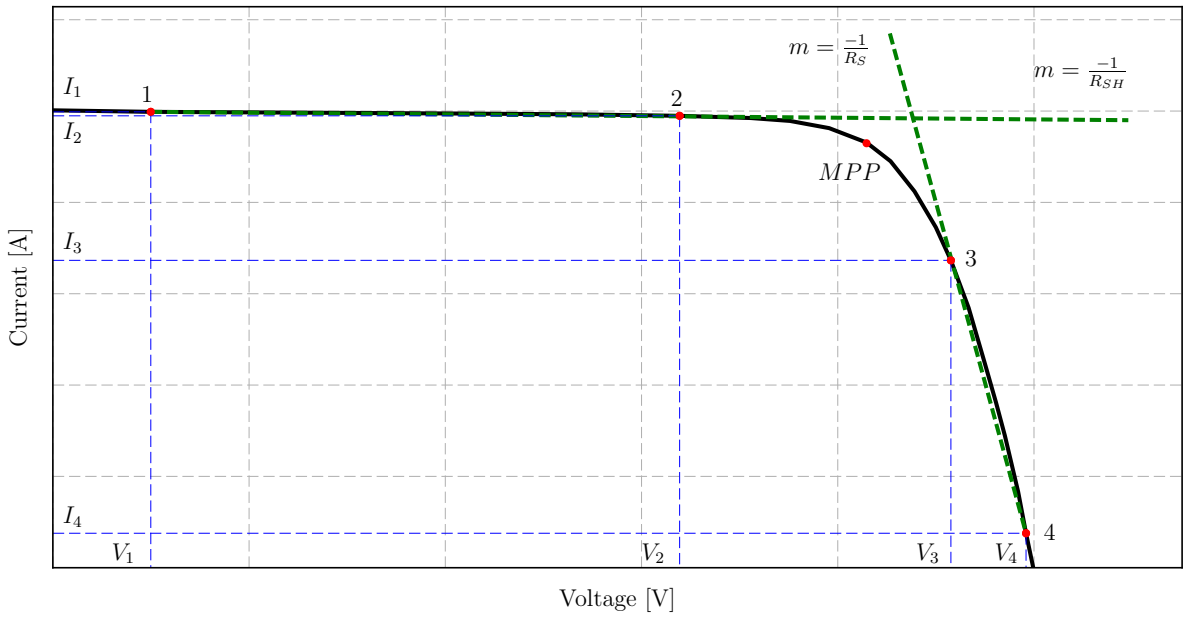

Figure 3.7: Initial parameter approximation from the measured data

3.5.3 Optimisation

The data that the active load provides is a set of 20 data points which represents the IV-curve that was measured. To validate the data and to provide a higher resolution of this data, a curve fitting routine is implemented in Python to do this with the estimated parameters. Curve fitting methods provided as a library in Python, include Savgol filtering, Spline interpolation and various other functions. These functions are general functions and not specifically for IV-curve fitting, thus it does not contribute to the validation of the data.

The optimisation method used in the curve fitting routine, is the Constrained Optimisation BY Linear Approximation (COBYLA) optimisation method. It was found to perform the best in this specific application [51]. Other optimisation methods aim to go through each data point, which is correct with a clear sky measurement, but on an overcast day, the methods result in irregular PV module behaviour. The SciPy library is used to call the optimisation algorithm, called optimize.minimize.

3.5.4 Implementation

The software implementation of the parameter extraction is shown in a flowchart in Figure 3.8.

The Python script begins by fetching a dataset from the database. The extraction process begins by estimating the R_s and R_{SH} values by calculating the gradients of the IV-curve as in equation 3.14 and 3.15. The value of a is approximated by assuming a diode ideality factor of one and a temperature of 30^oC. I_O and I_{PH} can be described in terms of R_S, R_{SH} and a with equations 3.6 and 3.8. The I_{SC} and V_{OC} values measured, are used as the required values in the equations. The optimisation process adjusts these parameters to minimise the difference between the measured and fitted curve. The optimisation process continues until a difference smaller than the predefined tolerance is reached. This

is defined as the convergence tolerance. The iterative process of solving the terminal current is achieved by using the Newton Raphson method. Finally, if the difference is smaller than the tolerance, the answer is reached at convergence.

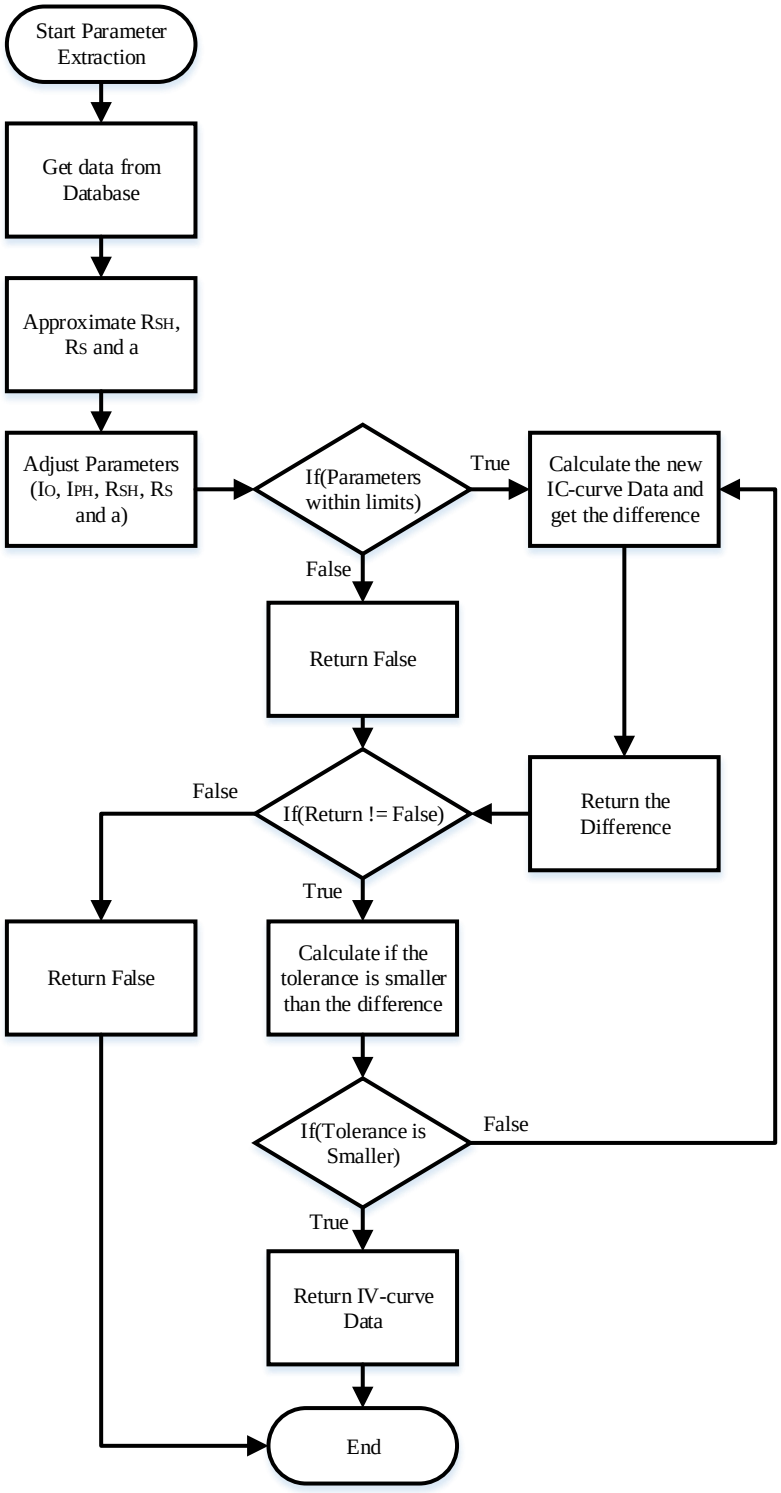

Figure 3.8: Software flowchart of the parameter extraction method

3.5.5 Extraction Result

The result of the parameter extraction is both sufficient and accurate. The convergence of a solution takes time, but with the accuracy shown in Figure 3.10, it is a small price to pay.

3.6 De Soto's Parameter Extraction and Prediction

De Soto's parameter extraction method is a well known and well referenced method [24] [39]. It is known for the advantage of module parameter extraction by using only the module data given by the manufacturer's data-sheet [57]. The method uses data from the data-sheet at standard test conditions (STC). The main assumption made by De Soto is that the series resistance is not dependent on the temperature and irradiance [55]. Semi-empirical equations are used for the prediction of the IV-curve. This method is of interest as it only requires a small amount of input data, thus the implementation of the method can be widely carried out.

3.6.1 Parameter Extraction Model

The effect of irradiance and temperature on the parameters of a solar PV module are given in equation 3.17 - 3.21 [40].

$$\frac{I_O}{I_{O,ref}} = \left[\frac{T_c}{T_{c,ref}}\right]^3 e^{\frac{\epsilon N_s}{a_{ref}}\left(1-\frac{T_{c,ref}}{T_c}\right)} \tag{3.17}$$

$$I_L = \frac{G_T}{G_{T,ref}}\left[I_{L,ref} + \alpha_{I_{SC}}(T_c - T_{c,ref})\right] \tag{3.18}$$

$$R_{SH} = R_{SH,ref}\left(\frac{G_{T,ref}}{G_T}\right) \tag{3.19}$$

$$R_S = R_{S,ref} \tag{3.20}$$

$$a = a_{ref}\left(\frac{T_c}{T_{c,ref}}\right) \tag{3.21}$$

,where G is the irradiance, ϵ is the electron band-gap voltage, N_s is the number of cells in series and $\alpha_{I_{SC}}$ is the temperature coefficient of I_{SC}. To solve these equations, the Newton Raphson method is used.

3.6.2 Implementation of De Soto's Method

De Soto's parameter extraction method's solution for each dataset was calculated and added to the database. To implement De Soto's equations, a reference parameter set is required. Due to manufacturers not providing parameters at STC for this specific module used at the research facility, a measured dataset close to STC was used as reference for this method. The reference parameters used as input for De Soto's parameter prediction equations, are shown in Table 3.5.

Table 3.5: Single Diode Model's Reference Parameters

Parameter	Reference Value	Unit
$I_{L,ref}$	8.5846	A
$I_{0,ref}$	2.3092×10^{-9}	A
$R_{SH,ref}$	160.869	Ω
$R_{S,ref}$	0.33066	Ω
a_{ref}	1.06024	
$T_{c,ref}$	27.69	^oC
$G_{T,ref}$	1000	W/m^2

A flow diagram of the implementation is shown in Figure 3.9. Each dataset measured has an ID. This ID is used as identification of the dataset in the implementation. Firstly, the function looks if the ID has an available dataset. If the dataset is available the temperature and irradiance is imported and used with the five parameter equations to adjust the parameters. The parameters is then sent to the database. This process repeats until all the entries in the database are serviced.

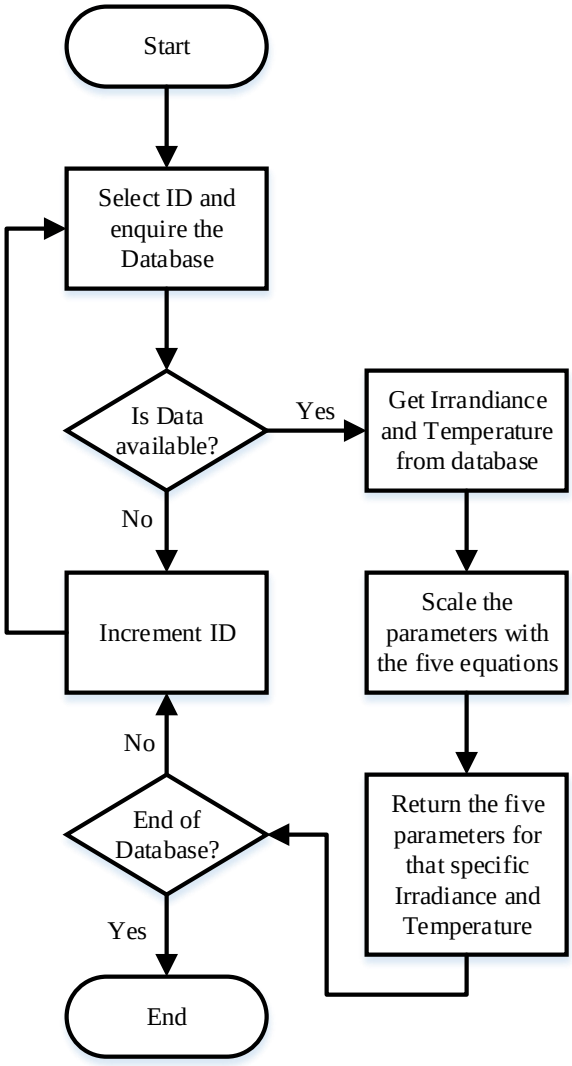

Figure 3.9: Flow diagram of the implementation of De Soto's method

3.6.3 Parameter Comparison

With the data for the study in place, the comparison between the measured data and parameters calculated, using De Soto's method applied to the single diode model, could be done. The database was updated with the percentage error between the MPP of each dataset's actual IV-curve and predicted IV-curve found with the use of equation 3.22. The data were analysed by looking at the influence that the temperature and irradiance had on the error made by De Soto's method.

In Figure 3.10 the difference in the IV-curves between the measured data and De Soto's parameters applied to the single diode model, are shown at different irradiance and temperature conditions. The dots represent the actual measured data which are then fitted with the single diode model to give the parameters of the dataset. A curve that is above or below the dotted curve is the result of De Soto's method.

As is shown in Figure 3.10, the prediction is quite accurate at conditions near the reference. The reason for this is that the parameter set given for this method is at these same conditions, thus because the prediction is almost at the same conditions, it must be close to the parameter set given. The prediction overestimates the performance at $G = 500\,W/m^2$

and underestimates the performance at $G = 250\,W/m^2$. This will differ from dataset to dataset, as each dataset has unique environmental conditions which influence De Soto's equations differently.

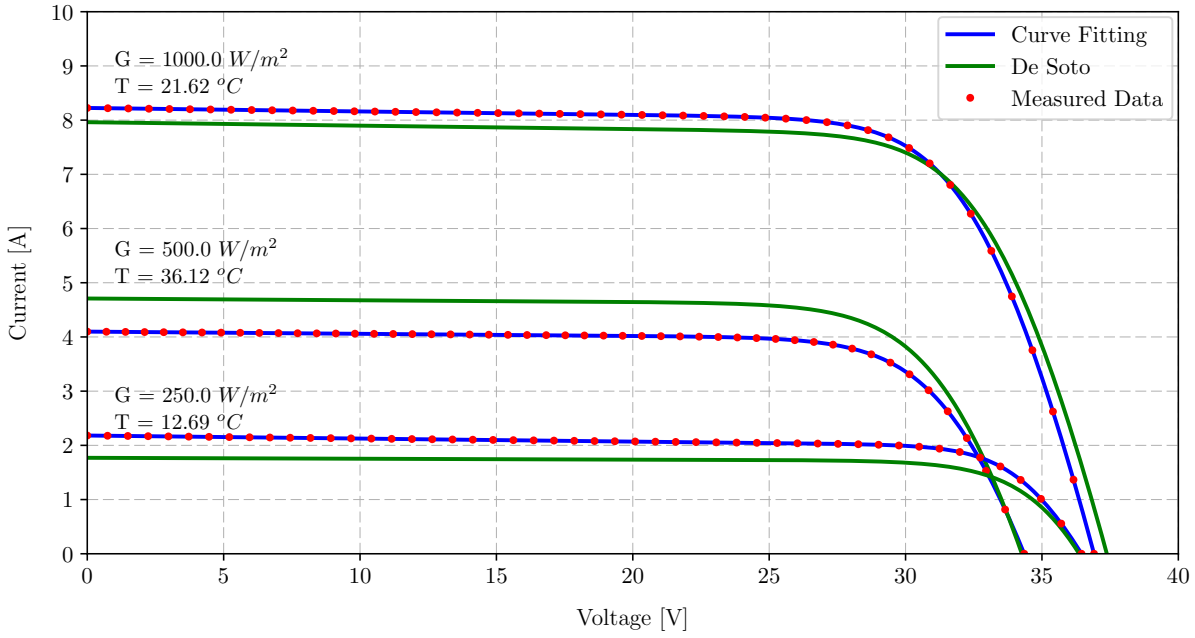

Figure 3.10: Comparison between De Soto's method and the measured data at different irradiance and temperature conditions

The percentage error was intensively studied and a relationship between the error, temperature and irradiance was observed. This observation becomes evident in the following section. An adjustment to the predicted MPP was made by the derivation of a linear function. The influence of the adjustment on the percentage error was obtained and the improvement is shown with a histogram in Figure 3.11.

3.7 Parameter Extraction Results

The maximum power point (MPP) of the measured IV-curve is calculated and used as a reference, referred to as MPP_{ref}, to compare to the MPP of the implementation of De Soto's parameters, referred to as MPP_{deSoto}. The error is calculated as a percentage with the equation in 3.22.

$$\%_{error} = \frac{MPP_{deSoto} - MPP_{ref}}{MPP_{ref}} \times 100 \tag{3.22}$$

The percentage difference was calculated for each dataset in the database and is shown in histogram form in Figure 3.11. In Figure 3.11 it is shown that the performance prediction overestimates the actual performance. The average error made using De Soto's parameters is 13.71 %.

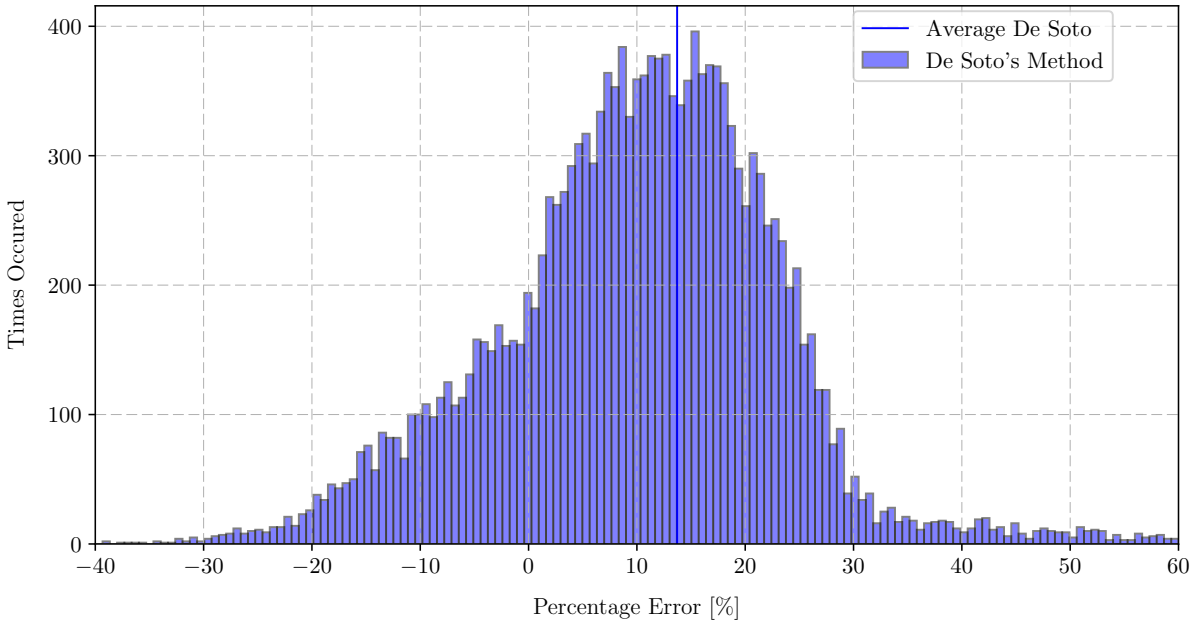

Figure 3.11: Histogram of the percentage error De Soto's method makes to measured data

The predicted performance is interesting as its median is well above the actual performance. Thus, if you use De Soto's parameters to predict the performance of this specific site, the predicted performance will be above the actual performance.

The data were studied further to look for a relationship in the percentage error De Soto's method makes compared to the measured data. It was found that there is a linear relationship of the percentage error to irradiance and temperature. This relationship is presented in this section.

3.7.0.1 Temperature Error

The temperature percentage error referred to, is the dominant factor in the difference between the measured performance and the predictive performance. The linear relationship in Figure 3.12 as well as the trend-line for the data are shown.

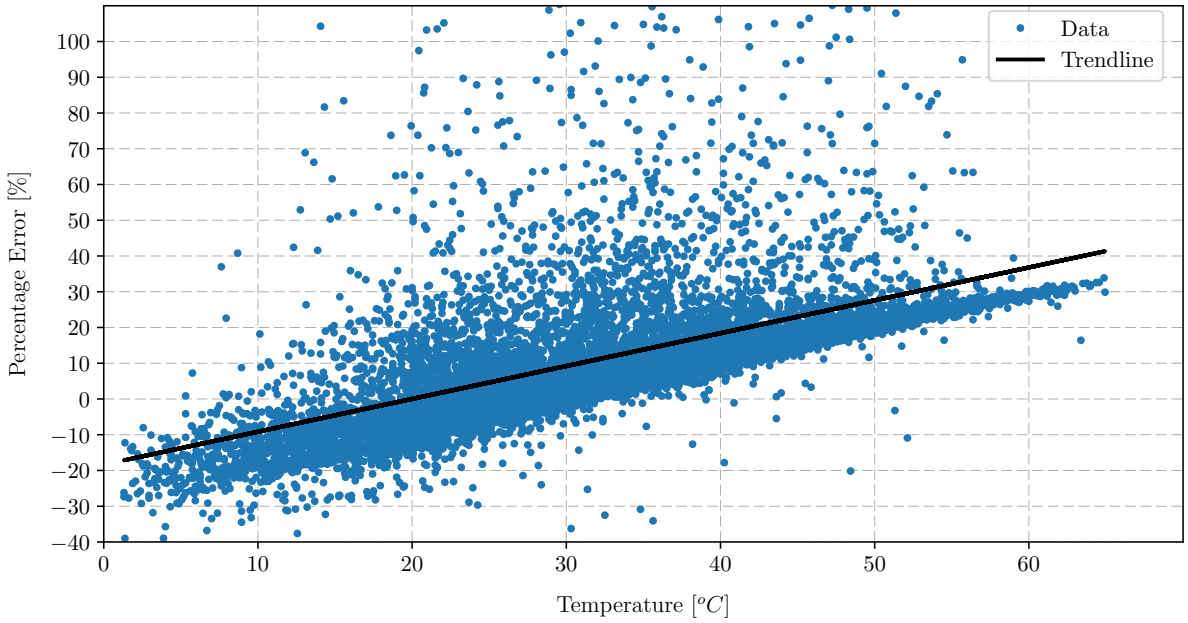

Figure 3.12: Influence on the percentage error with temperature

3.7.0.2 Irradiance Error

The irradiance error does not have a big influence on the percentage error, but is incorporated in the adjustment function to add the influence that it has. Although the difference is more scattered than in the case of temperature, a linear relationship can be defined. Figure 3.13 shows the relationship and the trend-line.

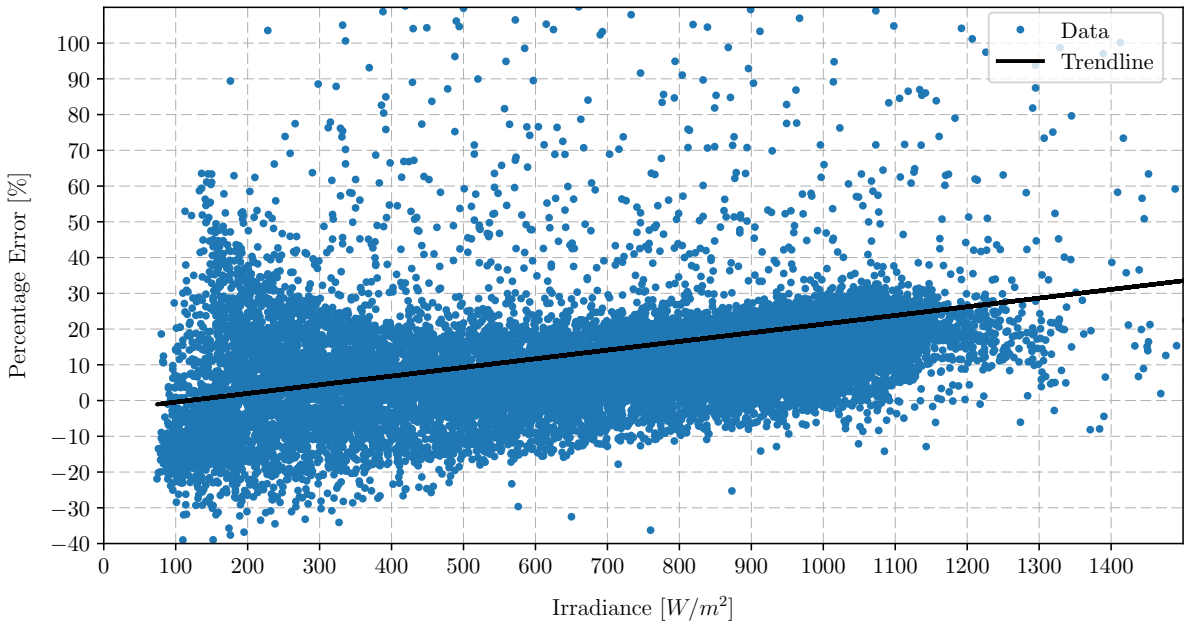

Figure 3.13: Influence on the percentage error with varying irradiance

3.7.1 Error Adjustment

The data presented above, were plotted in 3D to see the effect that relationship, temperature and irradiance had on the percentage error. A curve fitting routine in Matlab is used to fit a plane, with the form as in equation 3.23, to the data points. Matlab was used, because it was found to have the most user friendly approach. The equation of the plane gives an approximate error relationship. In Figure 3.14 the 3D Matlab plot is shown.

$$y(T, G) = aT + bG + c \tag{3.23}$$

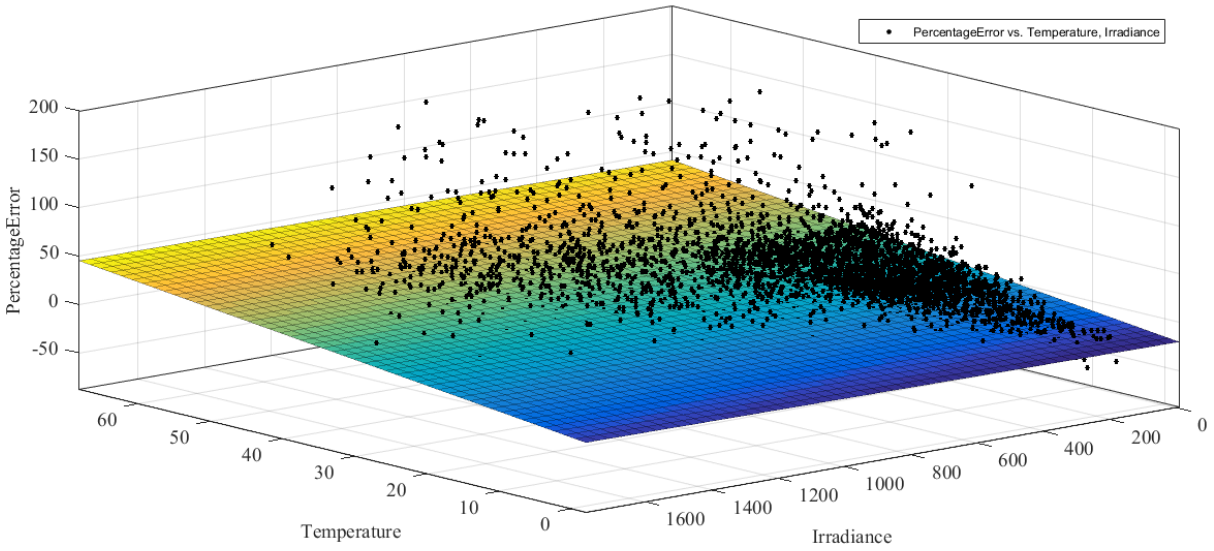

Figure 3.14: 3D curve fitting with Matlab

The error which the implementation of De Soto's parameters in the single diode model has on the test facility's actual performance in Kalkbult is of concern. The performance error can however be corrected by adjusting the performance with the adjustment function derived from the data.

The linear plane's coefficients are:

$$a = 0.8772,$$
$$b = 0.00221,$$
$$c = -18.41,$$

which result in equation 3.24.

$$y(T, G) = 0.8772T + 0.00221G - 18.41 \tag{3.24}$$

The equation is then applied by multiplying the function with the power from the single diode model using De Soto's parameters. These results are an adjustment that can be positive or negative, to be subtracted from the predicted power to give the final power.

$$P(T, G) = P_{DeSoto} - P_{DeSoto}\frac{y(T, G)}{100} \tag{3.25}$$

The adjustment on the predicted performance was applied to the data and the histogram in Figure 3.15 shows that the percentage error was reduced and that the median of this bell shape is closer to zero. The average is still -2.99%, which makes the method with the adjustment comparable with methods which require much more input data [55]. Figure 3.16 shows the improvement on the method. De Soto's method has an average overestimation of 13.71 %, compared to the adjustment on the method with an underestimation of -2.99 %.

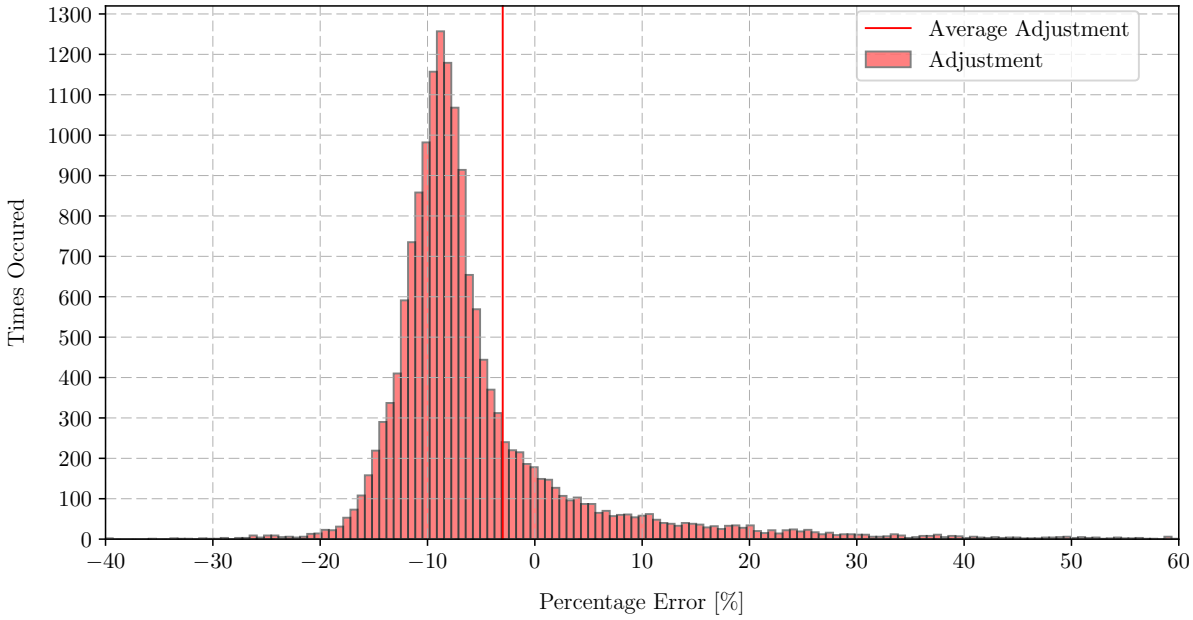

Figure 3.15: Histogram of the percentage error after the adjustment function is applied to De Soto's method

3.7.2 Adjustment Optimisation

The adjustment function was optimised with an iterative optimisation method by adjusting the constant and dependent values to give an average error as close to zero as possible. After the optimisation, the adjustment function to the outcome of the single diode model with De Soto's parameters is shown in equation 3.26.

$$y(T, G) = 0.8T + 0.0025G - 18.41 \tag{3.26}$$

The optimisation of the adjustment is shown in Figure 3.16 with the average error now only -0.062 %.

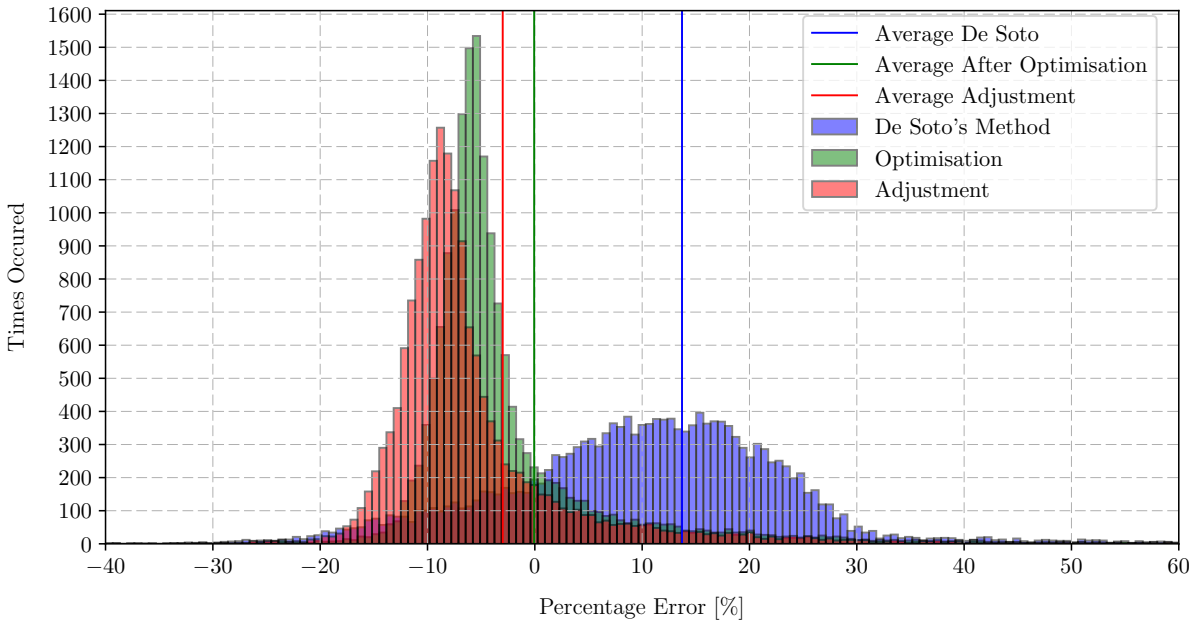

Figure 3.16: Percentage error of De Soto's method compared to the error in the adjustment to the method

3.7.3 Verification Study

The data from a single clear sky day, 31 January 2017, is utilised when creating a comparison between the power produced for this day and the different methods used for forecasting. The day's data were taken from 8:00 to 17:00 and the difference in energy is shown in Table 3.6. The output for the day is shown in Figure 3.17. The power variation throughout the day is shown on the left axis and the temperature throughout the day is shown on the right axis.

Table 3.6: Comparison

Data	kWh	Error to Measured
Measured	1620.04	0%
De Soto	2115.76	30.60%
Adjustment	1519.00	−6.24%
Optimisation	1602.03	−1.11%

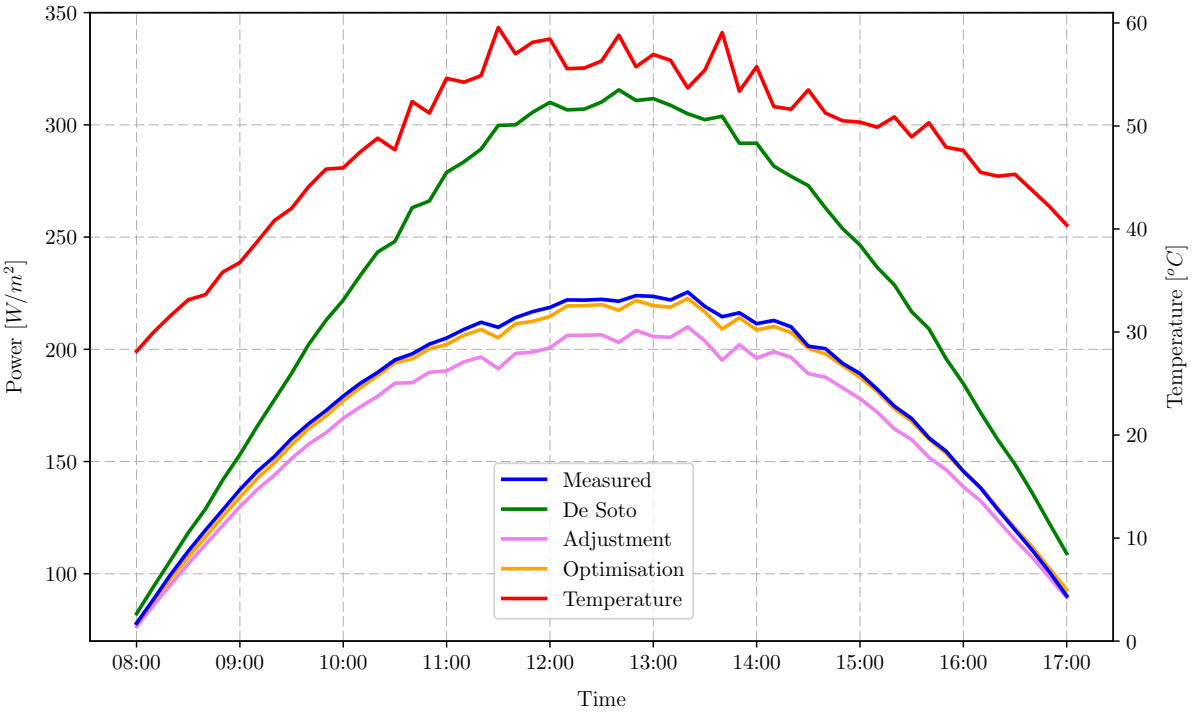

Figure 3.17: Comparison of the day's power with different methods

3.8 Individual Parameters

In this section the parameters are individually evaluated against the actual parameter values, to improve the parameter extraction of De Soto's method. Each parameter is shown against the actual value to indicate the error made with De Soto's method. This section forms an in depth analysis of the PV parameters and their influence on the output power. A new set of improved parameter equations are presented with the improvement in performance prediction shown with the actual data.

3.8.1 Error Calculation

The error made by the prediction, with the actual parameter values as reference, is calculated with the equation that is shown in equation 3.27.

$$Error = \frac{X_{para} - X_{actual}}{X_{actual}} * 100\% \,, \tag{3.27}$$

where X_{para} is the predicted parameter under investigation and X_{actual} is the actual parameter.

These errors for each dataset are summed together and divided by the total amount of entries to give the average error. This error is given at each parameter when it is discussed. For the improved parameter equations this error is calculated again to give the new error relationship. Keep in mind that the visual data correlation in this section does not mean a better actual point to point improvement. Thus the average percentage error is very important in addition to the visual inspection.

The approach followed to improve on the parameter extraction of De Soto's method, was to adjust his equations to fit the actual data more closely visually and especially with regards to the average percentage error. This meant including terms and removing some. Limits were also added for certain parameters. With the iterative optimisation it was important that the relationship does not introduce new constants, but rather dependencies on known irradiance and temperature values at a specific dataset. It was observed that the more accurate a parameter is predicted, thus a better percentage error, does not necessary mean the same improvement on the output power. The reason for this is that each parameter has a different weight of influence on the IV-curve.

3.8.2 Series Resistance

The series resistance is chosen as a constant in De Soto's method. The constant value is determined with the use of an IV-curve at STC. The value for the series resistance is, $R_S = 0.33066\ \Omega$. This is not the actual behaviour of the solar module as is evident in Figure 3.18 and 3.19, which show the relationship of the series resistance parameter. It has a varying value if evaluated against temperature and irradiance. The series resistance tends to be higher at lower temperature values. The fact that the short circuit current increases with the increase in temperature, supports this observation. At a low irradiance, the series resistance becomes exponentially higher.

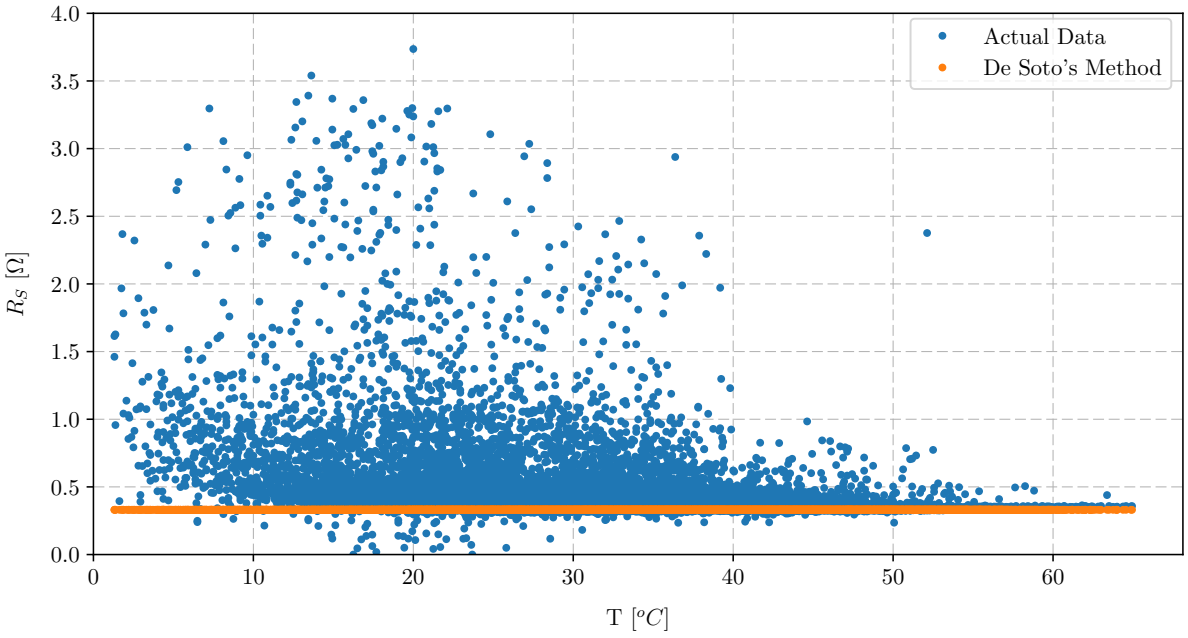

Figure 3.18: The relationship between the actual series resistance and De Soto's method evaluated with varying temperature

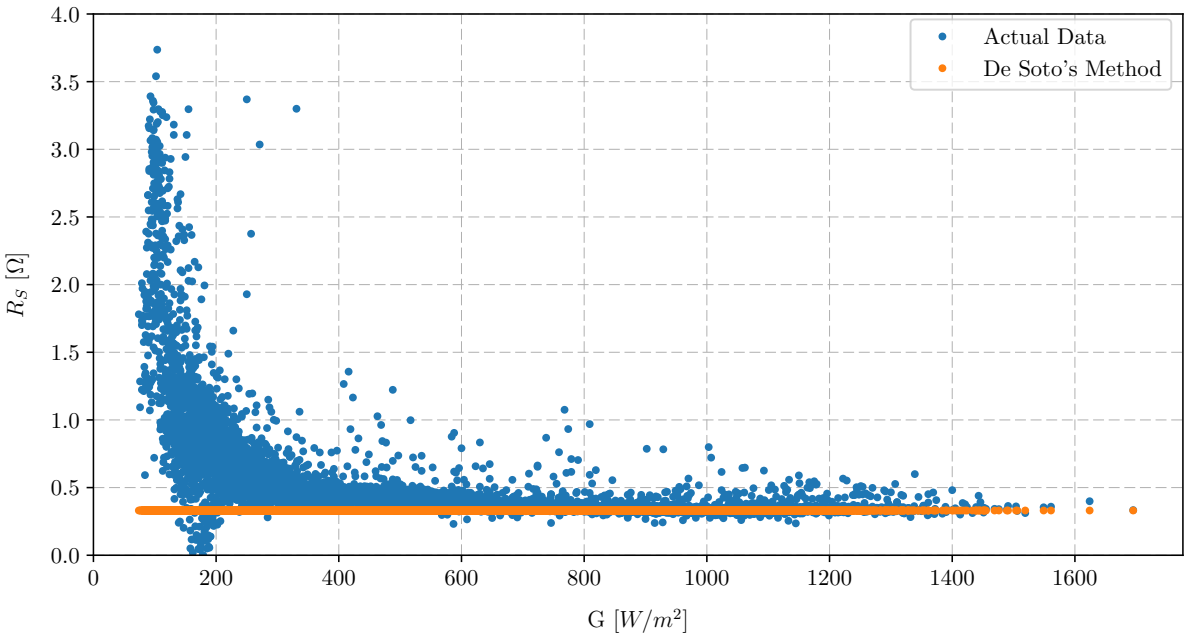

Figure 3.19: The relationship between the actual series resistance and De Soto's method evaluated with varying irradiance

With the result, it is evident that a better series resistance extraction equation, rather than the constant value, is needed to accurately extract the value. A curve with irradiance dependences are developed through iterative optimisation that represents the data more clearly. The curve equation is given in equation 3.28. The equation includes a limit where the series resistance is capped to the reference series resistance. Figure 3.20 and 3.21 show the new relationship that the series resistance parameter has against varying temperature and irradiance, for both the actual and the new estimated parameter. The new relationship improves the percentage error accuracy from -17.231% to only -2.513%. Thus with the use of equation 3.28, the extraction of the parameter's accuracy will increase by 14.7 %.

$$R_S = R_{S,ref}\left(\frac{G_{T,ref}}{2G_T}\right) \tag{3.28}$$
$$R_S < R_{S,ref} : R_S = R_{S,ref},$$

where $R_{S,ref}$ is the reference series resistance from STC conditions, $G_{T,ref}$ is the reference irradiance and G_T is the irradiance at the dataset for which the series resistance is required.

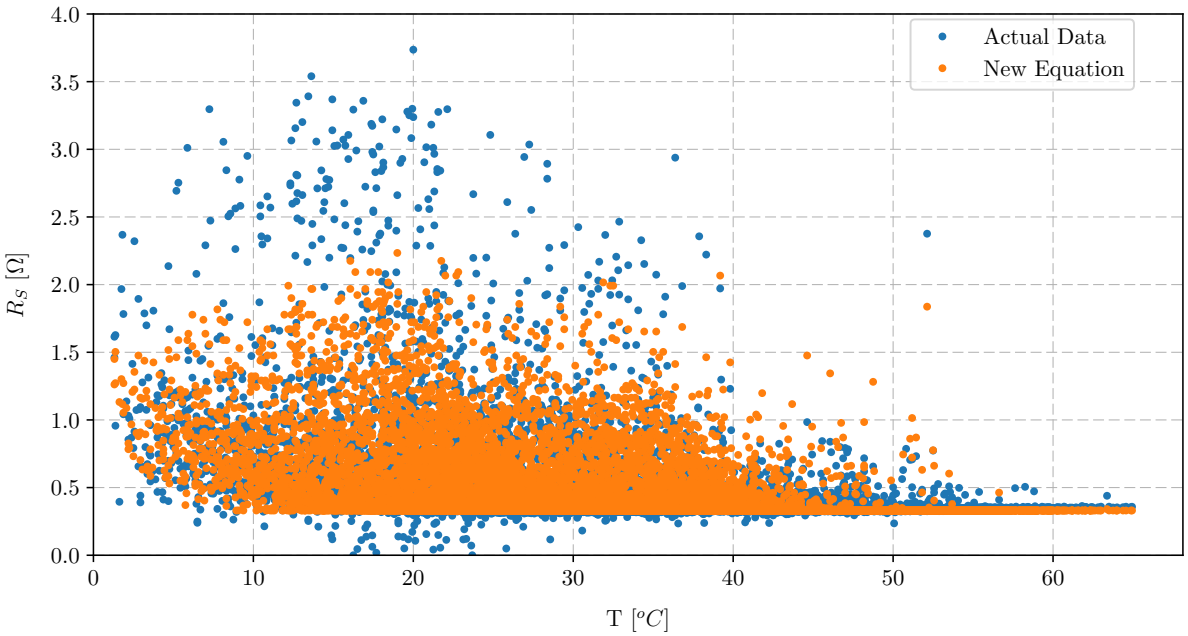

Figure 3.20: The relationship between the actual series resistance and the improvement on De Soto's method evaluated with varying temperature

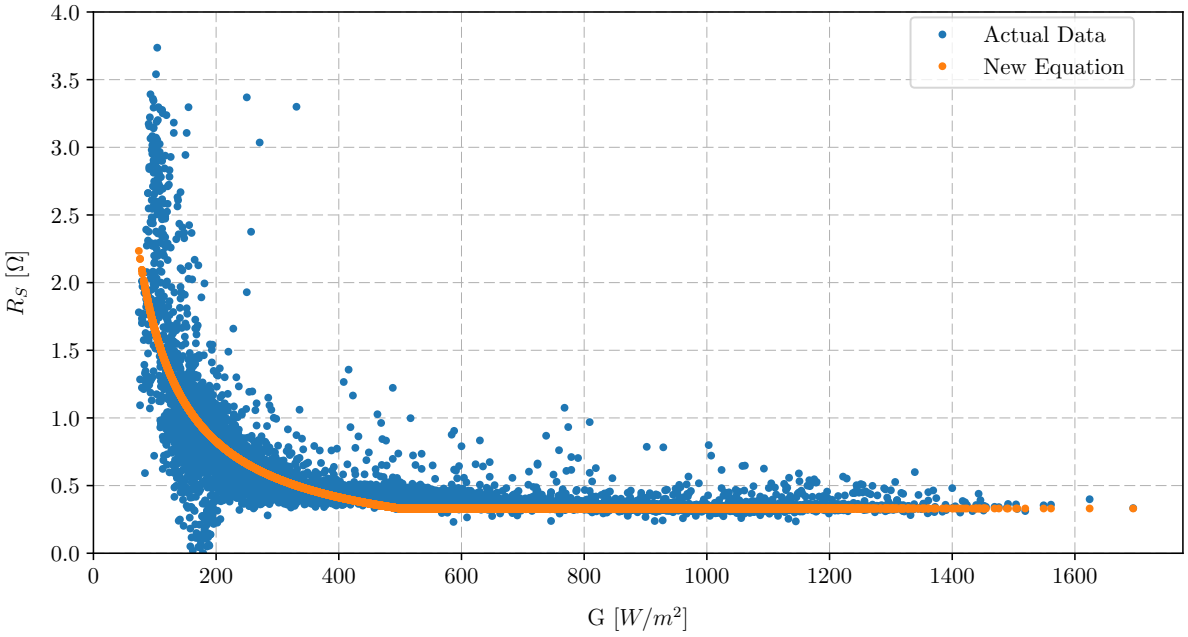

Figure 3.21: The relationship between the actual series resistance and the improvement on De Soto's method evaluated with varying irradiance

The influence of the improvement on the series resistance on the total output power, is small. With the estimation of a constant value which De Soto's method recommends, the error percentage was 13.714 %. The new parameter relationship only improves the error percentage to 13.157%. The improvement is shown in the histogram in Figure 3.22. As the influence is very small. the constant value that De Soto's method predict can be used

to simplify the calculations. The new parameter equation can be used if the specific value of the series resistance is of importance.

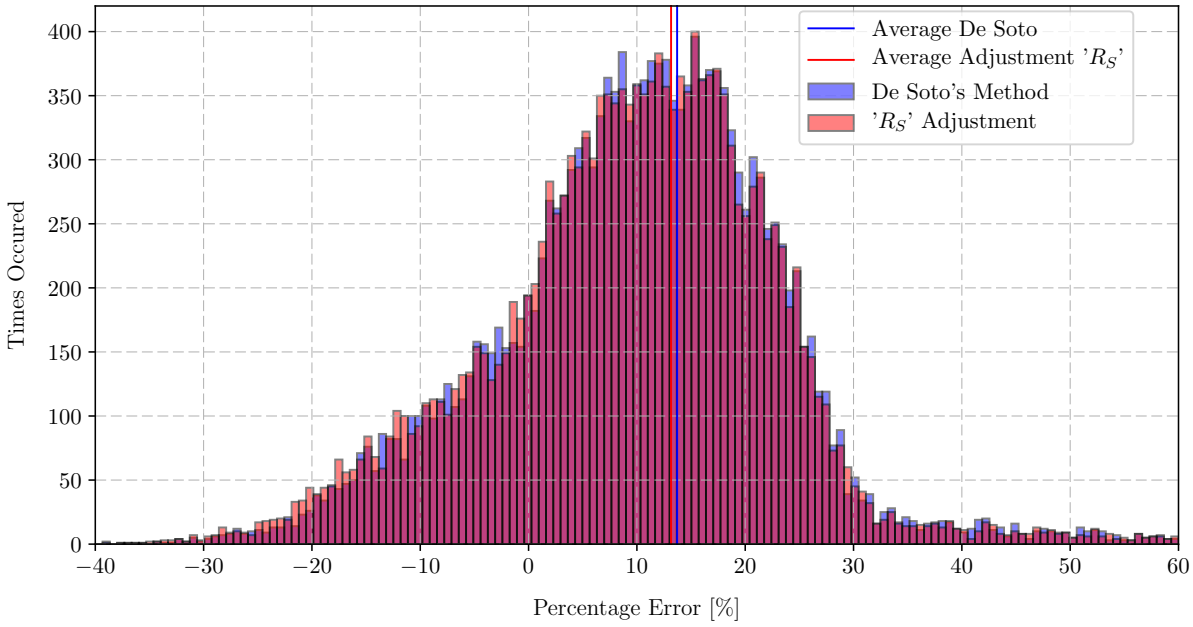

Figure 3.22: Histogram of the percentage error De Soto's method makes to the actual power, compared to the new series resistance parameter relationship

3.8.3 Shunt Resistance

Figure 3.23 and 3.24 show the relationship of the shunt resistance parameter against varying temperature and irradiance, for both the actual and De Soto's parameter. The shunt resistance is clearly overestimated by De Soto's method and is scattered. A higher shunt resistance is better, but it is clear that the resistance is not as high as De Soto's method extracts.

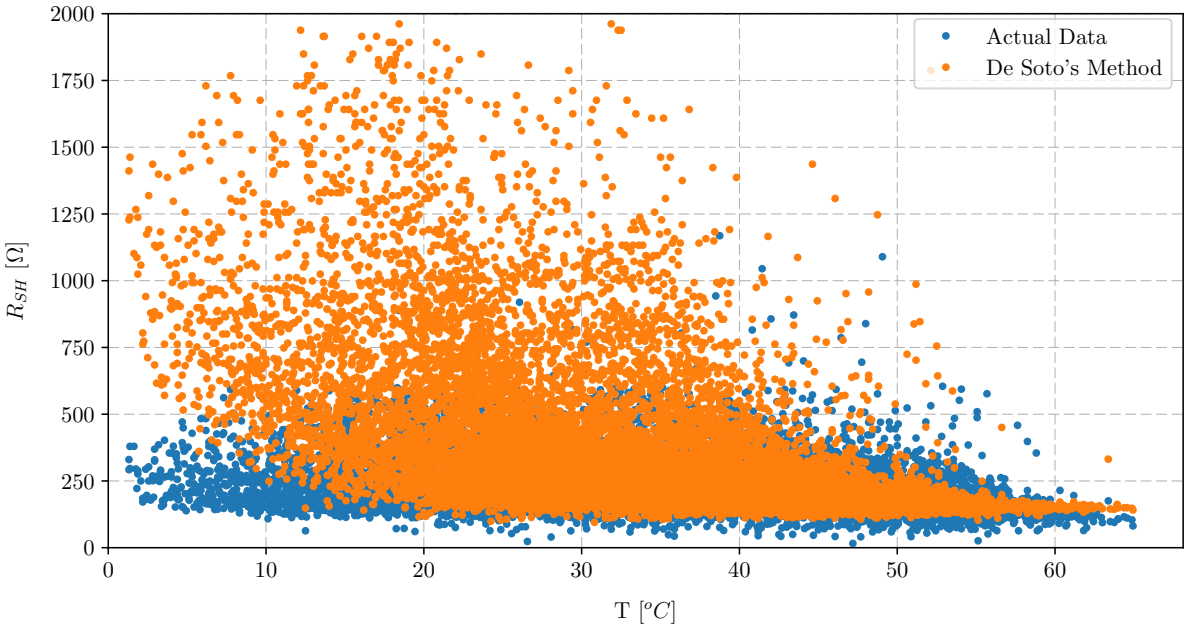

Figure 3.23: The relationship between the actual shunt resistance and De Soto's method evaluated with varying temperature

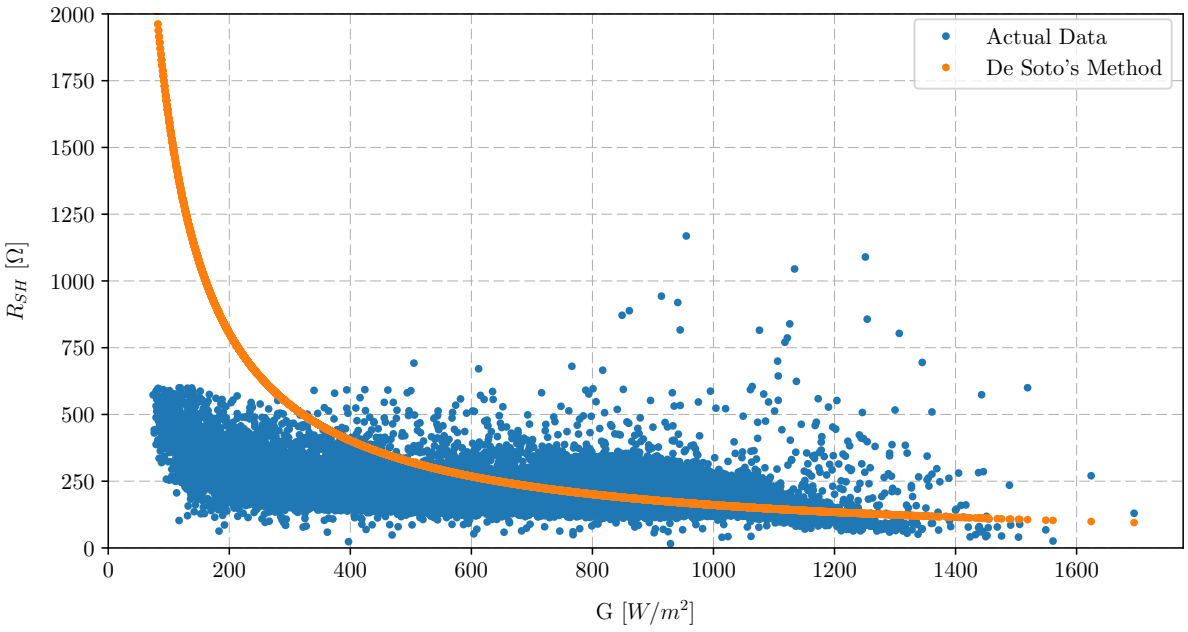

Figure 3.24: The relationship between the actual shunt resistance and De Soto's method evaluated with varying irradiance

The parameter can be estimated by a straight line with the same effect of the curve of the equation given. A straight line with a gradient was fitted to the irradiance axis of the data and was used to get the influence that the shunt resistance has on the output power. The equation of the fitted data is shown in equation 3.29. Figure 3.25 and 3.26 show the new relationship of the shunt resistance parameter against varying temperature

and irradiance, for both the actual and new estimated parameter. The new parameter equation increased with accuracy from 52.218 % to 18.169 %.

$$R_{SH} = -0,1248G_T + 324,38\,, \tag{3.29}$$

where G_T is the measured irradiance of a specific dataset.

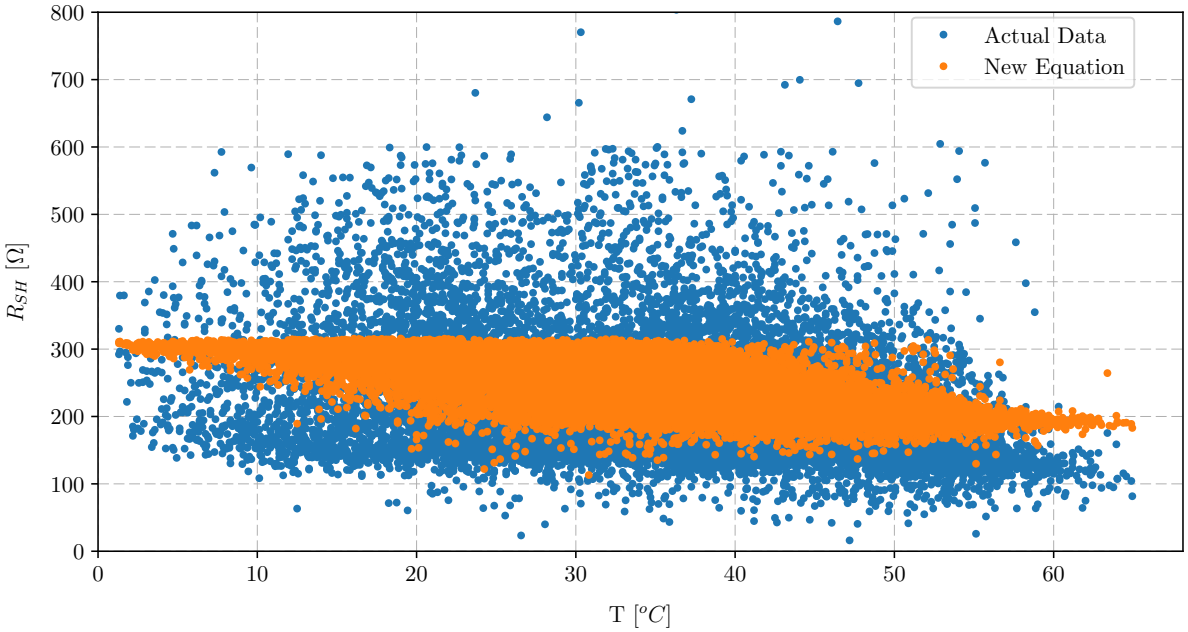

Figure 3.25: The relationship between the actual shunt resistance and the improvement on De Soto's method evaluated with varying temperature

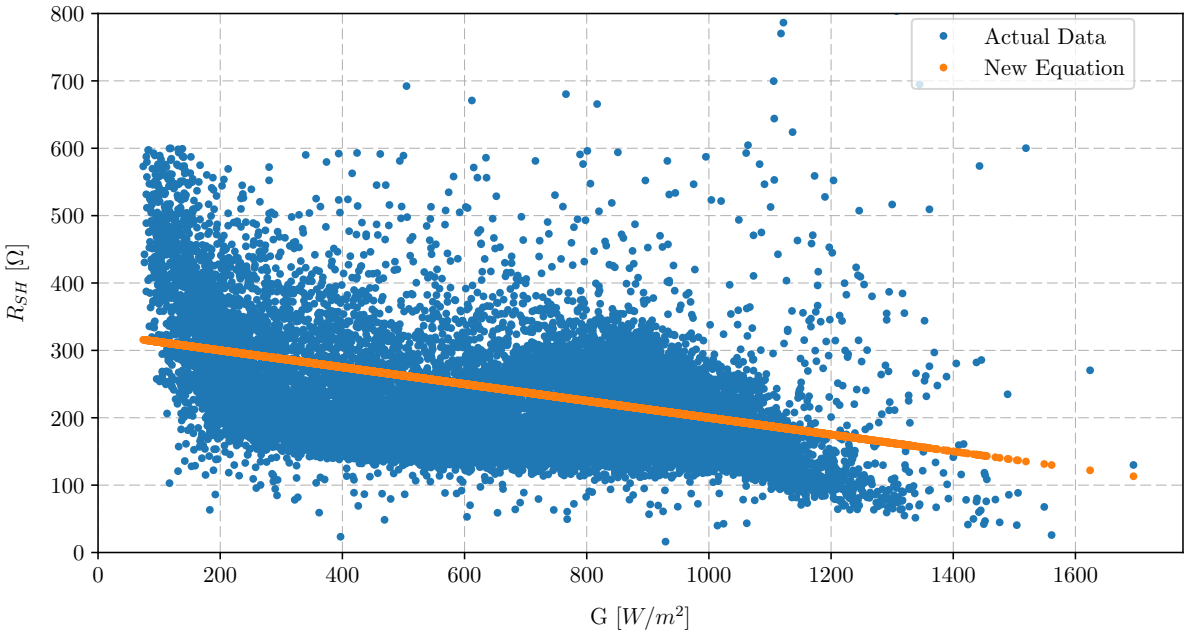

Figure 3.26: The new relationship between the actual shunt resistance and the improvement on De Soto's method evaluated with varying irradiance

The influence that the increase in accuracy of the shunt resistance parameter has on the total output power, is calculated and shown in Figure 3.27. The histogram representation of the percentage error only shows an increase in accuracy from 13.714 % to 12.918 %. Thus the increase in parameter extraction accuracy does not have a significant influence on the output power of a PV module.

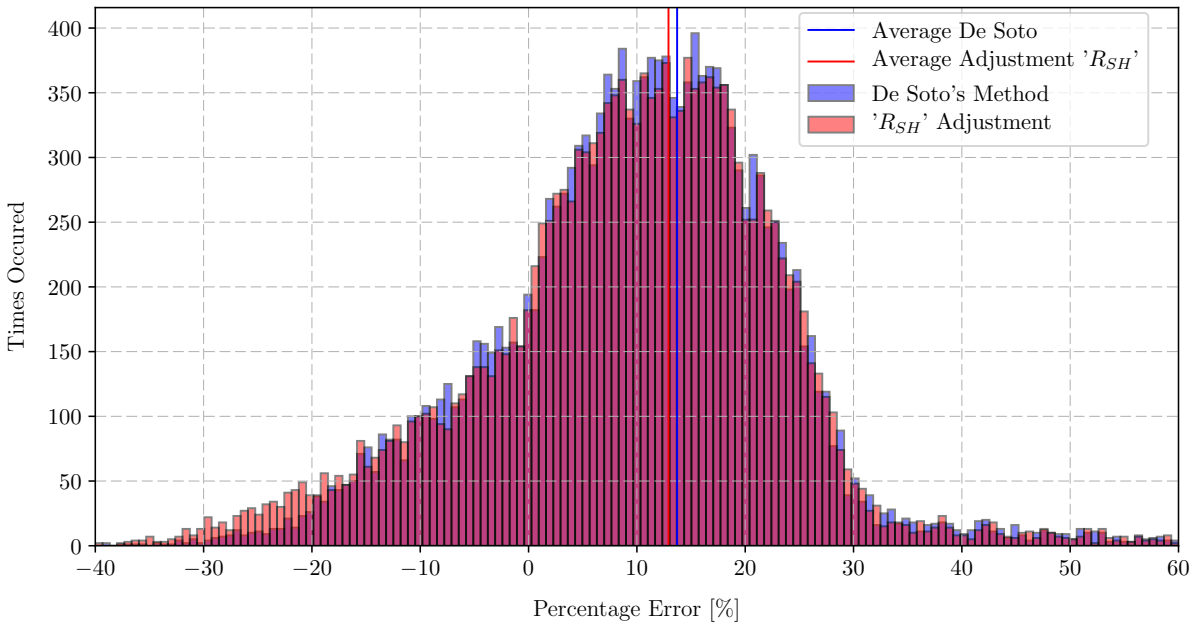

Figure 3.27: Histogram of the percentage error De Soto makes to the actual power compared to the new shunt resistance parameter relationship

The shunt resistance can be estimated as the mean of all the shunt resistance values, because this is seen to give a comparable result. This mean value is 224.27 Ω. The difference in the constant shunt resistance value and the actual value for R_{SH} is 13.98 %, which is also better than the 18.169% of the gradient trend line constant. At this stage, the series and shunt resistance can be chosen as constant values at STC and used throughout the varying range of irradiance and temperatures, because the result of better accuracy in the parameters do not increase the accuracy of the output power as much.

3.8.4 Photo Current

The parameter is a representation of the light that falls on the solar module. From visual inspection it can be seen that De Soto's method overestimates the actual data with a gradient that is higher than the actual data. The average percentage error made is calculated as 13.376 %. Figure 3.28 and 3.29 show the relationship of the photo current parameter against varying temperature and irradiance, for both the actual and De Soto's parameter.

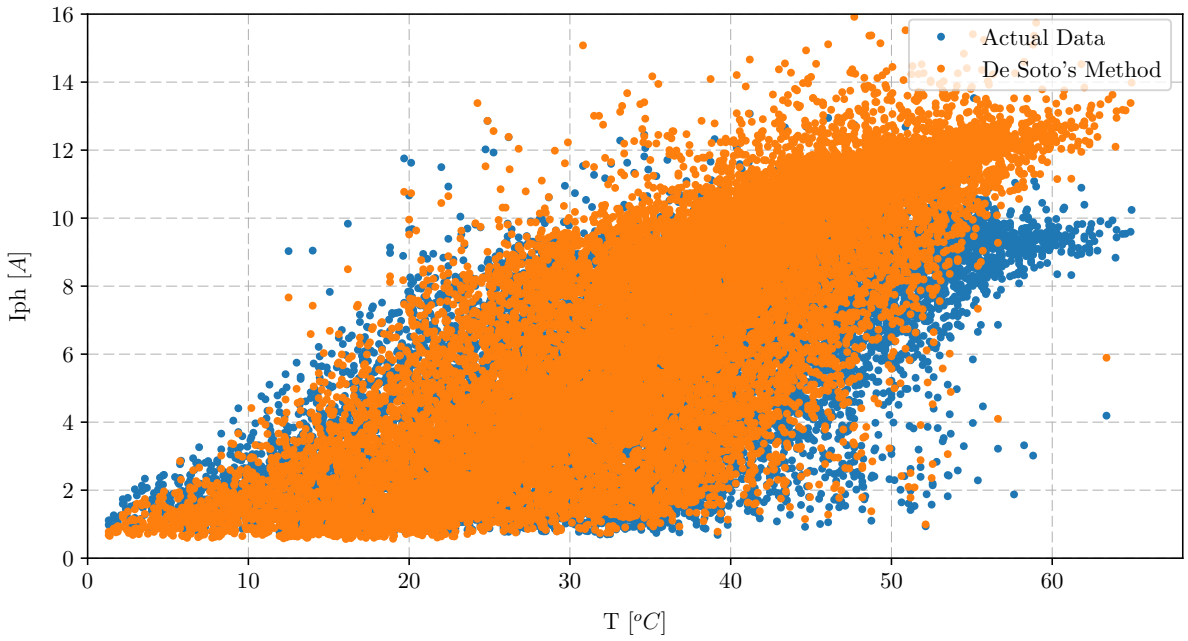

Figure 3.28: The relationship between the actual photo current and De Soto's method evaluated with varying temperature

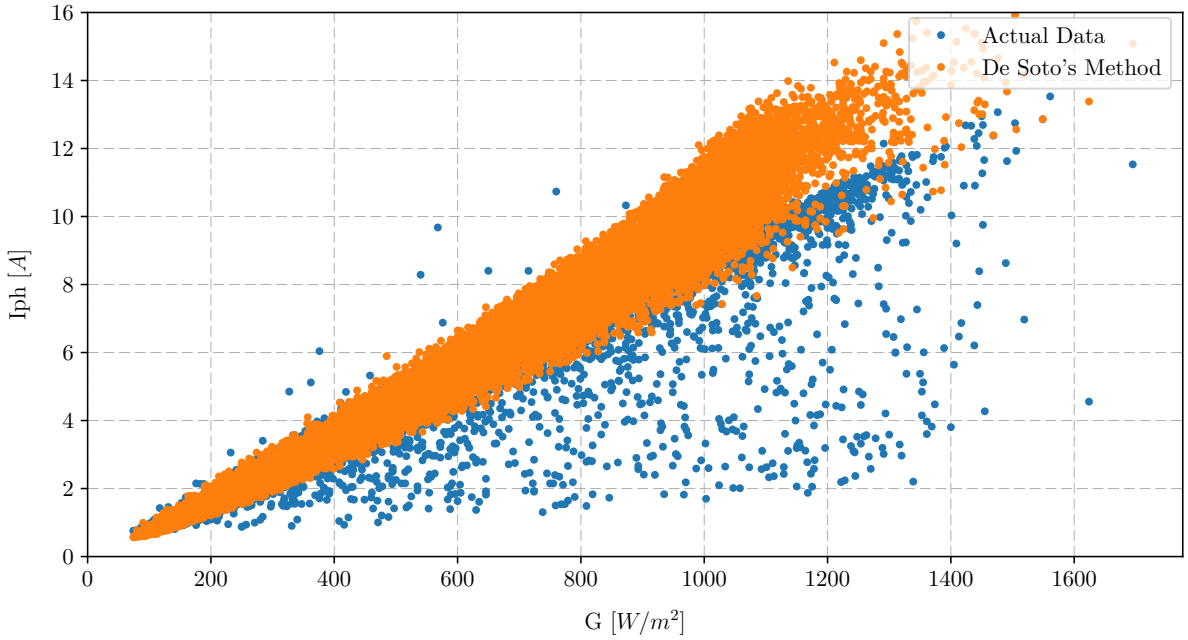

Figure 3.29: The relationship between the actual photo current and De Soto's method evaluated with varying irradiance

With further investigation, it was observed that the temperature coefficient added to the equation that De Soto's method presents, is the factor that contributes to the overestimation of the data. When this factor was removed from the equation, the data looked more accurate visually. The calculated error, after the temperature coefficient was removed,

improved to 4.783 %. The new equation for the photo current parameter is shown in equation 3.30.

$$I_{PH} = \frac{G_T}{G_{T,ref}}\left(I_{PH,ref}\right), \tag{3.30}$$

where G_T is the measured irradiance, $G_{T,ref}$ is the reference irradiance from STC and $I_{PH,ref}$ is the reference photo current at STC.

Figure 3.30 and 3.31 show the new relationship of the photo current parameter against varying temperature and irradiance, for both the actual and the new estimated parameter. The data correlates to the new equation for the photo current.

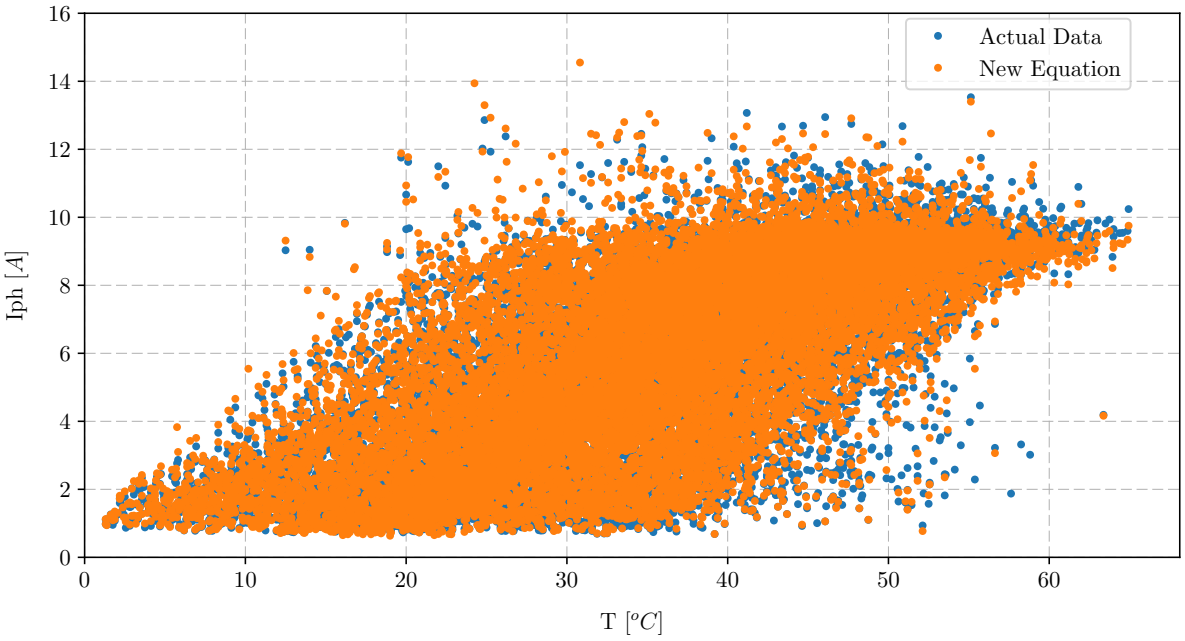

Figure 3.30: The relationship between the actual photo current and the improvement on De Soto's method evaluated with varying temperature

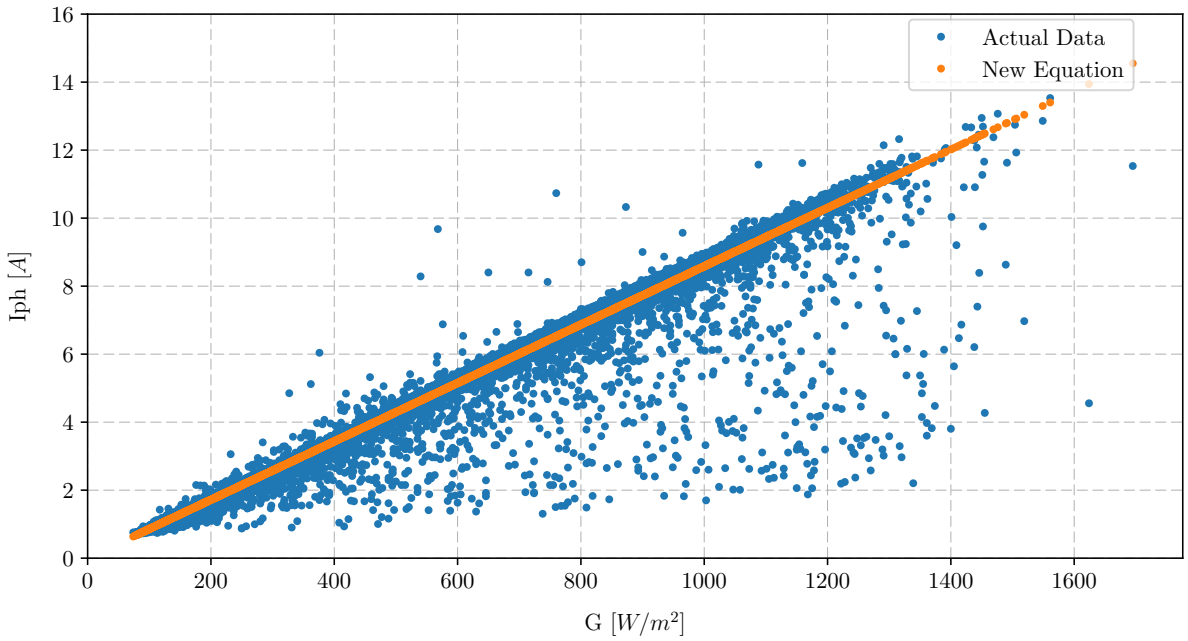

Figure 3.31: The relationship between the actual photo current and the improvement on De Soto's method evaluated with varying irradiance

As mentioned, the parameter may increase accuracy, but may also have a insignificant influence on the output power, thus the influence that the new parameter equation has on the output power, was calculated. The percentage error before the new relationship was 13.714 % and it improved to 5.617 % without the temperature coefficient. Figure 3.32 shows a histogram of the percentage error made by De Soto, compared to the actual output power and the improved relationship's positive influence on the error. The shape of the histogram's distribution of the error on the output power is typically what you want the data to show.

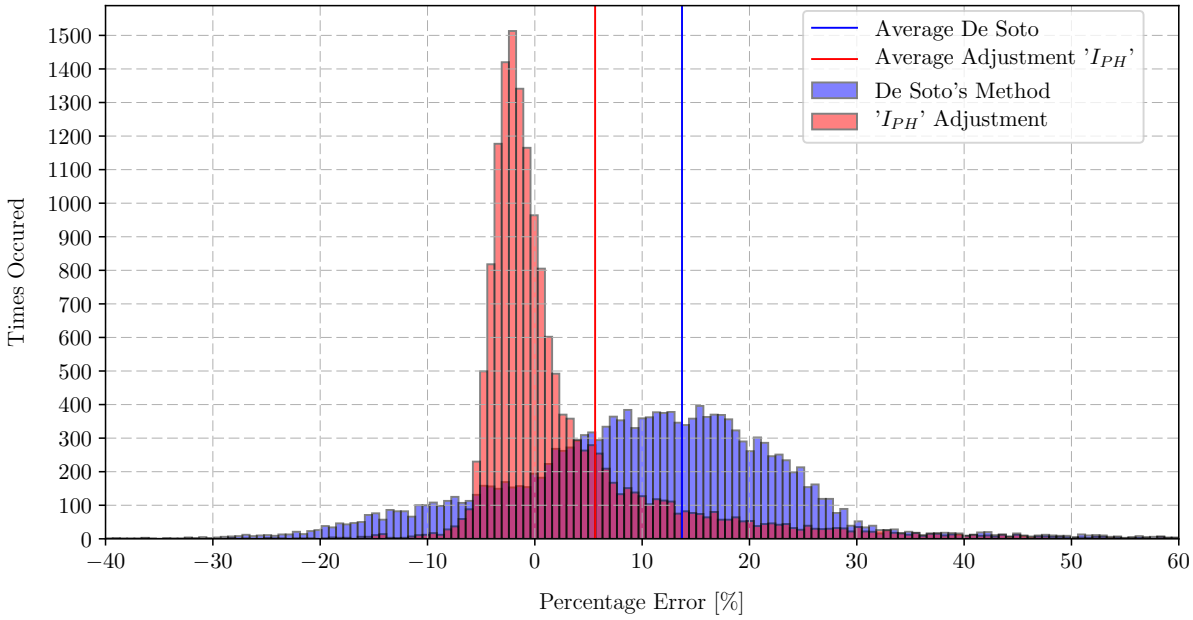

Figure 3.32: Histogram of the percentage error De Soto makes to the actual power compared to the new parameter relationship

3.8.5 Diode Saturation Current

With visual inspection of the output current parameter, it looks like a good representation of the actual parameter data. The average error made compared to the actual parameter is calculated as 11.32%. The parameter seems to be close enough to the actual data and thus the equation presented by De Soto will be used further in this study. Figure 3.33 and 3.34 show the relationship of the output current parameter against varying temperature and irradiance, for both the actual and De Soto's parameter.

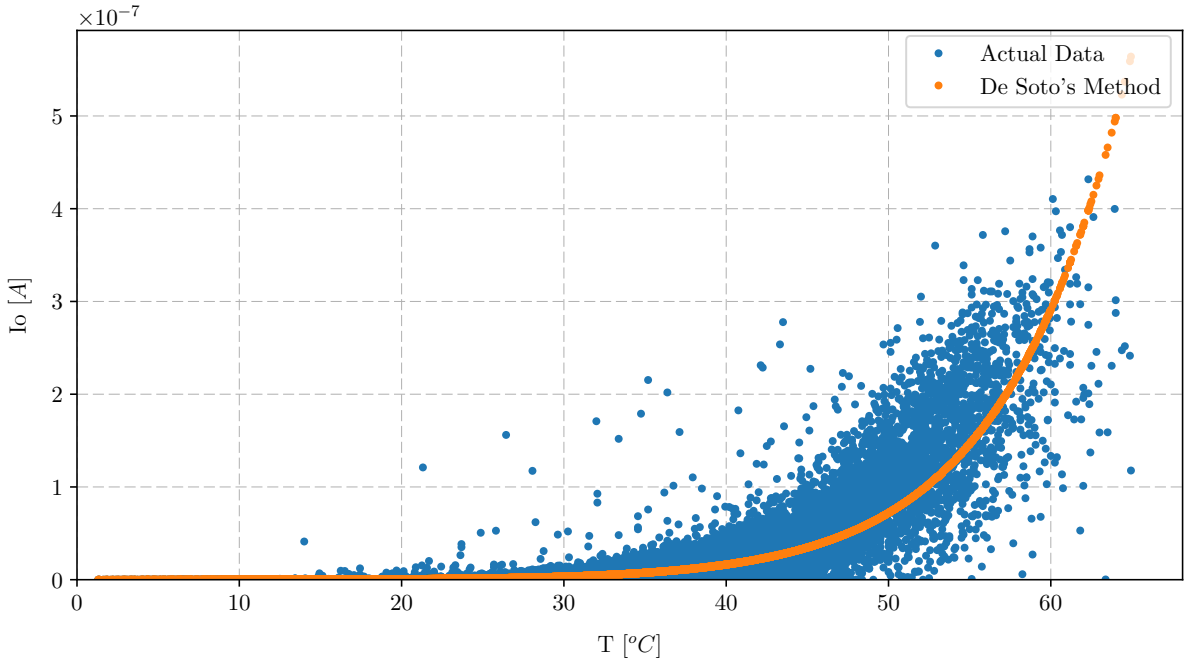

Figure 3.33: The relationship between the actual output current and De Soto's method evaluated with varying temperature

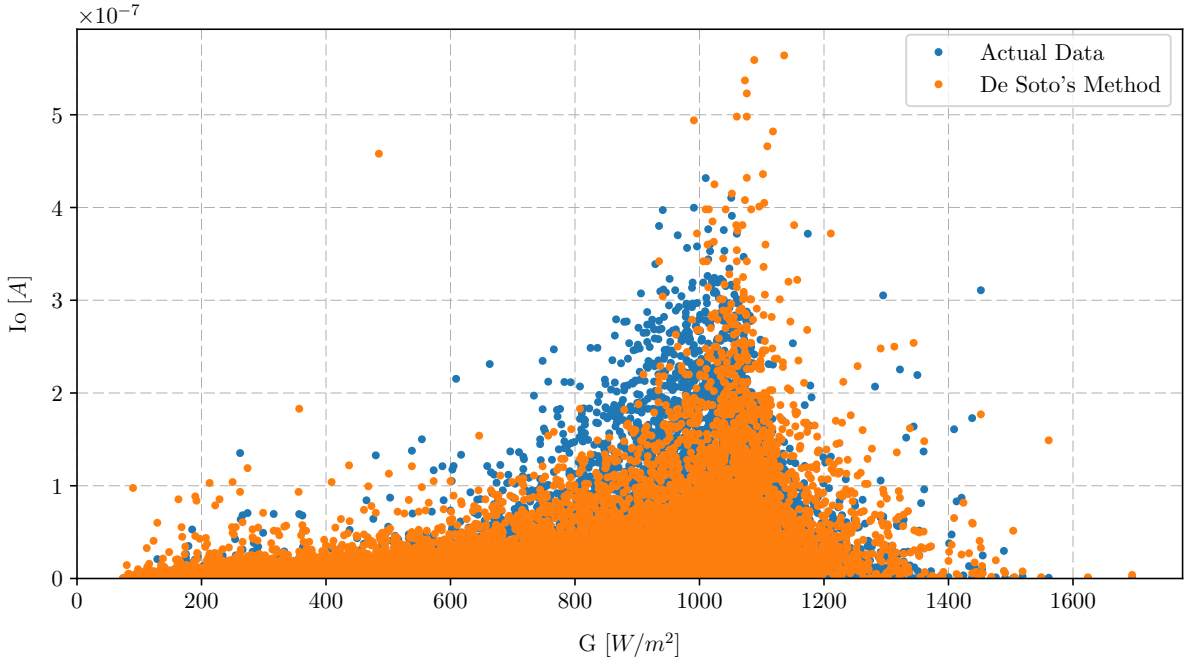

Figure 3.34: The relationship between the actual output current and De Soto's method evaluated with varying irradiance

3.8.6 Ideality Factor

The ideality factor is a complex parameter to define, because it is dependant of many factors. The data are scattered and the relationship is uneven. De Soto's method has a

good representation of this parameter. Figure 3.35 and 3.36 show the relationship of the ideality factor parameter against varying temperature and irradiance, for both the actual and new estimated parameter. The percentage error is 7.929%.

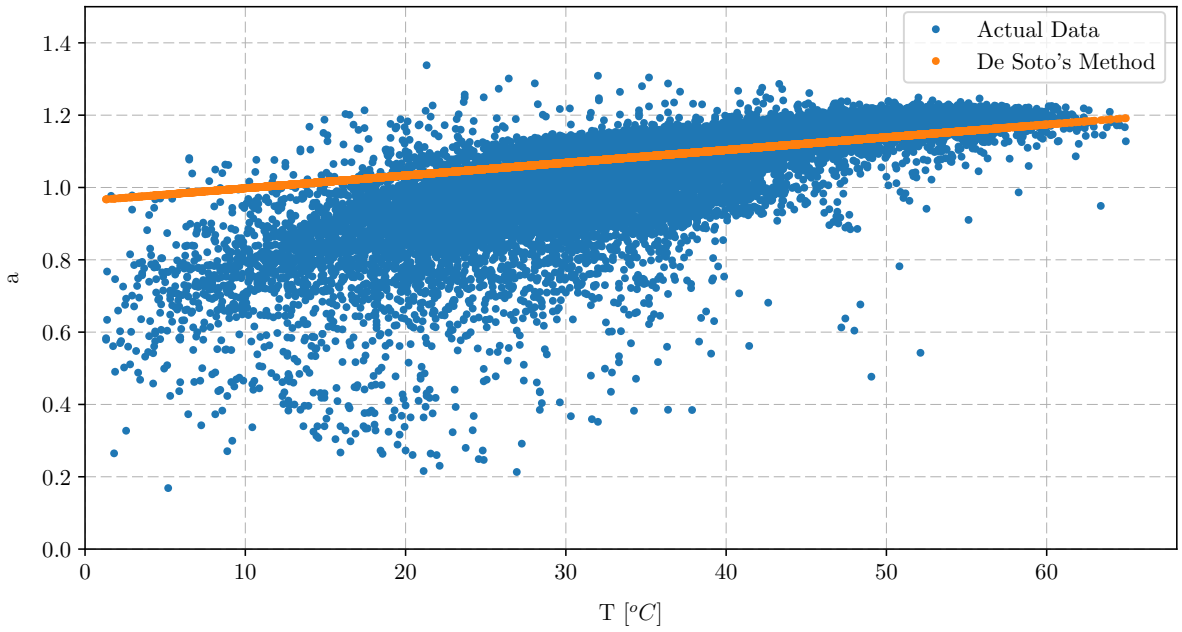

Figure 3.35: The relationship between the actual ideality factor and De Soto's method evaluated with varying temperature

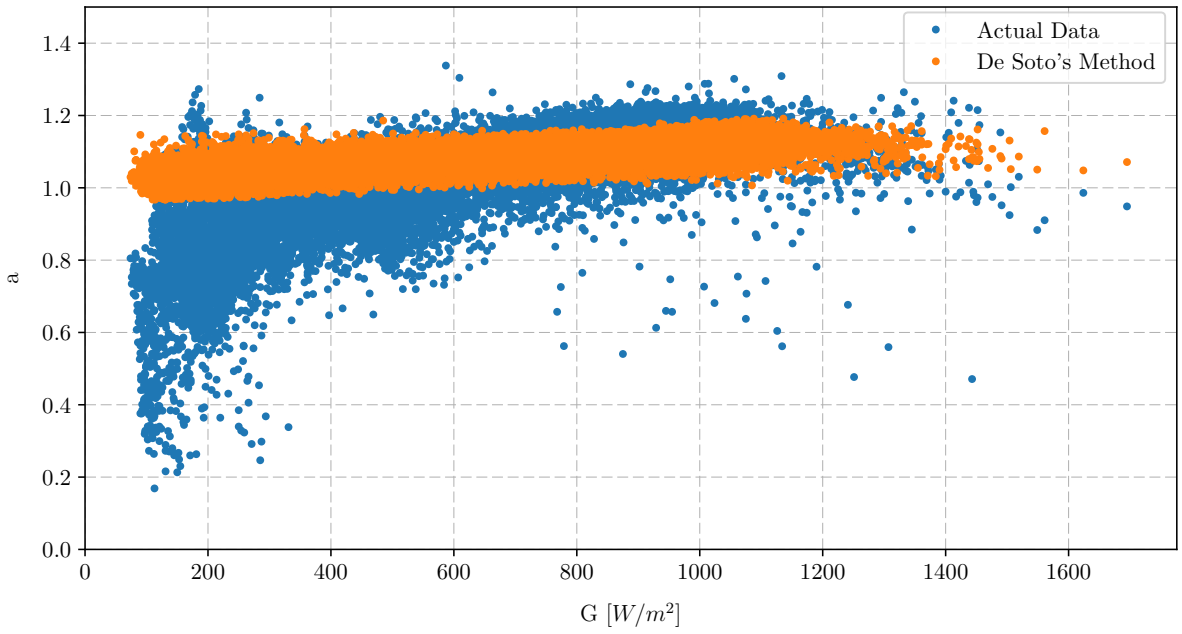

Figure 3.36: The relationship between the actual ideality factor and De Soto's method evaluated with varying irradiance

A linear fitting to the data in the temperature axis, was done and a line with a gradient was defined. The relationship between the new equation and the actual data is shown in Figure 3.37 for the variation in temperature and Figure 3.38 for the variation in irradiance. The new relationship improves the error percentage to only 1.682%.

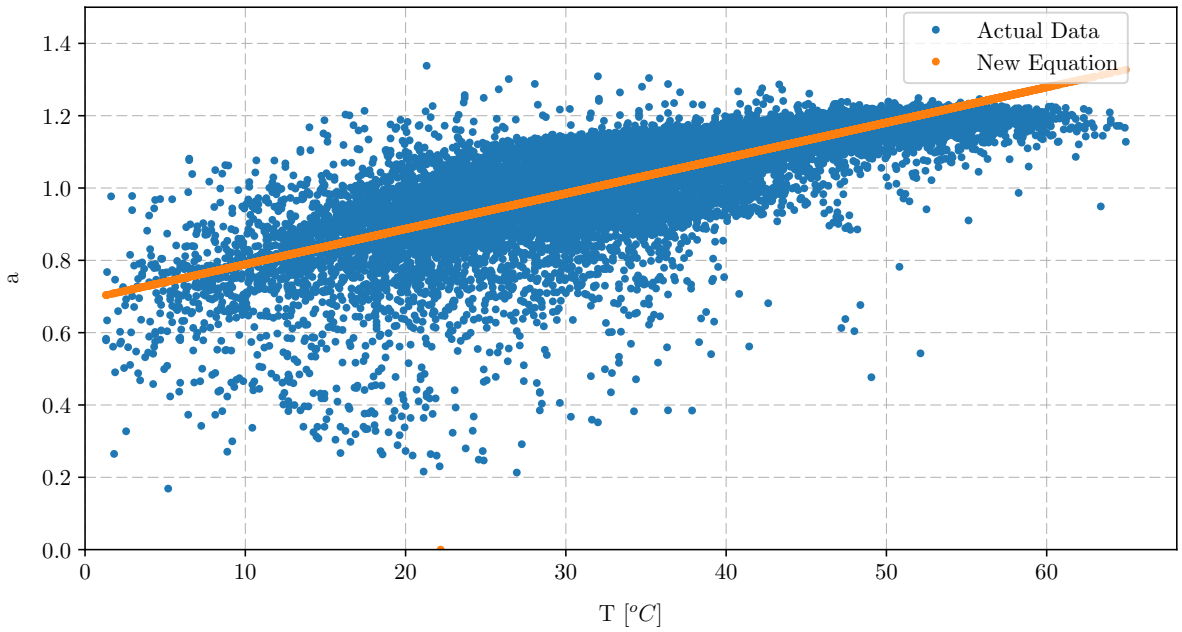

Figure 3.37: The relationship between the actual ideality factor and the improvement on De Soto's method evaluated with varying temperature

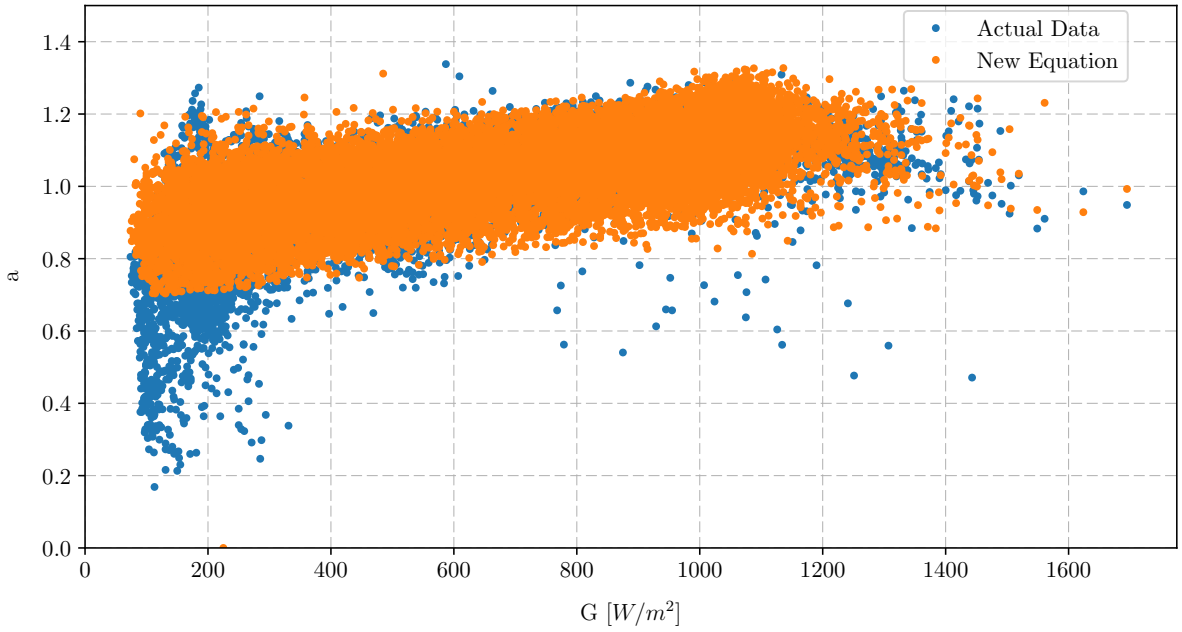

Figure 3.38: The new relationship between the actual ideality factor and the improvement on De Soto's method evaluated with varying irradiance

The influence that this new relationship has on the output power, is shown in the histogram in Figure 3.39. The accuracy of the percentage error increased from 13.714% to 8.672%. The distribution is widened, but the average is closer to zero with an improvement of 5.042 %.

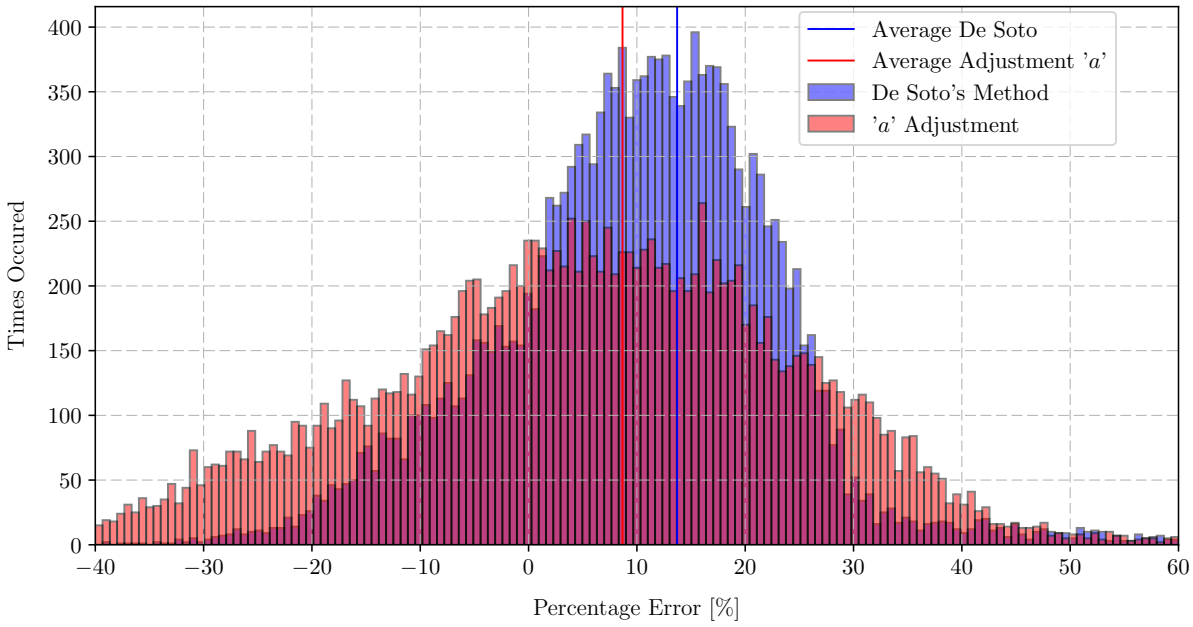

Figure 3.39: Histogram of the percentage error De Soto makes to the actual power compared evaluated with the new ideality factor parameter relationship

3.8.7 New Parameter Equation Set

As is evident in the analysis above, the results of De Soto's extraction method vary from the actual measured data. The equations that are used for these parameters are shown and discussed.

The shunt resistance, R_{SH}, can be used as a constant value from the extraction at STC. The shunt resistance is as shown in equation 3.31.

$$R_{SH} = R_{SH,ref} \tag{3.31}$$

The diode saturation current, I_o, of De Soto is a well fitted representation of the actual parameter, thus it will be kept as the describing equation. The diode saturation current is shown in equation 3.32.

$$I_o = I_{o,ref}\left[\frac{T_c}{T_{c,ref}}\right]^3 e^{\frac{\epsilon N_s}{a_{ref}}\left(1-\frac{T_{c,ref}}{T_c}\right)} \tag{3.32}$$

The ideality factor, a, is fitted with a trend line to improve on the attempt of De Soto's method. The ideality factor is calculated as shown in equation 3.33.

$$a = 0.0098T_c + 0.691 \tag{3.33}$$

The series resistance, R_S of De Soto's method is not the correct representation of the actual parameter. Thus the equation is used with limits, to try and correct the fault in extraction of this parameter. The series resistance is as shown in equation 3.34.

$$R_S = R_{S,ref}\left(\frac{G_{T,ref}}{2G_T}\right) \tag{3.34}$$

$$R_S < R_{S,ref} : R_S = R_{S,ref}$$

The biggest improvement was made at the photo current, I_{PH}. The initial result of De Soto's method overestimated the photo current, but with an irradiance factor removed from the recommended equation, the parameter accuracy improved significantly. This parameter has got the biggest influence on the output power, thus accurate prediction of the photo current is of fundamental importance to the prediction. The photo current equation is as shown in equation 3.35.

$$I_{PH} = \frac{G_T}{G_{T,ref}}\left(I_{PH,ref}\right) \tag{3.35}$$

3.8.8 Total Performance Influence

If the new improved parameter extraction equations are implemented together, the result on the percentage error made with output power produced, is shown in Figure 3.40. The total percentage error is -1.73% of the actual performance of the solar module. This is a good improvement.

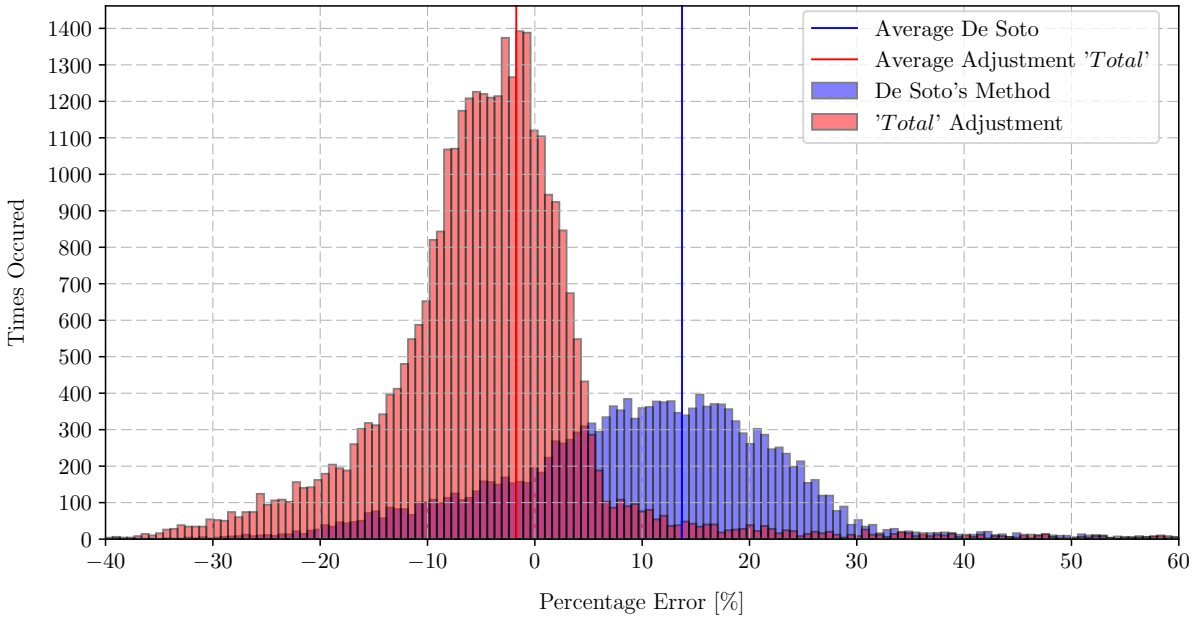

Figure 3.40: Total improvement with the new parameter equations used

From this analysis it is shown that the investigation and improvement to the individual parameters do not necessarily mean an improvement in the output power error made by De Soto's method. The adjustment and optimisation on the power output of De Soto's method is more accurate when the output performance extraction is evaluated.

All the parameters can be improved together if the power output is of importance. If the individual parameters must be extracted accurately and the values of each one is important, the individual equations are of good use.

3.9 Summary

This chapter introduced the hardware used to provide the data that were used in this study. The parameter extraction from the IV-curves measured from the active load is shown. The alternative parameter extraction method of De Soto is introduced and the implementation of the method is discussed. A comparison between the IV-curve from the database and the curve produced by De Soto's method showed an error when the environmental conditions vary from STC. Approximately a year's data is used and an error relationship between the irradiance and temperature is observed. The total error that De Soto's method makes is an overestimation of the MPP of more than 13 %. The error is analysed and an adjustment function, which is later optimised, is developed.

Further investigation into each parameter individually gave interesting results. After analysing each parameter, it was evident that the functions that De Soto presents does not follow the actual parameters very accurately. These parameter equations are adjusted individually to improve the error it makes with the IV-curve extracted parameters. The influence of the new equations that describe the behaviour of each parameter with the temperature and irradiance as reference, is shown. It was evident that the diode saturation current has the main influence on the MPP error.

Chapter 4

Automated Spectrum Data Acquisition and Analysis

4.1 Introduction

The solar spectrum is the radiation emitted by the sun that reaches the earth's surface. The radiation received is referred to as the irradiance and is used by the solar module to produce power. The solar module has a specific band of light to which it responds better compared to other bands and is called the spectral response (SR) of the solar module. The different types of solar modules also respond differently to the solar spectrum. The solar spectrum is of importance when studying PV. The background and quantifying methods are discussed in the first sections of this chapter to provide the necessary insight to the reader.

Later in this chapter, an automated system is designed to measure the spectrum that reaches a solar module. Part of this system is to measure the performance of the solar module at the time the spectrum is measured to see what the influence of the spectrum is on the performance of the output power. The entire system is explained and the design of the automated measuring concept is shown.

After the measurements are taken, the data are analysed to look into the correlations between the performance of the solar module and the spectrum it receives. The measuring period was from 29 May to 27 July 2017. The analysis shows the different colour bands and the amount the bands vary throughout the day. Temperature dependence as well as wind speed at the location are discussed with some interesting observations.

4.1.1 Spectral Response

To measure the spectral response of a solar cell, a controlled and isolated environment is essential. The process consists of illuminating the PV cell being tested with monochromatic beams at different wavelengths. The output of the cell is then recorded to give the response at different wavelengths. The process is equipment intensive and requires laboratory conditions. According to [23], the most widely accepted method to measure the spectral response is the differential spectral responsitivity approach. This approach allows for the introduction of a light bias when measuring. A low power modulated monochromatic light illuminates the solar cell with a more intense broad band steady state beam. This causes a small AC current being superimposed on the large DC current. The su-

perimposed AC current is then measured with a lock in technique to establish spectral responsitivity [23]. A simpler method is presented by [54], in which the cell is irradiated with different broadband spectra to determine the spectral response. The broadband wavelengths are obtained with the use of narrow bandpass polychromatic filters with an approximate bandwidth of 50 nm. The short-circuit current is the essential measurement from the PV cell that is fitted to a chosen spectral response model [54]. It should be noted that some researchers use a normalised spectral response instead of the absolute spectral response to minimise addition loss effects [45].

The generic spectral response of the pi-Si solar module under evaluation is shown in Figure 4.1. The data for the spectral response of a polycrystalline silicon solar module is used as it is given in [45]. The data of the curve for specific data points are needed, thus a polynomial was fitted to give an approximate equation of the spectral response in order to obtain values for the specific wavelengths required. The fitted polynomial is shown in equation 4.1 with an error relation of $R^2 = 0.9963$.

$$SR = 10^{-16}\lambda^6 - 4\times10^{-13}\lambda^5 + 7\times10^{-10}\lambda^4 - 6\times10^{-7}\lambda^3 + 0.0003\lambda^2 - 0.0593\lambda + 4.5572 \quad (4.1)$$

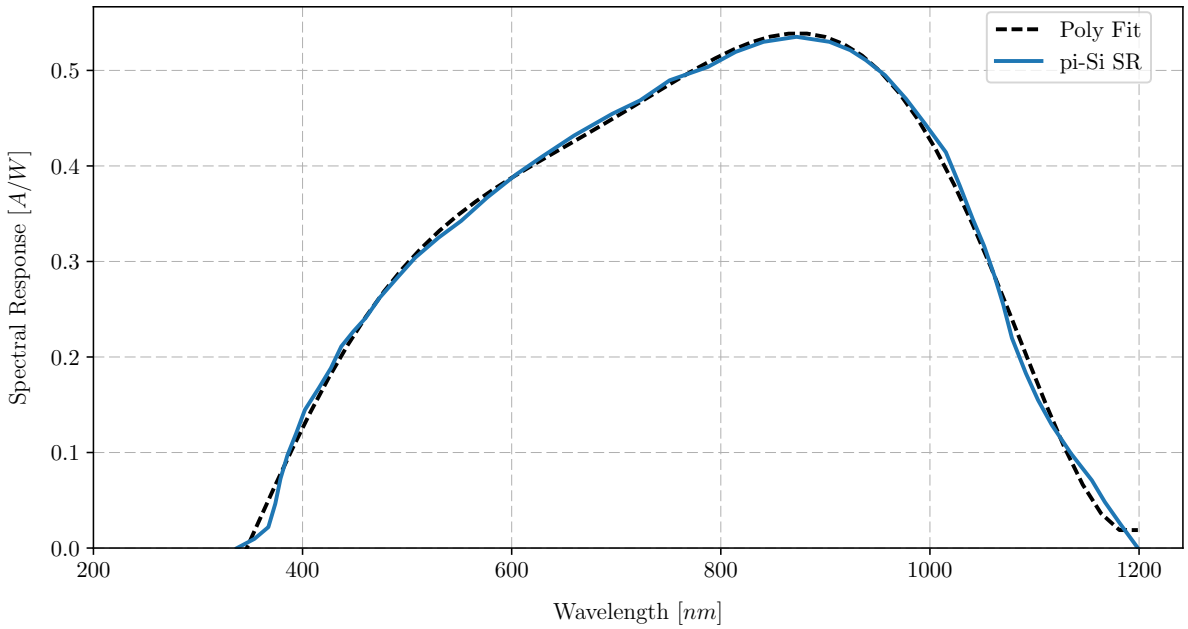

Figure 4.1: Spectral Response of a polycrystalline silicon solar module

4.1.2 Quantum Efficiency

The quantum efficiency of a solar cell is the part of incident photons that are actually converted into electrons by the cell as a function of wavelengths. The relationship is shown by [45] in equation 4.2. It is stated by [11] that the quantum efficiency is zero for wavelengths below 300 nm or greater than 1100 nm. The data derived from the spectral response shows that the QE is still valid at wavelengths above 1100 nm, but it can be a normalised spectral response as it is not stated.

The QE can be derived from the spectral response with equation 4.3. Figure 4.2 shows the data derived from the spectral response's equation.

$$QE = \frac{\text{Number of Electrons Generated}}{\text{Number of Incident Photons}} \tag{4.2}$$

$$QE = \frac{hc}{q\lambda} SR\,, \tag{4.3}$$

where h is Planck's constant, c is the speed of light, q is the electron charge and λ is the wavelength.

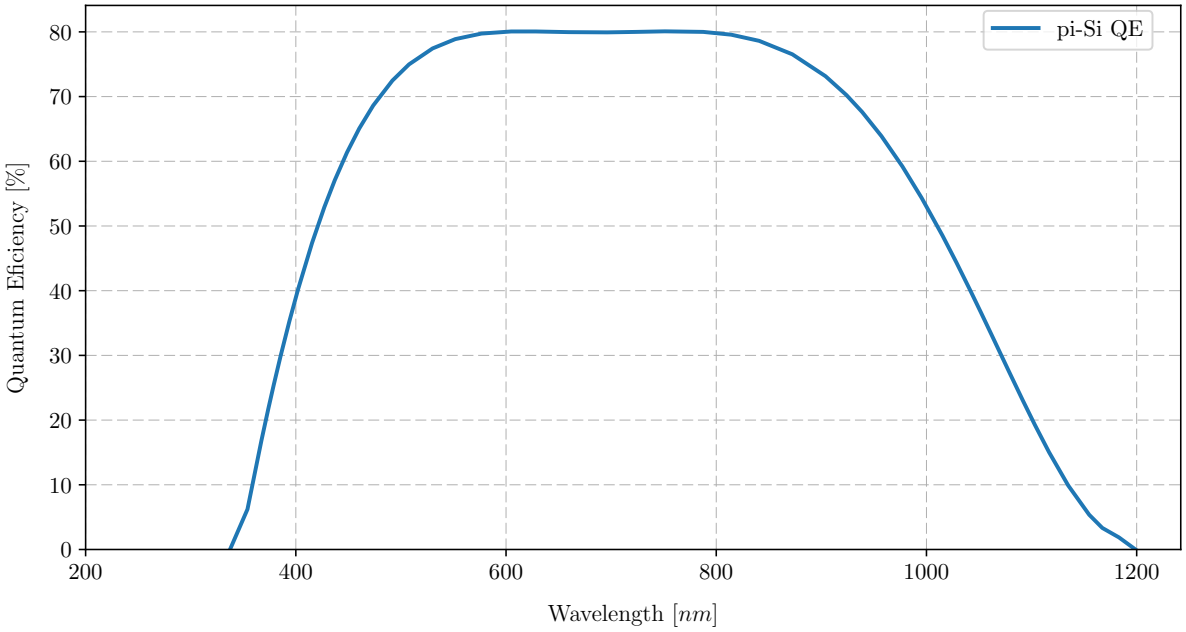

Figure 4.2: Quantum Efficiency calculated from the Spectral Response

4.1.3 Spectral Evaluation

Spectral quality of solar irradiance can be studied and compared to different metrics to quantify the quality of certain characteristics.

4.1.3.1 Average Photon Energy (APE)

The APE is a popular metric in the field of PV analysts and researchers [49]. Equation 4.4 shows the relationship between the spectrum measurement and the para-metrics to calculate the APE.

$$APE = \frac{1}{q}\frac{\int E(\lambda)d\lambda}{\int \Phi(\lambda)d\lambda}\,, \tag{4.4}$$

where q is the electron charge, $E(\lambda)$ is the spectrum measurement in $W/m^2/nm$ that is under investigation and $\Phi(\lambda)$ is the photon flux density defined in equation 4.5. λ refers to the measurements at a certain wavelength and is a dependant variable.

The photon flux density is calculated with the use of the Plank Einstein relation, shown in equation 4.5, and therefore the APE value is independent of the absolute intensity of light at a certain wavelength. The implication of this is that the APE value only indicates the average distribution of light across the entire spectrum [49].

$$\Phi_\lambda = \frac{E(\lambda)}{hc/\lambda}\,, \tag{4.5}$$

where $E(\lambda)$ is the measurement in $W/m^2/nm$ of the spectrum that is under investigation, h is Plank's constant, c is the speed of light and λ is at a specific wavelength in the spectrum.

The APE value is known for its convenient means of modelling PV performance with large sets of spectral data. This means of quantifying spectral data have been used in many previous studies by researchers to examine the performance of PV modules as a function of the solar spectrum [49]. Unlike other evaluation metrics, the APE only describes the spectral composition of solar radiation.

A high APE value indicates that the spectrum is shifted towards a more blue spectrum. A lower APE value correlates to a redder spectrum [17].

4.1.3.2 Useful Fraction (UF)

The second favourable factor to evaluate the spectrum is the useful fraction [17]. Different PV material uses different parts of the spectrum to produce power, thus a ratio is defined to determine what this part is and is known as the useful fraction [33]. The useful fraction can be seen as the part of the spectrum that can contribute in the generation of photo current. Equation 4.6 shows the relationship of the useful fraction.

$$UF = \frac{\int SR(\lambda)E(\lambda)d\lambda}{\int E(\lambda)d\lambda}\,, \tag{4.6}$$

where $SR(\lambda)$ is the spectral response of the solar cell material and $E(\lambda)$ is the spectrum's measurement in $W/m^2/nm$ that is under investigation.

The useful fraction changes its value when the actual distribution of the spectrum changes [33]. A high useful fraction means that the spectral response of the solar module correlates better to the spectrum received by the module, thus a higher MPP is observed. The useful fraction can be seen as the matching of the solar module's reaction to the spectrum.

4.1.3.3 Mismatching Factor (MMF)

The mismatching factor is based on the AM1.5 global spectrum calculating by taking the difference in the relationship between the reference and the measured spectrum with the spectral response of the material type of the solar cell under investigation [30]. The AM1.5 global spectrum consist of the diffused and direct radiation discussed in Chapter 2. The MMF calculation is defined in the IEC standard 60904-7 [45]. This MMF calculation is also referred to by researchers as the spectral factor (SF) with the equation shown in equation 4.7.

$$MMF = \frac{\int SR(\lambda) \cdot E_{AM1.5G}(\lambda)d\lambda}{\int E_{AM1.5G}(\lambda)d\lambda} \frac{\int E(\lambda)d\lambda}{\int SR(\lambda) \cdot E(\lambda)d\lambda}\,, \tag{4.7}$$

where SR is the spectral response of the solar cell material, $E_{AM1.5G}$ is the airmass 1.5 global spectrum measured in $W/m^2/nm$, used as reference and $E_(\lambda)$ is the measurement of the spectrum that is under investigation.

4.1.4 Spectral Conversion Efficiency

The optical to electrical conversion efficiency for a single junction solar cell can be expressed as shown in equation 4.8 [52]. This conversion efficiency is the relationship of the electrical output power to the optical power received of the irradiance illumination on the solar cell. The spectral conversion efficiency is seen by [52] as a useful PV parameter because of the fact that it expresses certain properties of the spectrum that are measured all together. These properties include the absorption of the cell through SR, the bandgap through V_{OC} and the specific circuit properties of the PV cell through the fill factor, FF.

$$\eta = \frac{P_{outputofPV}}{P_{opticalInput}} = \frac{J_{SC} \cdot V_{OC} \cdot FF}{P_{opticalInput}}\,, \tag{4.8}$$

where J_{SC} is the short circuit current density and V_{OC} is the open circuit voltage.

The optical power is obtained by integrating over the measured spectrum shown in equation 4.9.

$$P_{opticalInput} = \int E(\lambda)d\lambda \tag{4.9}$$

The current density is defined as shown in equation 4.10.

$$J_{SC} = \int E_{AM1.5}(\lambda) \cdot SR(\lambda)d\lambda = \frac{q}{hc}\int E_{AM1.5}(\lambda) \cdot QE(\lambda)d\lambda\,, \tag{4.10}$$

where SR is the spectral response of the solar cell material, q is the electron charge, h is Plank's constant, c is the speed of light and QE is the quantum efficiency of the solar cell material.

4.2 Location of the Measuring Set-up

In this section, the existing hardware is shown and discussed. A full shading analysis of the location is done to give the reader better insight into the data and choices made in the analysis of the data later in this chapter. This tests are done on the roof of the third floor of the Electric and Electronic Engineering building at Stellenbosch. The coördinates are 33.9285^o *South* latitude and 18.8668^o *East* longitude.

4.2.1 Facility

A fixed axis solar panel is mounted at an angle of 35^o and is placed facing North. The calculations for this specific angle are the same as in the previous chapter. The solar

module used for this test is a Solairedirect SD Eco Plus 240 W polycrystalline module. The key characteristics are shown in Table 4.1.

Table 4.1: Electrical and influential characteristics of the Solairedirect SD Eco Plus.

Characteristic	Description	Value	Unit
P_{MPP}	Power at the MPP	240 ($\pm$5)	W
V_{OC}	Open Circuit Voltage	37.0	V
I_{SC}	Short Circuit Current	8.66	A
V_{MPP}	Voltage at MPP	30.0	V
I_{MPP}	Current at MPP	8.0	A
$T_{V_{OC}}$	Temperature influence on V_{OC}	-0.37	$\%/^oC$
$T_{I_{SC}}$	Temperature influence on I_{SC}	+0.035	$\%/^oC$
$T_{P_{max}}$	Temperature influence on P_{max}	-0.5	$\%/^oC$

Figure 4.3 shows a photo of the existing test set-up. The solar module on the right is used in this study. This set-up is between two buildings, but is mostly influenced by the building to the left, facing North, that casts a shadow on the set-up before sunset. Figure 4.4 shows the test location, from a satellite photo, with the path that the sun travels at the beginning of July in the middle of the measuring period [2].

Figure 4.3: Photo of the testing facility and set-up

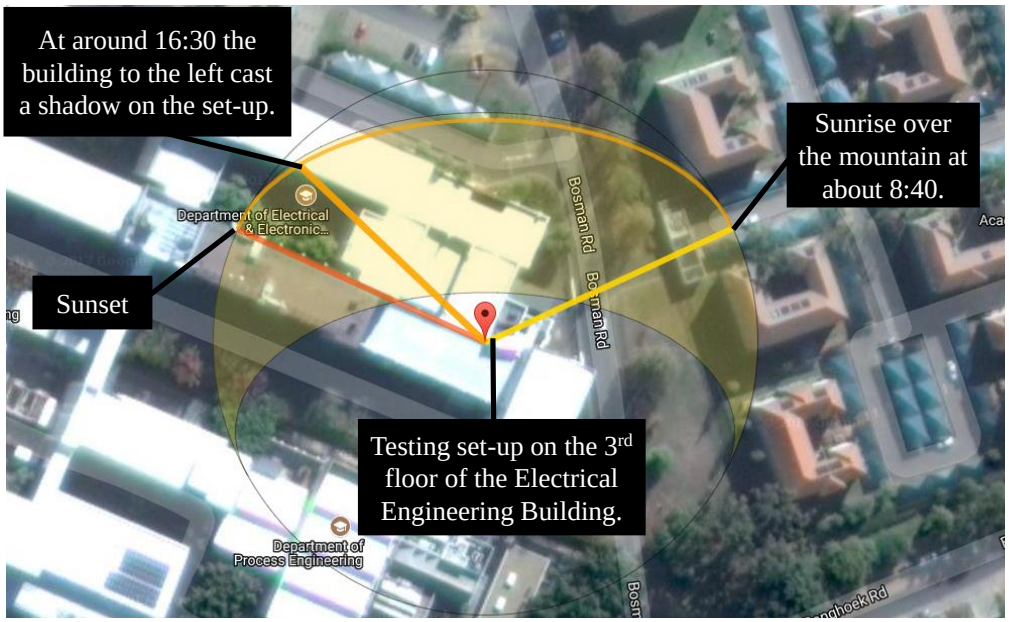

Figure 4.4: A Google Maps satellite photo with the sun's path at the facility at the beginning of July

4.2.2 Shading Analysis

Sun path diagrams are used for the shading analysis of the set-up. The spectral study is shadow sensitive, thus a full shading analysis is important to know how the surroundings affect the measurements of the system [41]. The method followed requires a site survey to determine the angles from the point where the measuring equipment is to the surroundings. It is then used to map out the possible objects that will cast a shadow. The building to the left and the mountain to the right are included in the sun path diagram, shown in Figure 4.5. This helps to build an intuition into where and when a shadow will be cast on the measuring equipment [34].

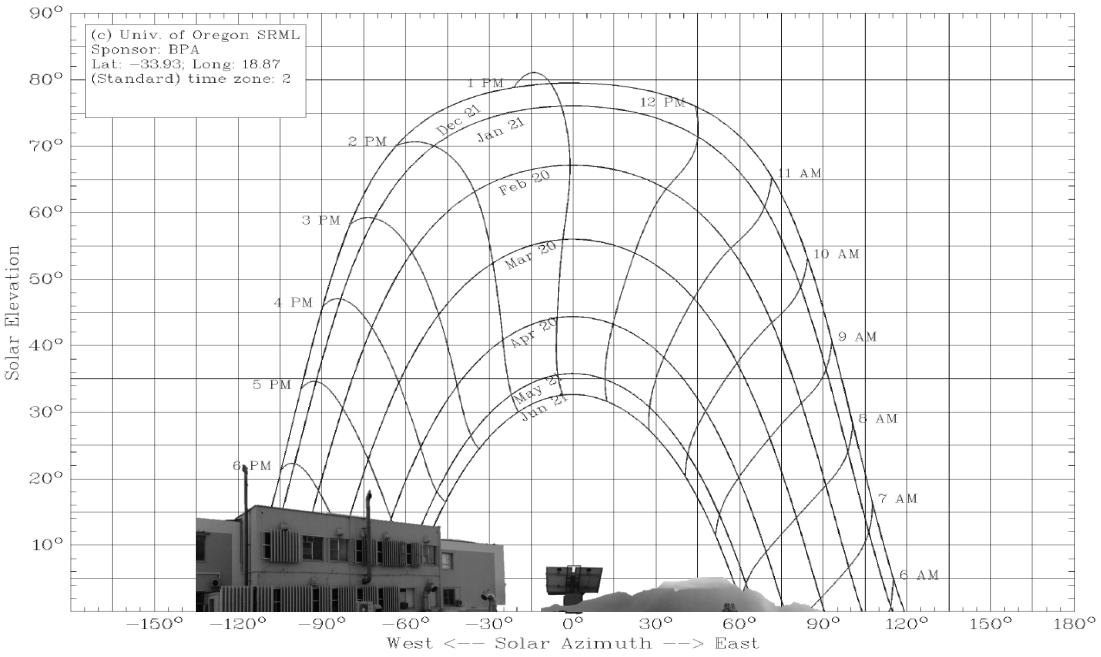

Figure 4.5: Shading analysis of the surroundings of the measuring equipment

4.2.3 Weather

Stellenbosch has a Mediterranean climate, due to the fact that the rainfall occurs in the winter months. It was the rain season when this study was conducted as the study occurred mostly over June and July 2017, thus the weather for these months is summarised below. The data presented are from MyWeather, a commonly used site for weather data [62].

4.2.3.1 June

- The maximum recorded temperature is 31 ^oC, and the minimum is 0 ^oC.
- The average midday temperature is around 19^oC and the average night temperature is 8 ^oC.
- The average daily humidity is 78 %.
- It is expected that one will see rain or a drizzle falling for 14 days in June.
- The average sunshine per day is 7 hours.
- The average daily wind speed is 14 km/h and the maximum, 83 km/h.

4.2.3.2 July

- The maximum recorded temperature is 28 ^oC, and the minimum is -5 ^oC.
- The average midday temperature is around 18^oC and the average night temperature is 7 ^oC.
- The average daily humidity is 77 %.
- It is expected that one will see rain or a drizzle falling for 14 days in July.

- The average sunshine per day is 8 hours.
- The average daily wind speed is 15 km/h and the maximum, 70 km/h.

4.2.4 SAURAN - External Data

Southern African Universities Radiometric Network (SAURAN) has a weather station that is located on the roof of the civil engineering building at 33.2981^o *South* latitude and 18.8654^o *East* longitude and is part of Sonbesie. SAURAN is a network of weather stations in Southern Africa. The station is about 300 m West of the measuring set-up. Weather data such as the wind-speed, ambient temperature and DHI from this database is used. Initially the data from the electrical and electronic Sonbesie [42] weather station was going to be used, which is right next to the set-up, but due to technical problems, the data were not made available.

4.3 Hardware Utilisation and Design

The aim of this design was to build a system that functions automatically. This is due to one day's manual measurements being too time consuming and unproductive and a decision was made to make it automatic. The system's requirements were to measure the IV-curve of the solar module and the solar spectrum in 10 minute intervals. An active load was used to measure the IV-curve of the solar panel and to send the data to a Raspberry Pi. A spectrometer, connected to a Raspberry Pi, was used to measure the spectrum throughout the day. A shutter system was used to protect the spectrometer's receptor. The Raspberry Pi was used to control the system, measure and collect the data and to upload it to a server for analysis. In this section, each hardware component of this automated system is explained and discussed.

4.3.1 Spectrometer

The spectrometer used is a Stellarnet Blue Wave. The specifications of this device are shown in the list below. The use of the software that came with the spectrometer to interact with the device was changed, but is discussed in detail in the software section.

Stellarnet Blue Wave Specifications:

- Measurements in the $200 - 1150\,nm$ wavelength regions.
- 15 standard models with options for customised wavelength ranges.
- Ideal for process, lab, and field applications.
- Signal to noise ratio is 1000 : 1.
- High-speed 16-bit electronics for fast data acquisition.
- 1x3x5 inch enclosure allows for extreme portability.
- Low power consumption through USB.
- Software Development Kit (SDK) is included.

The spectrometer has an optic fibre with a cosine receptor with an opening end equivalent to half a sphere. This receptor is attached to the side of the solar panel and faces

towards the sun. To ensure that the receptor is always at the same place when taking measurements, a bracket is designed to hold it in place. The first concept of the bracket is shown in Figure 4.6. The bracket's screw is fastened at the bottom side of the solar module. A shutter mechanism was designed later on to help protect the receptor from environmental conditions, such as dust and rain.

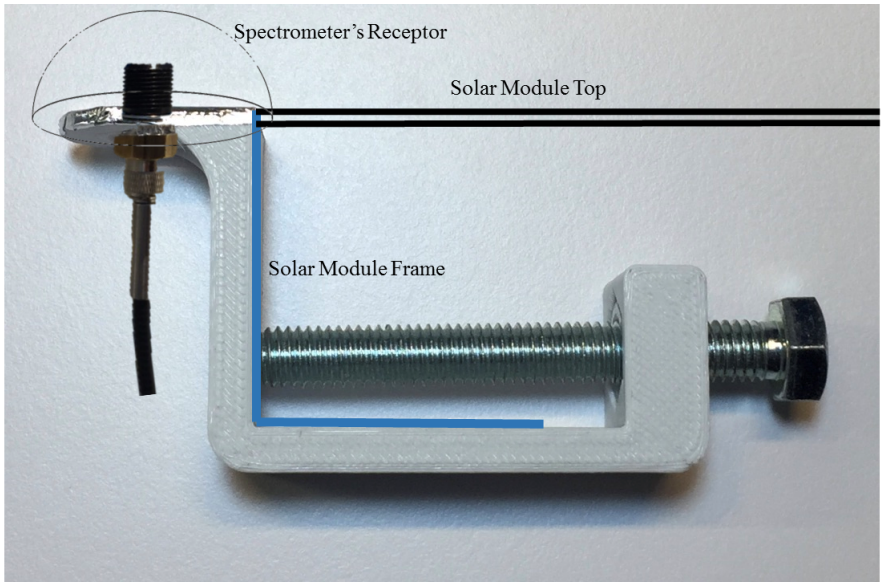

Figure 4.6: First concept of the receptor bracket and how it connects to the solar module

In Figure 4.6, the blue line represents the frame of the solar module and the black lines represents the top of the module. The bracket fits over the frame and the bolt then screws tightly to the frame.

4.3.2 Active Load

The active load that was used is the same as the one that was used in the parameter extraction study. The active load measures and stores data, such as the IV-curve and the back of cell temperature of the solar module. The data are sent to the Raspberry Pi to be uploaded, together with the spectral data, to the database.

4.3.3 Communication Breakout Board - RS485

The active load communicates through RS485 communication, thus a communication board from the Raspberry Pi's UART needed to be built with output pins for the servo motor of the shutter, which is discussed in the next section. A breakout board was designed for the Raspberry Pi. The schematic is shown in Figure 4.7 with the PCB layout in Figure 4.8. The PCB design was done in Altium Designer 13 [36]. A photo of the breakout board with the connections on the Raspberry Pi is shown in Figure 4.8.

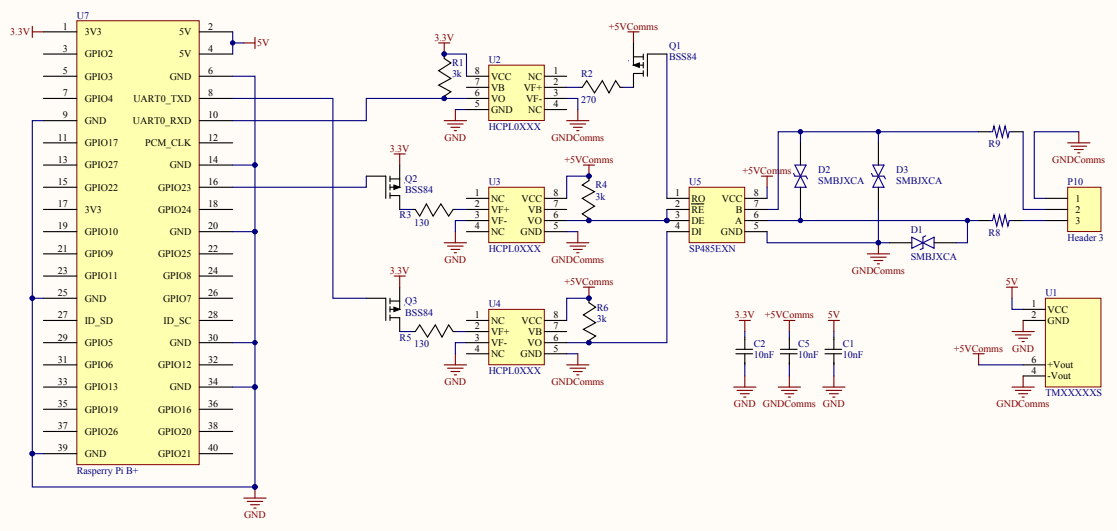

Figure 4.7: Schematic layout of the RS485 breakout board for the Raspberry Pi

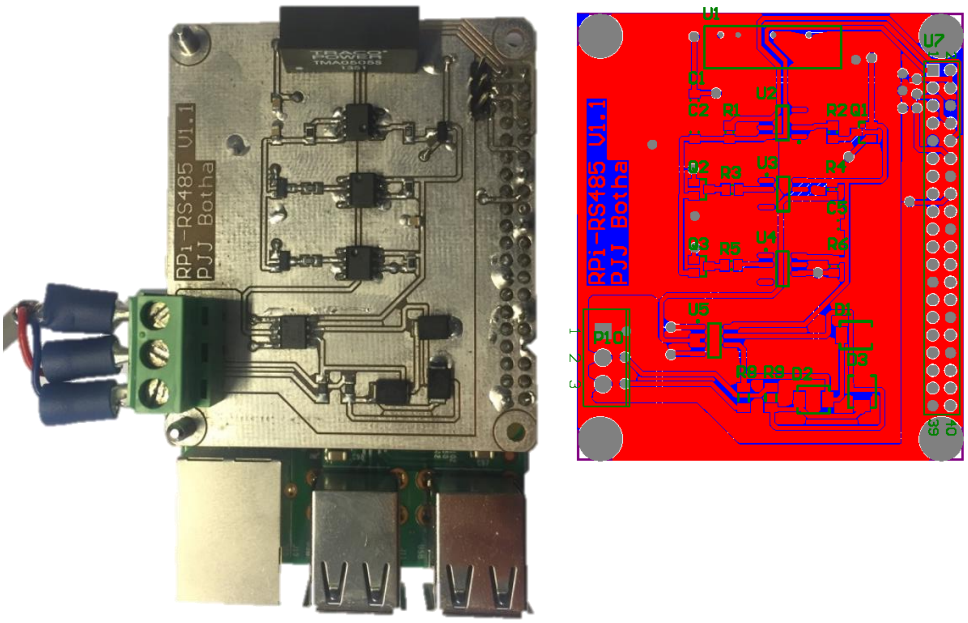

Figure 4.8: Photo of the breakout board on the Raspberry Pi and the PCB layout

The components used for the breakout board and it's corresponding prices, at RS Components [1] on 12th July 2017, are listed in Table 4.2.

Table 4.2: Components used in the RS485 breakout board

Component	Quantity	Cost
Fairchild HCPL0501 DC Input Phototransistor	3	R 86.54
EXAR SP485ECN-L RS485	1	R 9.39
Fairchild SMBJ12CA-E3/52 TVS Diode	3	R 6.62
Infineon BSS84P MOSFET	3	R 2.49
TracoPower DC-DC Converter Isolator	1	R 56.06
Total		R 161.09

4.3.4 Shutter

For the system to be automated, the spectrometer's receptor must be protected when the spectrum is not being measured. This is most of the day and the whole night. A shutter concept is used to open the receptor for each measurement and close it afterwards. The shutter then serves as a form of protection against the weather conditions on the receptor which is located outside. The shutter part will be connected to the bracket to secure the receptor to the solar module.

4.3.4.1 Concept Selection

A solenoid was used in the first design of a shutter system for the spectrometer's receptor. The prototype worked, but a solenoid requires a high current source, thus it was an ineffective solution. The solenoid could work, because a power source is within reach, but then a driver circuit with a relay is needed, which unnecessarily complicates the design. Figure 4.9 shows the first concept of the shutter.

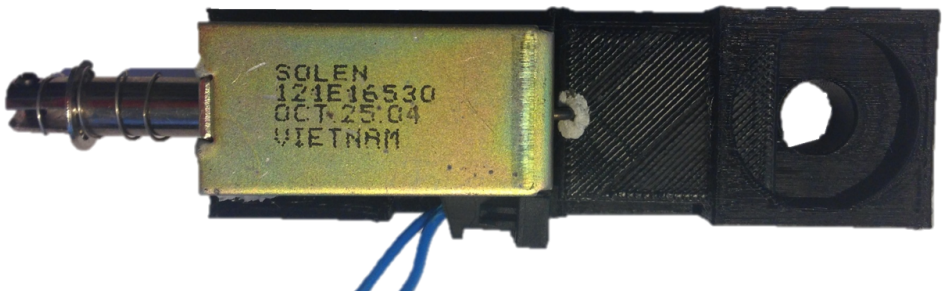

Figure 4.9: Solenoid shutter concept without fixing bracket

The solution for the problem was a servo with a gear pushing the shutter open and close. A CYS model S0009 analog servo [19] was chosen as it is widely available and is sufficient to open and close the small shutter. The specifications of the servo are shown in Table 4.3. The servo can be powered from a GPIO pin on the Raspberry Pi's breakout board. The servo within the newly designed bracket to hold the shutter mechanism is shown in Figure 4.10.

Table 4.3: CYS S0009 Analog Servo Specifications

Size	22.3 x 11.8 x 26.3 mm
Weight	9 g
Speed	0.10 seconds per 60^o
Torque	1.5 kg cm
Voltage	4.8 - 6.0 V

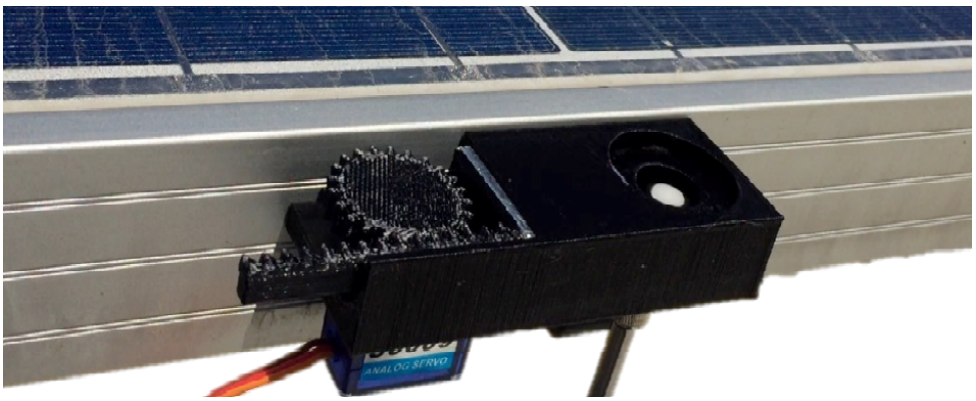

Figure 4.10: Servo shutter concept attached to the solar module

4.3.4.2 Design

The designs were done in Autodesk Inventor Professional 2016 [27]. The servo concept consists of three parts namely: the main bracket that has the screw to fix the mechanism onto the solar module, the shutter lid and the gear that is connected to the servo. The drawings of the whole design of the shutter's three parts can be found in Appendix A.

4.3.4.3 Manufacturing

To be able to test the prototype, the parts were 3D printed. The 3D printer used to print the parts is a Makerbot Replicator 2. Black, 1.75 mm ABS plastic was used because the spectrometer is very sensitive to reflections, thus the darker the colours the better. One of the concerns was that the black plastic would attract light and that the heat would cause the plastic to disintegrate, but after more than two months in the sun, the parts were all in their original form and colour. This was a good result of the abilities of the technology of 3D printing. Ideally the parts can be machined out of a block of aluminium, but for the purpose of this study, the 3D printed parts were more than sufficient.

4.3.5 Data Server

The Raspberry Pi must send the measured data to a server that stores the data. The data take about 100 MB per month and the need for remote data logging to a secure server was necessary. An old quad core desktop computer was used for the server. The problem most servers have is failing hard-drives because of the constant writing and reading of the data on them. Due to the fact that the data of this system are so important, a RAID

set-up was chosen. The RAID1 chosen for the server essentially consist of hard-drives in parallel. A figurative explanation is shown in Figure 4.11. The hard-drives are essentially a clone of one-another and can run off of any one of the drives, because the boot loader is also on all of the hard-drives. More about the software set-up of the RAID1 is explained in the software section.

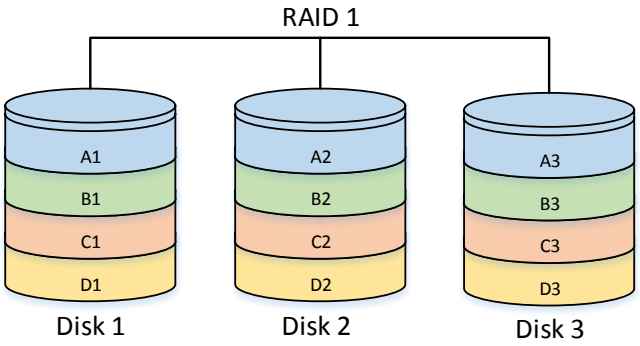

Figure 4.11: Raid Set-up diagram

4.3.6 Raspberry Pi (RPi)

A Raspberry Pi 2B is used to integrate all of the measuring devices. The spectrometer connects to the RPi through USB. The active load connects to the UART of the RPi through the RS485 breakout board. The servo shutter is controlled through GPIO pins that are brought over to the breakout board and lastly, the USB wifi dongle connects the RPi to the internet. The internet is provided for by an access point from a nearby building.

4.3.6.1 Servo Control

The servo needs a Pulse Width Modulation (PWM) signal on the control pin in order to turn. The Raspberry Pi has a hardware PWM on GPIO pin 18. The other general output pins can be used to produce a software PWM. The software PWM is dependent on the clock, and thus not as stable as the hardware PWM. This will cause the servo to be unstable in the opening and closing movements. This factor needs to be taken into account when designing a sensitive system that is dependant on the functionality of the PWM.

4.3.7 System Integration

The whole automated system with all of the components used is shown in Figure 4.12.

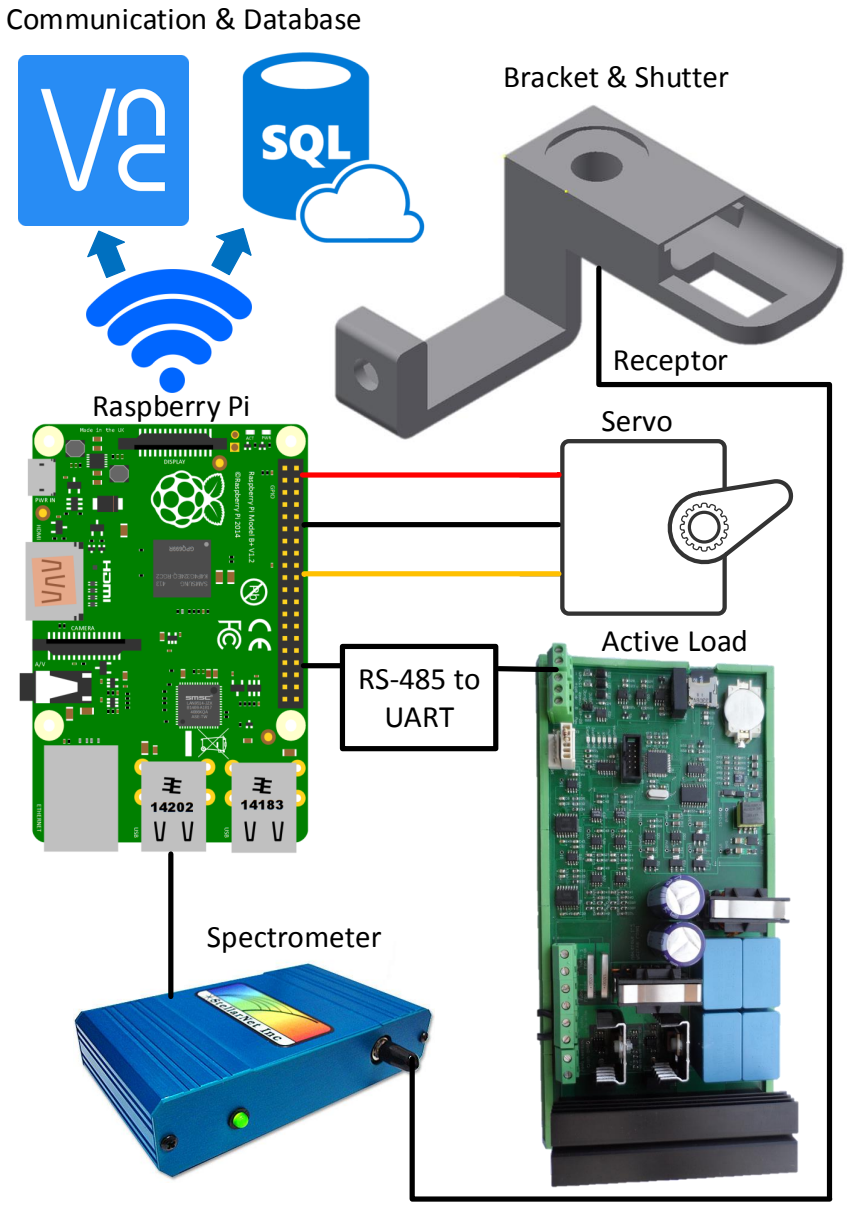

Figure 4.12: System Set-up

4.4 Software

In this section, the different parts of the system's software that were developed are discussed and explained. The spectrometer and servo's software are uploaded to the Raspberry Pi. The software on the Raspberry Pi controls all the peripherals of the system and connects the system to the internet. A GUI program, that can be called on any computer, can be executed to fetch data from the database on the server to show the spectrum visually in raw data format as counts or irradiance.

4.4.1 Controlling Software

The spectrometer has software called SpectraWiz for the Windows OS environment. This was used for initial testing and used to learn how the spectrometer works and responds.

The automated measuring system needs to run from a Raspberry Pi, thus a normal .exe program cannot be used. The manufacturers provided source code to measure the spectrum through Python. However, this code is not well written and some privileges such as locked files, make it difficult to work with. The solution to this was to call the measuring function through a command line command with the use of Python. Because all of these aspects of the system need to happen on their own and independently, the file is called from another Python script that controls the shutter system. This Python script is used as the main controlling program, which calls all the independent software scripts.

A flow diagram of the implementation of the controlling script is shown in Figure 4.13. The function starts by initialising the GPIO settings. A check is done to see if the servo is open and if it is then it closes the servo. If it is closed, then the function checks if it is time to measure. If it is time to measure, then the servo is opened and the measuring function is called. After the measurement, the servo is closed. It it is not time to measure the process must sleep for 0.95 seconds.

The flow diagram for controlling the servo from the GPIO of the Raspberry Pi is shown in Figure 4.14. The function initialises the PWM to control the servo. The desired positions, open or closed, of the servo is set and a 0.3 second time delay is used to give the servo enough time to move to the position. After the position is reached, the PWM is closed and stopped.

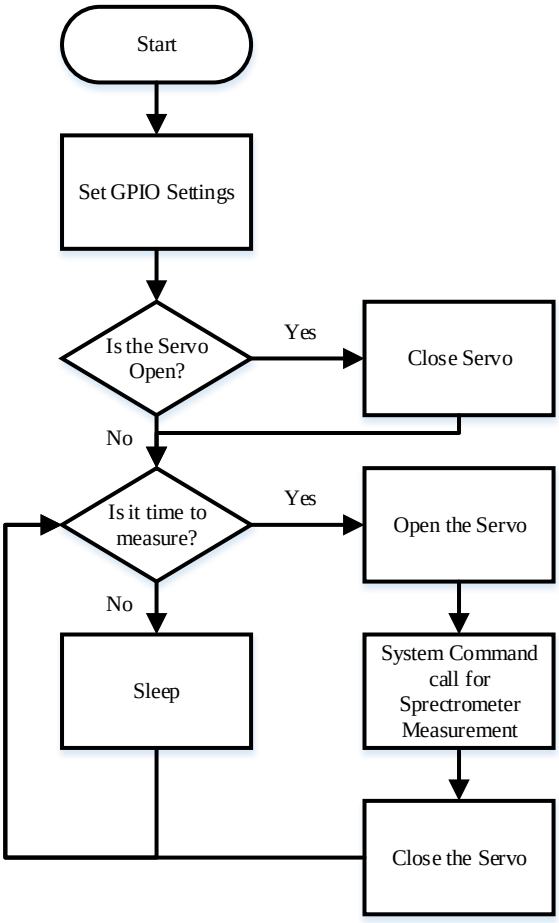

Figure 4.13: Main software Python script flow diagram

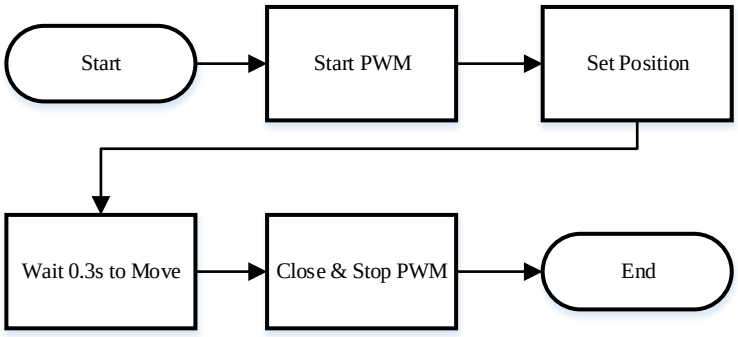

Figure 4.14: Servo controlling software flow diagram

A few things were added and changed in the software file of the spectrometer called "stellernet.py". The changes are explained and discussed in the next section.

4.4.1.1 SQL Query Function

A function called *db_execute* was added. This function holds the database user name, password and table to which the data should be sent. The option to send the data to the localhost or the webhost is available in this function. The different login parameters for the database is shown in Table 4.4. A flow diagram of the "*db_execute*" function is described in Figure 4.15.

Table 4.4: Login parameters for the database

Parameter	Web DB	Local DB
Address	www.pvsoiling.co.za	10.10.11.78
User Name	xpiosbkm_JP	JP
Password	*Maties123*	PVLAB
Table	xpiosbkm_Spectrum	JP_TEST

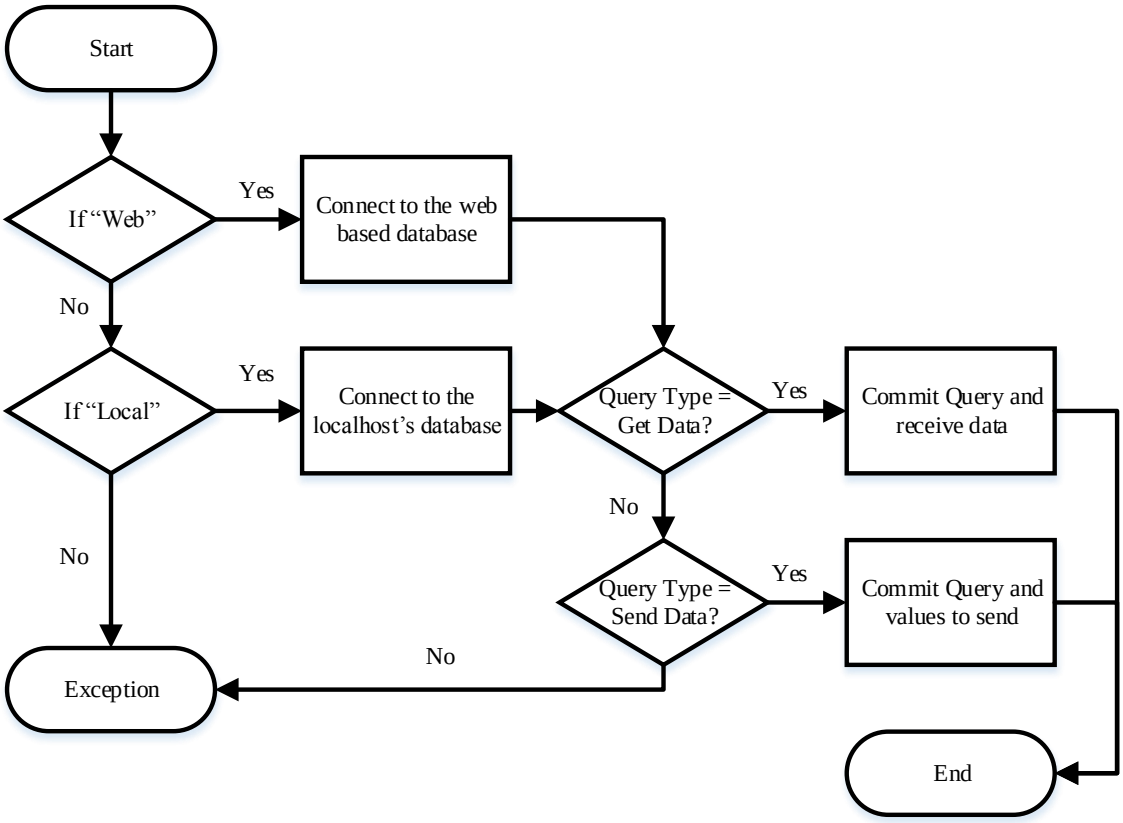

Figure 4.15: "*db_execute*" function software flow diagram

4.4.1.2 Spectrum Measurement

The integration time of the spectrometer refers to the time that the spectrometer opens the receptor to record the light. If the integration time is too long, the light measured becomes saturated at certain wavelengths and thus the data cannot be used. This is not a problem when using Windows OS as SpectraWiz warns of possible saturation and then one can change the integration time. With the automated system, the integration time cannot be changed for every measurement. In order to keep the data measurements constant, a fixed integration time was chosen. With some measurement experience, it was established that $20\,ms$ would be short enough to prevent the spectrometer's measurement from saturating but also long enough to record enough light from the receptor. The integration time is changed from $100\,ms$ to $20\,ms$ to account for possible saturation of the measured data. This is changed in "*_init_config*", from the source code the suppliers provided. In Figure 4.16, saturation of a measurement is shown against the AM1.5 global spectrum. It is evident that the centre part of the spectrometer's measurement is saturated.

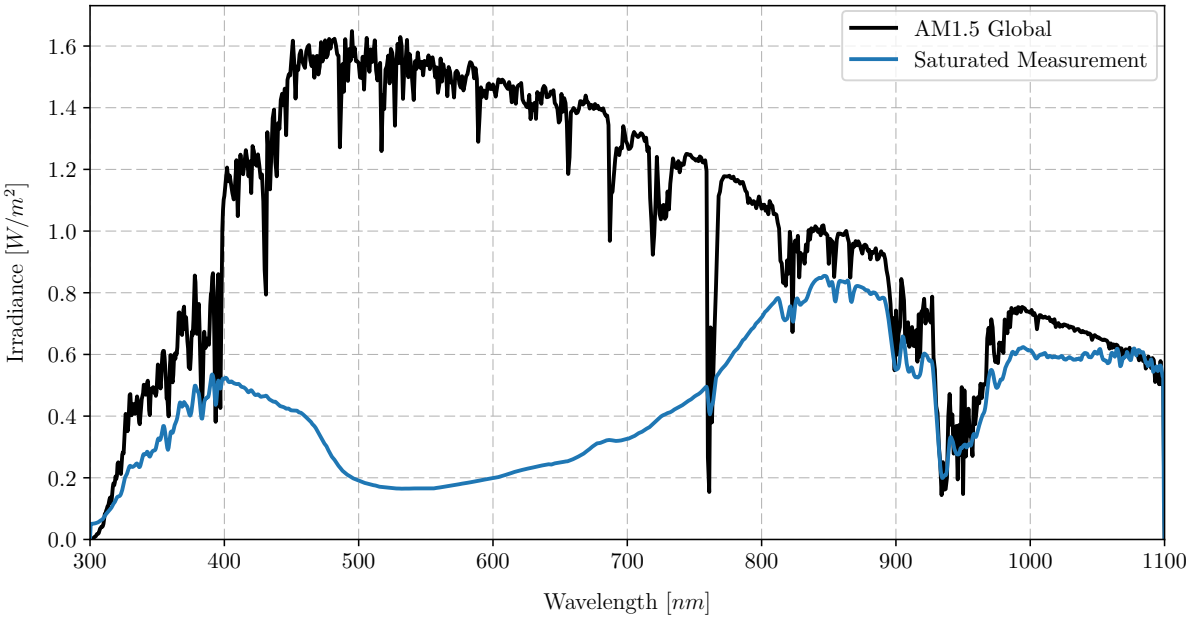

Figure 4.16: Saturated spectrum measurement against AM1.5 global

4.4.1.3 Additional Software Changes

A function that saves the data to an on-board text file is written and executed after the measurement is done. This was done to keep the data that were measured when the internet connection is down. The time stamp that the spectrometer includes in the data are in the Epoch format. This was extracted and converted before it was sent to the database to provide a readable time stamp.

4.4.2 Graphical User Interface

The software that comes with the spectrometer is only compatible with Windows OS and does not allow you to plot historical data. The data that are uploaded to the database must be visually seen, especially at the beginning of this project to ensure correct measurements. Therefore a program was written to give the user of the database's data more insight and value, with the function to query any data measured and display the graph.

The program developed is a Graphical User Interface (GUI) written in Python by the use of the TKinter library. The program allows the user to enter a dataset ID to plot the data. The user can also insert the date and time for which the data are required, and the program will look for the data in the database and plot it if it is available. The program will plot the data requested over each other to allow comparison of different spectrum measurements. The program is also written to look for new entries in the database and it will plot the data as soon as it is available, which gives a real time feeling to the user. The data that are plotted can be cleared by the Clear button. The Quit button closes the program. The integrated irradiance, date and time of the last plotted data are shown at the bottom left corner of the program. Two different versions of the program are developed to show either the raw data measured in counts, or the converted data in irradiance.

A flow diagram of the implementation is shown in Figure 4.17. The GUI software begins

with the draw of the frame, buttons and text as it was shown in Chapter 4. The user has the ability to request a dataset. If a dataset is requested by the ID or the date and time, the GUI looks in the database to see if the data is available and then updates the frame to show that required data. The GUI will update new data automatically if it is written in the database. The user has the ability to clear the frame to compare new spectral data. Screen shots of the two different GUI's are shown in Figure 4.18 and 4.19.

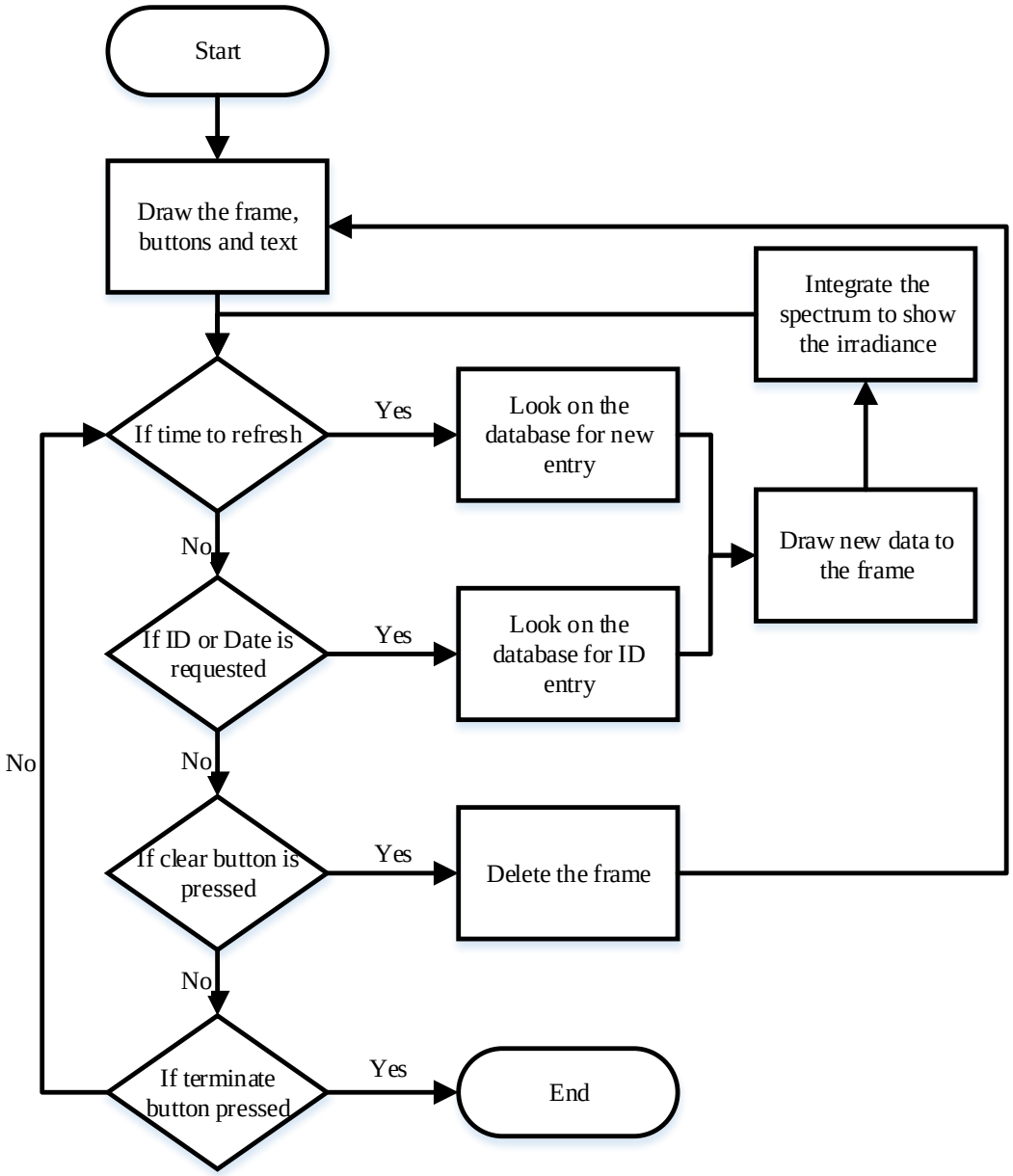

Figure 4.17: Flow diagram of the GUI software

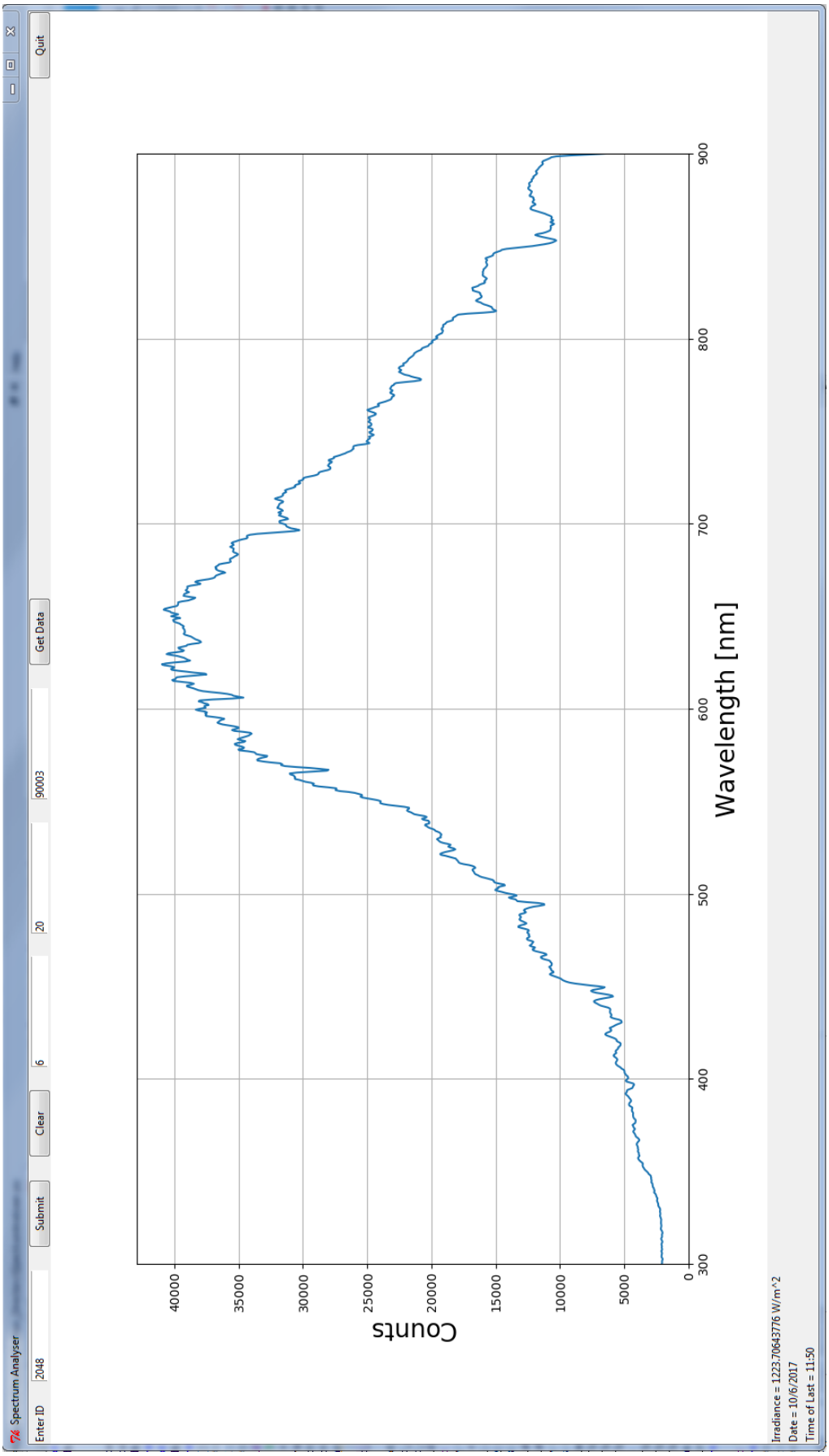

Figure 4.18: Screen-shot of Spectral Counts GUI

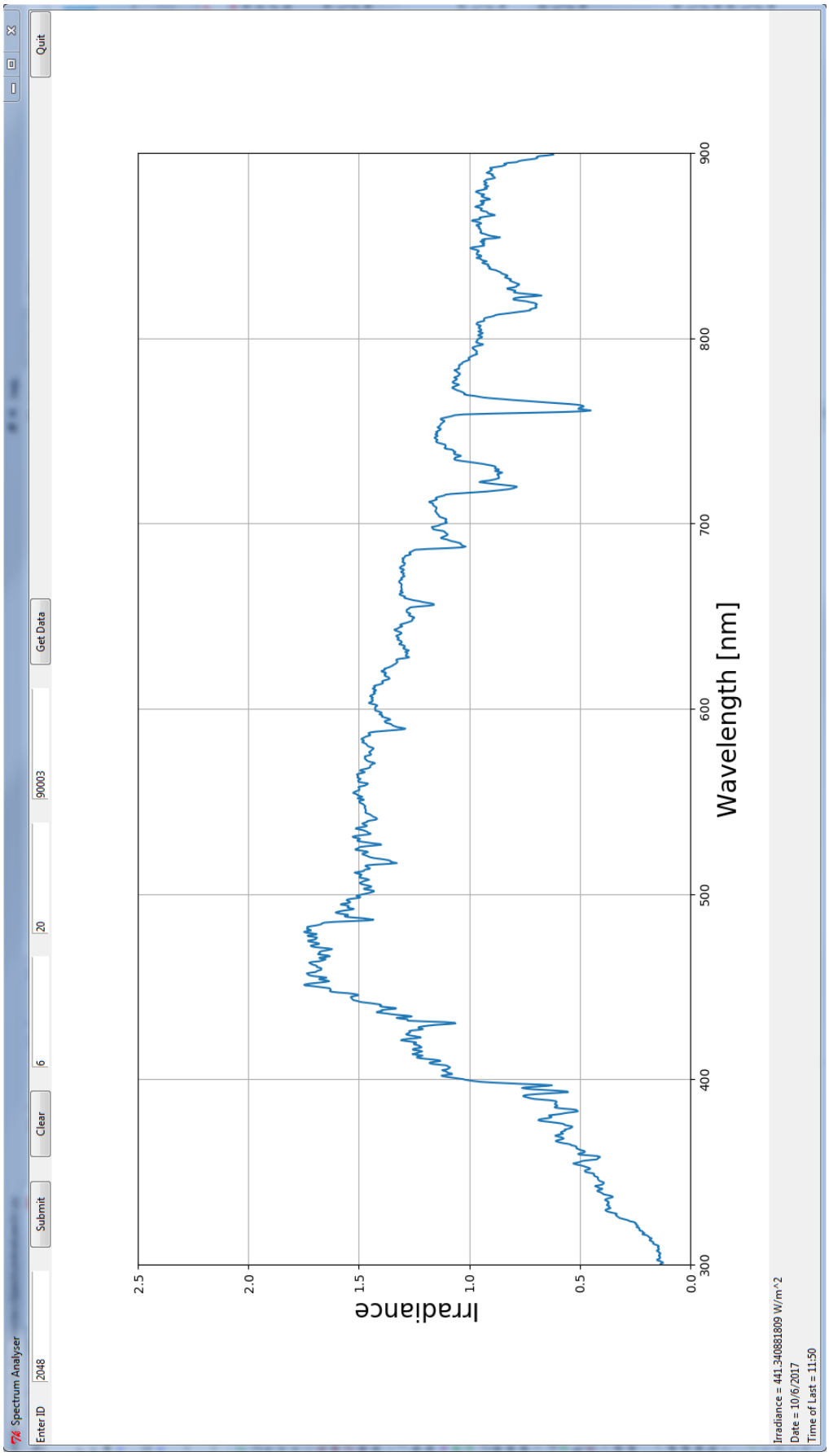

Figure 4.19: Screen-shot of Spectral Irradiance GUI

4.4.3 Database

The database is a mySQL database which is managed by phpmyadmin. The database is locally hosted to keep internet data costs to a minimum. The option to sync the data to an online database is also tested and used as an off-site backup of the measured data. The online database is hosted on www.pvsoiling.co.za. The data are uploaded to the database from the Raspberry Pi with a SQL command every time new data is recorded. A guided process that was followed has been documented and inserted in Appendix B for reference on how the installation of the RAID was done for the local server.

4.4.4 Server

The server computer is running Linux Ubuntu Server. The server has three hard-drives that are configured in RAID1. The configuration of RAID1 was done with the installation of the server OS by using the installation steps to partition all the hard-drives into the required partitions and combining the partitions on the hard-drives to result in a working RAID1. Webmin is used to manage the server with the availability to monitor all the hardware, such as the status of the RAID, and to configure permissions and mySQL tables. This managing software provides a GUI to the server, which makes managing and status reading convenient. Webmin is shown in Figure 4.20, with the specifications of the server shown within the Webmin window.

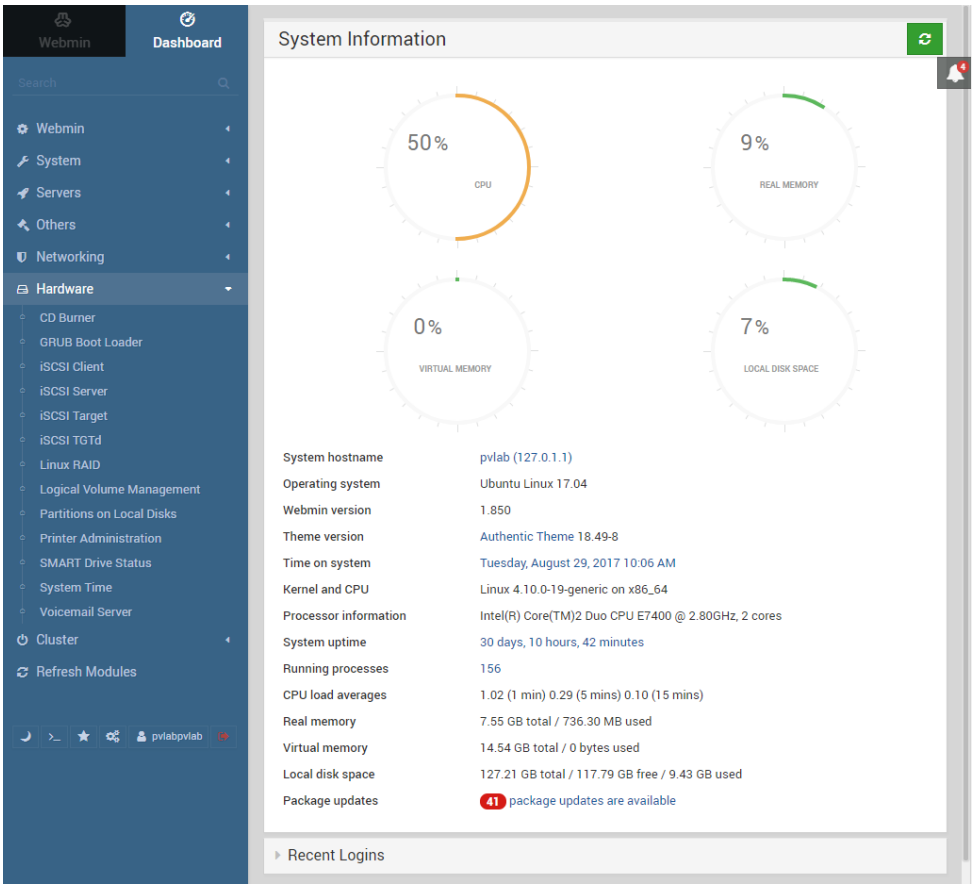

Figure 4.20: Screen-shot of Webmin server management software and specifications

4.5 Data Validation

The measurements must be validated before any further investigation into the data can be done. Thus it is compared to various reference standards to see if the data is valid for this study. In this section, the part of the spectrum that is used is discussed with the conversion of the raw data measurements to the irradiance unit. The limitations and problems found are also discussed.

The usable data that are measured is shown in Table 4.5, where the data that are complete is green and the incomplete data is red. The white blocks are not part of the measuring days. Incomplete data are a result of different problems that are discussed later in this chapter.

Table 4.5: Day's data that are measured and used in the study

May	1	2	3	4	5	6	7	8	9	10	11	12	13	14	15	16
	17	18	19	20	21	22	23	24	25	26	27	28	29	30	31	
June	1	2	3	4	5	6	7	8	9	10	11	12	13	14	15	16
	17	18	19	20	21	22	23	24	25	26	27	28	29	30		
July	1	2	3	4	5	6	7	8	9	10	11	12	13	14	15	16
	17	18	19	20	21	22	23	24	25	26	27	28	29	30	31	
Incomplete					Complete						Not Measured					

4.5.1 Calibration File

The spectrometer's calibration was conducted on 13 July 2016. The calibration file is used with the conversion from counts, which is the raw data measured, to irradiance. In Figure 4.21, the data of the file are shown. When measured the high values in the calibration file, with the sensitivity of the spectrometer in the high and low wavelengths, result in measuring noise after the conversion. Thus, a decision was made that the study will only look at the spectrum from 300 nm to 900 nm. In Figure 4.21, the blue line indicates the part of the spectrum data that are seen as usable in this study. Every observation and conclusion from this point on in the chapter is based on this band of the spectrum.

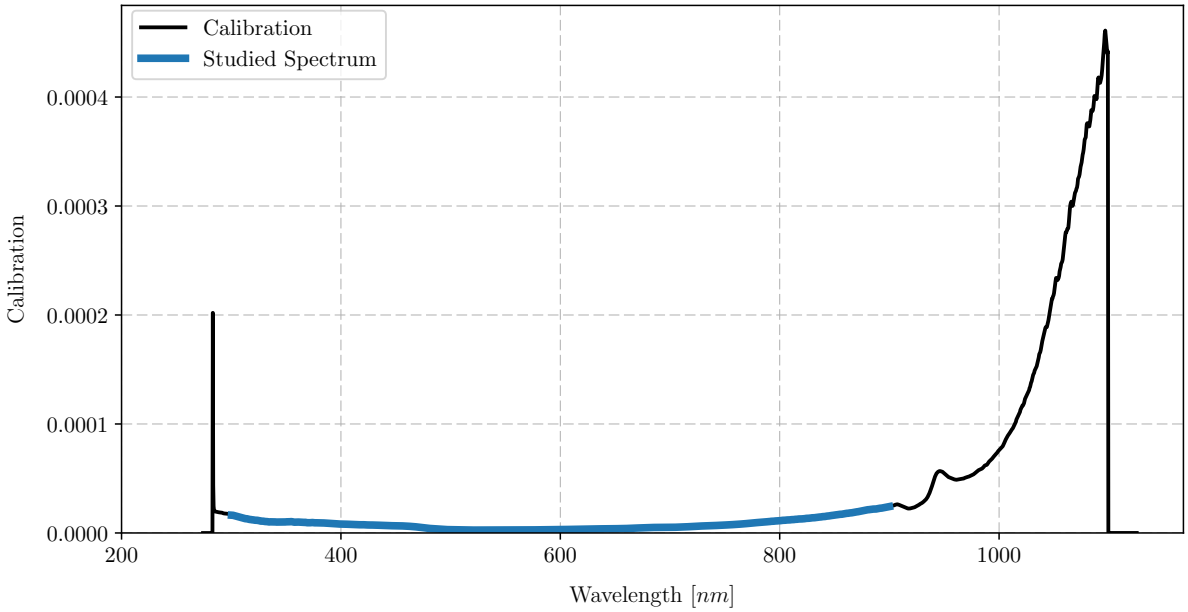

Figure 4.21: Plot of the calibration file of the spectrometer and the band of spectra used in this study

4.5.2 Data Conversion

The software to measure spectrum data in Windows is trivial with an easy GUI to use. The data can either be measured in the radiometric or counts function in Windows. The radiometric function's data are in irradiance, thus no conversion is needed to get data that can be analysed. If the counts function is used, the data measured can be converted into irradiance by the use of equation 4.11. The radiometric function is only part of the Windows SpectraWiz and cannot be used in Linux.

$$G = \frac{Cal_t}{Meas_t}\ Cal_{Value}\ (Counts - DS)\,, \tag{4.11}$$

where G is the irradiance, Cal_t is the integration time used in the calibration measurements, $Meas_t$ is the integration time in which the current measurement is taken, Cal_{Value} is the value of the calibration at the specific wavelength, $Counts$ is the raw data measured at the wavelength and DS is the dark spectrum counts taken as a constant in this study.

For the automated system, the measurements can only be done by the use of the Python code in the Linux environment, thus the conversion needs to be done to get the irradiance at each wavelength measured. The use of the calibration file that comes with the yearly calibration of the spectrometer is vital for the conversion.

The calculation requires a so called dark spectrum measurement to complete the calculation. This is used as a constant between 1500 and 2000 counts, as recommended by the supplier of the spectrometer, if it is not possible to get a black spectrum for each measurement. The value used in this study is 1500.

4.5.3 Measured Data Categorisation

The spectrum is measured from 7:00 to 18:00. This time includes the sunrise and sunset. The location only allows direct irradiance from after 8:00, when the sun rises above the mountain, and at 16:00 a shadow of the adjacent building is thrown on the system. Thus, the decision to split the day's data into diffused irradiance and direct irradiance is made. The times between these categories are seen as transition times with scattering and incorrect measurements expected for the reason that the surrounding buildings influence the measurement. Figure 4.22 shows the categories chosen for the data. A measurement from the first clear day, one in the middle of the measuring period and one at the end of the period are plotted. It is interesting to see that June has the shortest direct irradiance, as it is known. Thus the data are correlating.

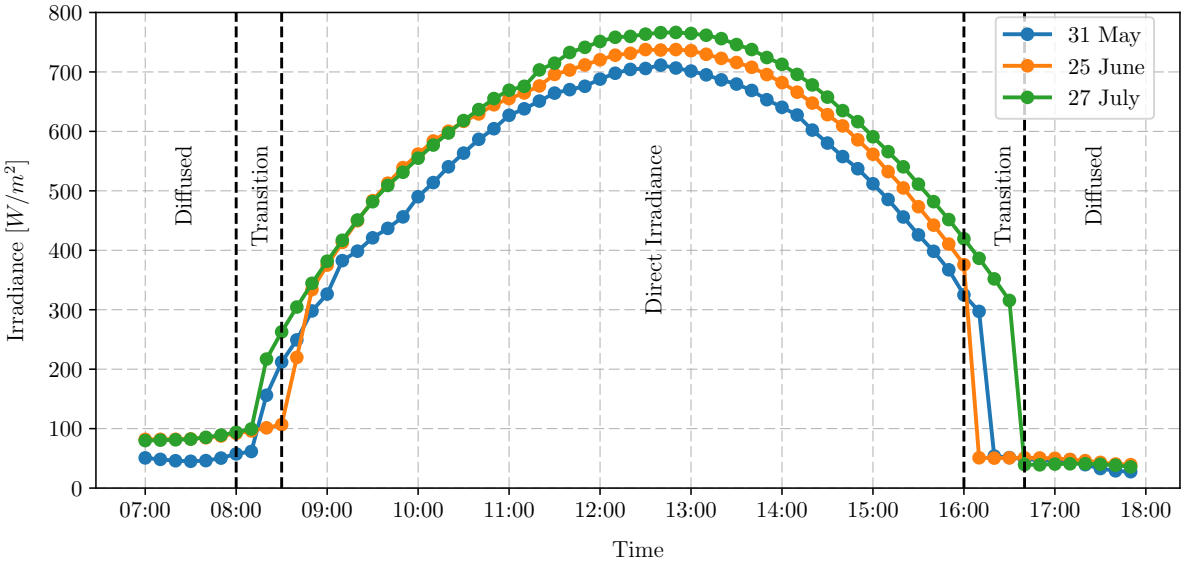

Figure 4.22: Categorisation of the times of data measured thought out the measuring period

The first category of data are before 7:50 and is labelled as diffused. The transition category is data from 8:00 to 8:30. The direct category is from 8:40 to 15:50. The second transition is from 16:00 to 16:40 and the last diffused category is from 16:50 to 18:00.

4.5.4 AM1.5G Comparison

The comparison of a measured spectrum to the AM1.5 global spectrum is contained in Figure 4.23. It is evident that the data measured correlates closely to the standard spectrum with all the dips and noise as that of the AM1.5 global spectrum. The measurement is taken at 14:00 on 6 June 2017. The Zenith angle at that time was measured at 33.13^o, thus an AM value of 1.19. The lower AM value shows the higher radiation of the measurement compared to the AM1.5 global measurement.

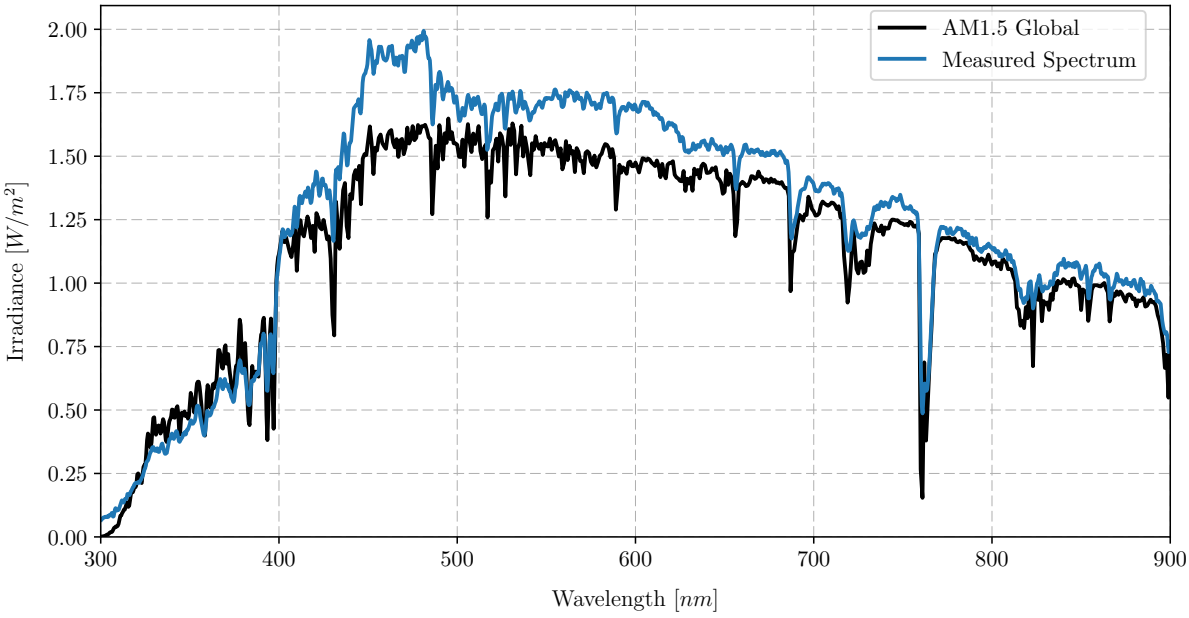

Figure 4.23: Comparison between the AM1.5 global spectrum and a measurement taken

4.5.5 SAURAN Comparison

The SAURAN weather station's data are compared to the measured spectrum data. The SAURAN station does not measure the spectrum. Thus the spectrum measured with this set-up was integrated and compared to the DHI measured by SAURAN. The comparison is shown in Figure 4.24. The integrated spectrum is higher. This is a result of the measurement of the spectrometer's receptor that is 30^o tilted. At 16:00, the shadow of the adjacent building is cast on the measuring equipment and can be seen from the comparison. The offset at the beginning and the higher irradiance measured can be a result of the dark spectrum that needs to be subtracted that is actually higher than the value provided by the manufacturer of the spectrometer.

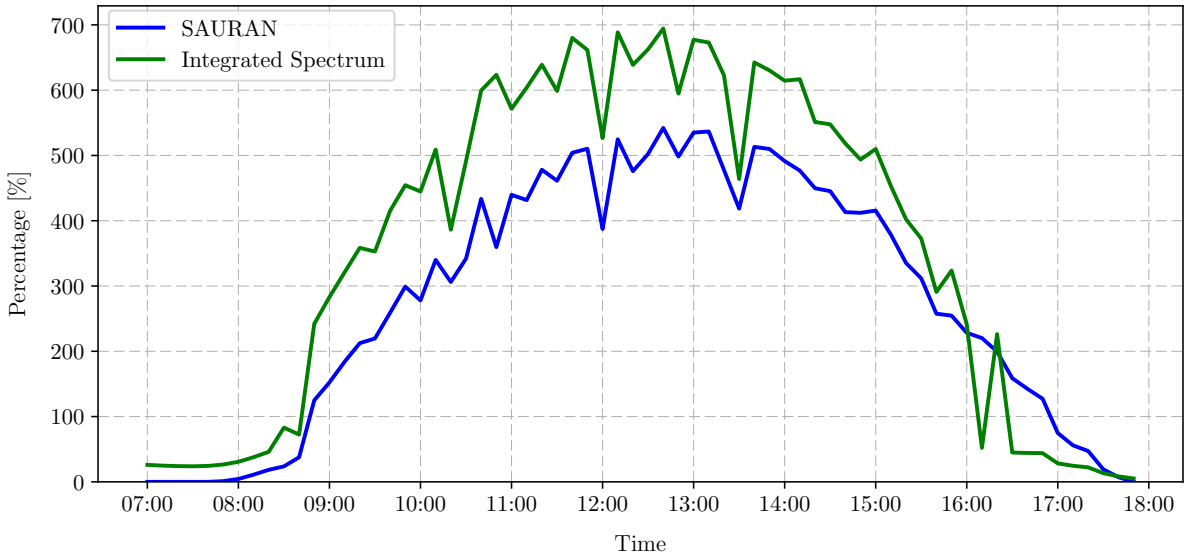

Figure 4.24: Comparison between the measured integrated spectrum and SAURAN's irradiance data

4.6 Data Analysis

All the data measured are stored on the database for analysis. The analysis of the spectrum is done through Python scripts. Studying the data began by first looking into the different bands of defined light, thus the visible, infra-red and ultra-violet light.

A comparison between the spectrum received by the solar module and the output performance of the module is studied. Correlations between the spectrum and the power are shown. Some of the quantifying methods discussed are used to quantify the spectrum and to show correlating factors.

Interesting observations are also shown that were seen with the execution of this study. These include the temperature of the module and wind speed analysis. The effect of the bypass diodes were also observed and shown.

4.6.1 Colour Analysis

In Figure 4.25, the AM1.5 global spectrum is shown with the different colour bands, defined by the wavelengths on it. The AM1.5 global spectrum is used as a reference in this study. Only the section from 300 nm to 900 nm is used as it is what the measuring device can measure with certainty and accuracy which was proved in the data validation section. Only data from clear days will be used to analyse the colour bands in the spectrum, because the overcast conditions will influence the data as spectrum varies with the variation in cloud covering throughout the day. The data of an overcast day are also shown to illustrate the variation in the colour bands.

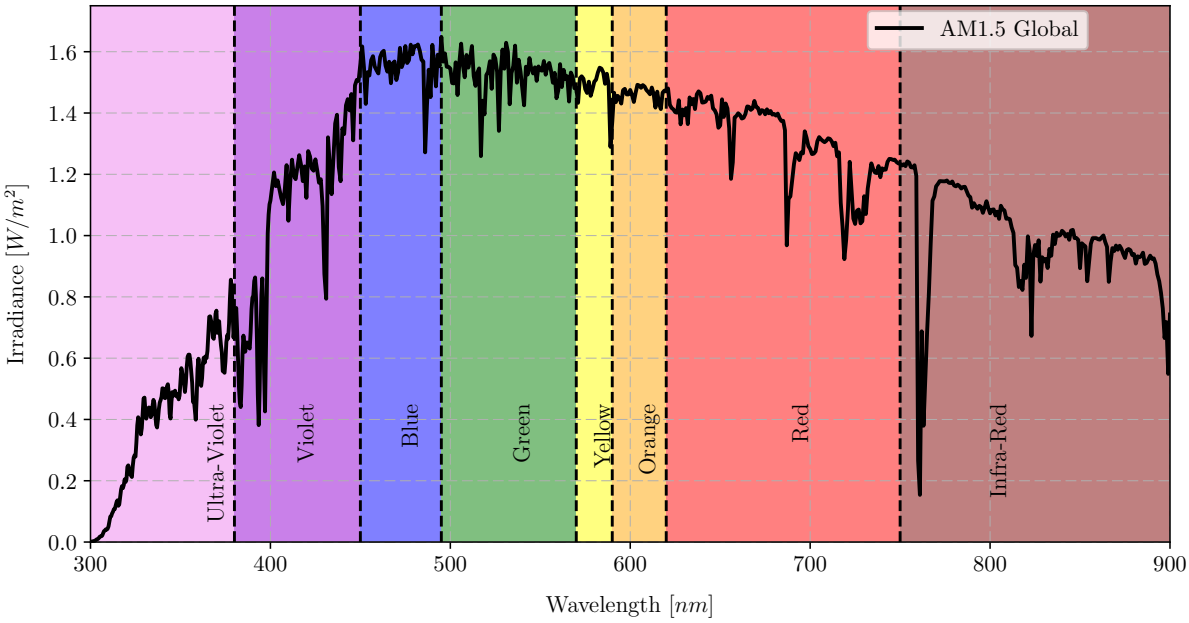

Figure 4.25: Spectrum colour divisions

Each colour band in the spectrum is integrated to give the irradiance per colour band. The colour is presented as a percentage of the total spectrum's irradiance. Table 4.6 shows the percentage of each colour as well as ultra-violet and infra-red. These values are used later to compare the actual measured spectrum against the reference spectrum under which solar modules are tested by manufacturers.

Table 4.6: Percentage of colour represented in the spectrum of AM1.5 global

Band	Percentage
UV	4.79 %
Violet	11.12 %
Blue	10.23 %
Green	16.73 %
Yellow	4.34 %
Orange	6.41 %
Red	24.82 %
IR	21.54 %

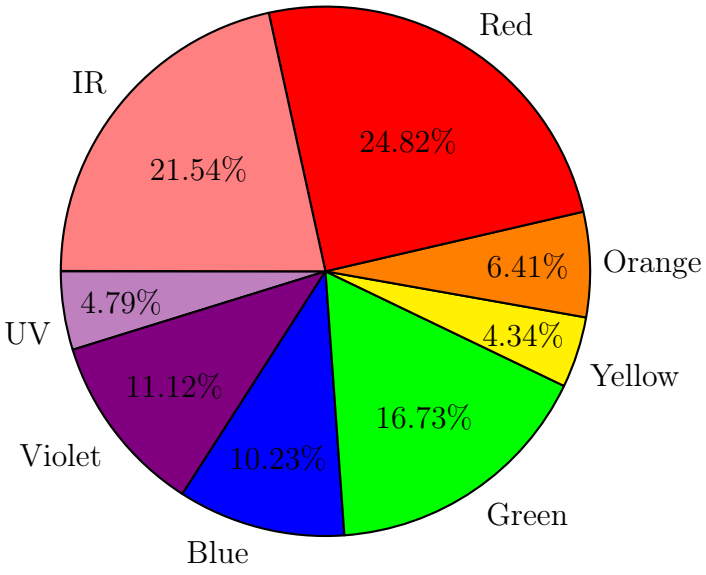

Figure 4.26: Spectrum colour divisions Pi diagram

4.6.1.1 Full day's measured data

With the data recorded, the result of the spectrum can be categorised into two types of days: clear and overcast. In this analysis, it is shown how the spectra of these two different

days look and how the percentage of colour varies within the spectrum throughout the day. It is important to understand that all the calculations are done with data only between 300 nm and 900 nm. Figure 4.27 shows each colour that the spectrum has on a percentage scale for an entire clear day. Figure 4.28 shows the same, but for an overcast day.

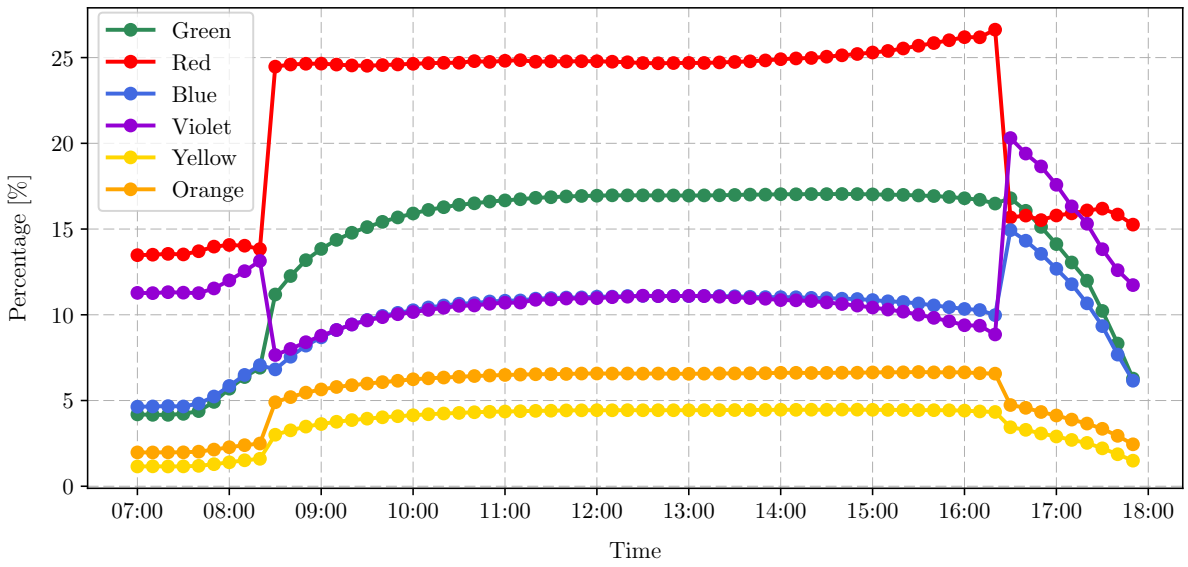

Figure 4.27: Percentage colour throughout the clear sky day

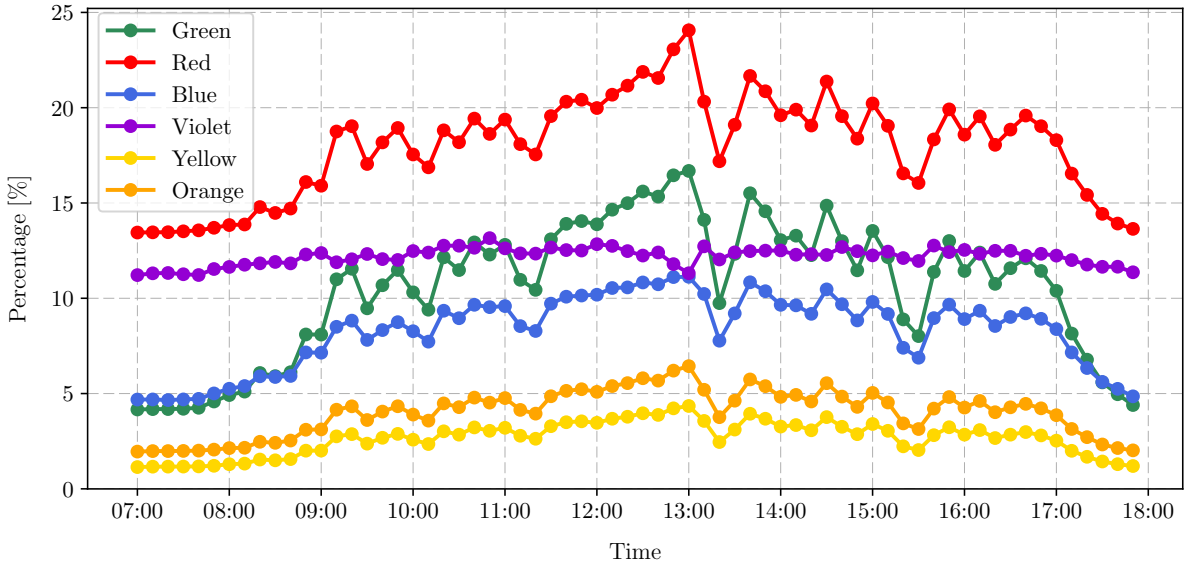

Figure 4.28: Percentage colour throughout the overcast sky day

The ultra-violet and infra-red parts of the spectrum are shown in Figure 4.29 and 4.30. Although it is not part of the colour spectrum, it is part of the spectrum band to which the solar module responds.

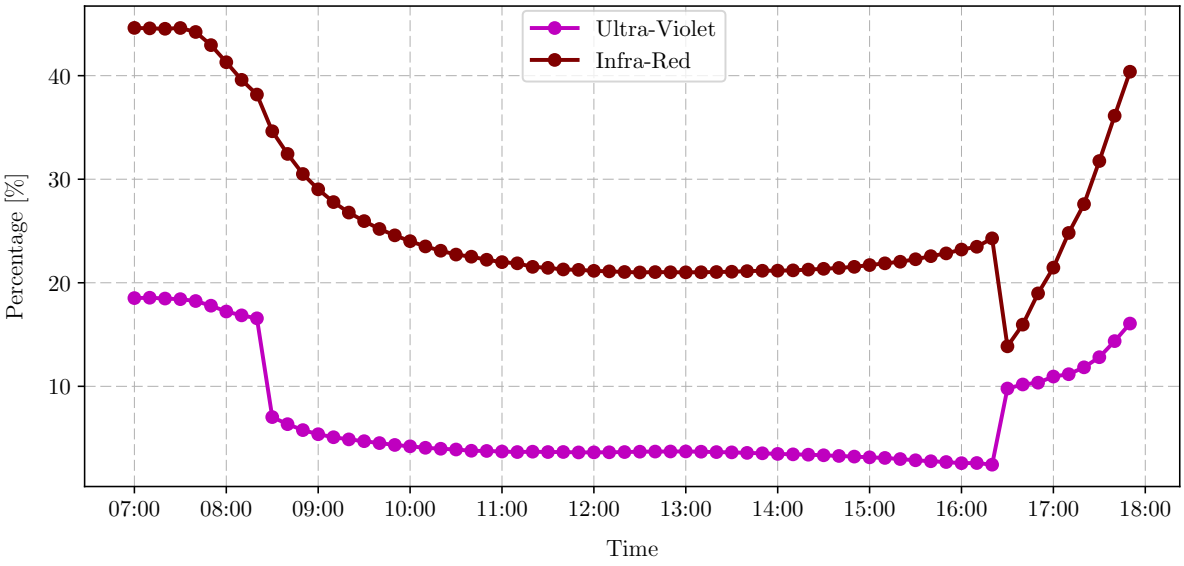

Figure 4.29: Percentage ultra-violet and infra-red light throughout the clear sky day

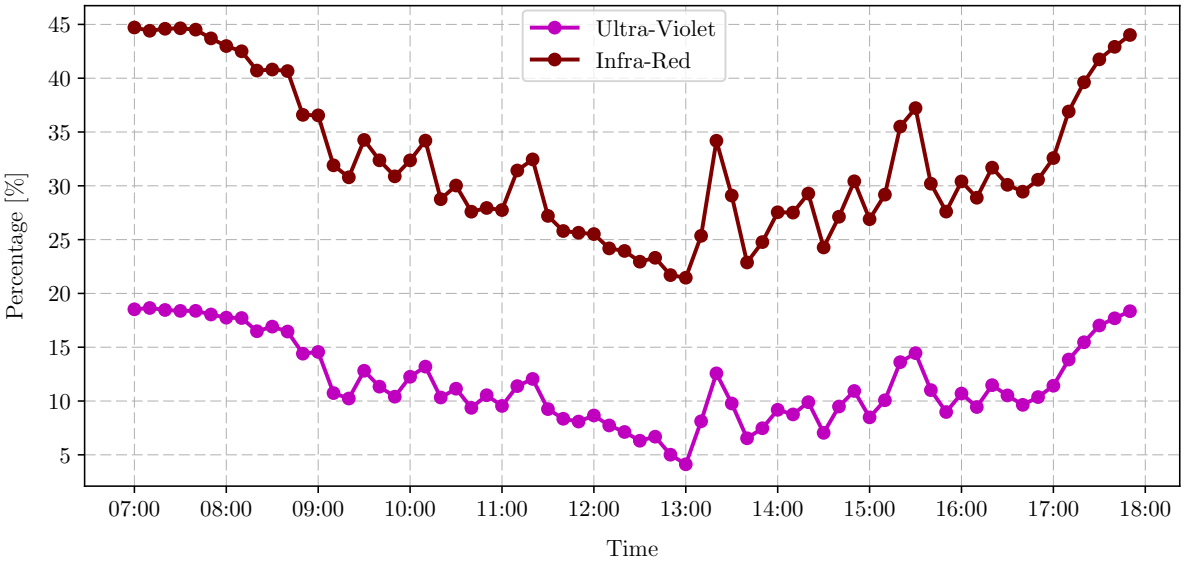

Figure 4.30: Percentage ultra-violet and infra-red light throughout the overcast sky day

From the figures presented, the difference between the clear and overcast days is evident. When a cloud passes over the measurement equipment, most of the colour band's spectra percentage drops and, thus the increase in percentage in the other bands (infra-red and ultra-violet).

4.6.1.2 Individual colour band analysis

The study further only uses the direct irradiance part of the data that were measured. This is to find a trend for the different colours on clear days and to compare the spectra measured to the ASM1.5 global spectrum. As one can see the categories for this study are important. The data from 8:30 to 16:00 were taken and filtered to give 8 clear days

in the measuring period. These 8 days are analysed together, because they must have more or less the same light spectrum. From this data, one can see the trend of the colour amounts in the spectrum.

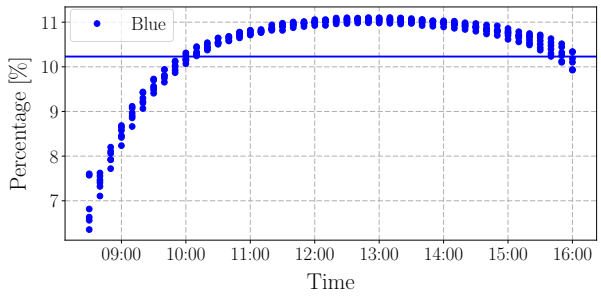

Figure 4.31: Blue light band percentage in the spectrum

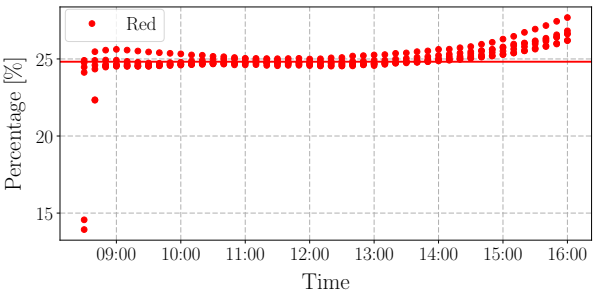

Figure 4.32: Red light band percentage in the spectrum

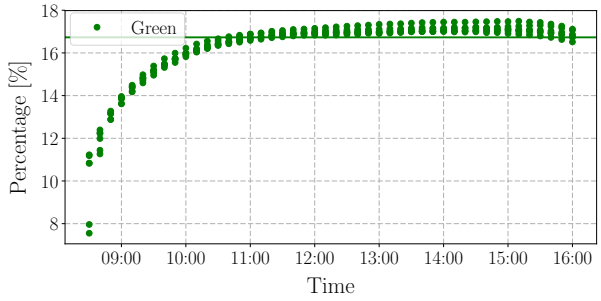

Figure 4.33: Green light band percentage in the spectrum

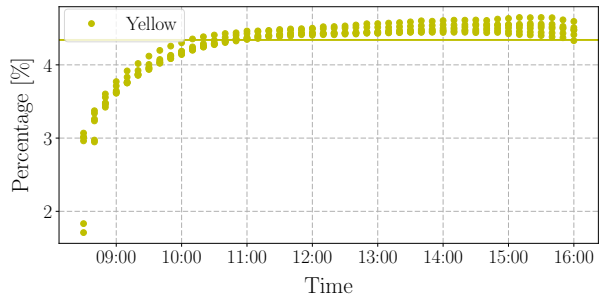

Figure 4.34: Yellow light band percentage in the spectrum

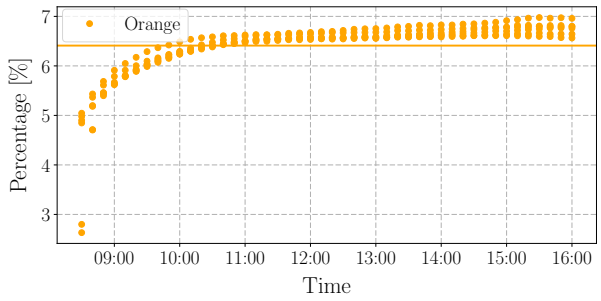

Figure 4.35: Orange light band percentage in the spectrum

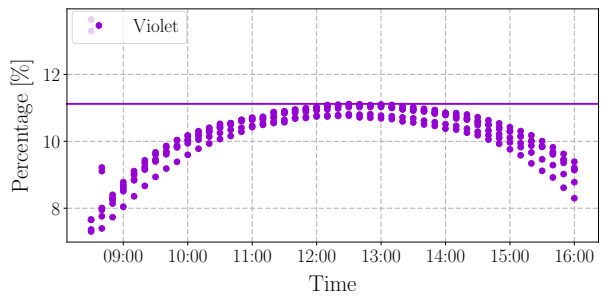

Figure 4.36: Violet light band percentage in the spectrum

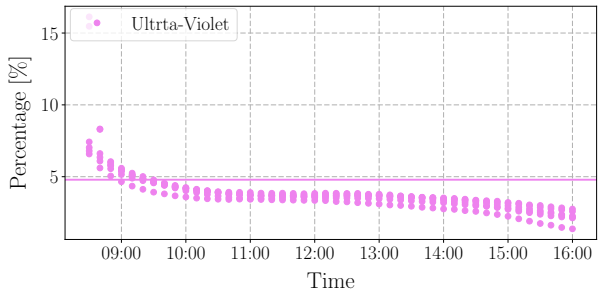

Figure 4.37: Ultra-Violet light band percentage in the spectrum

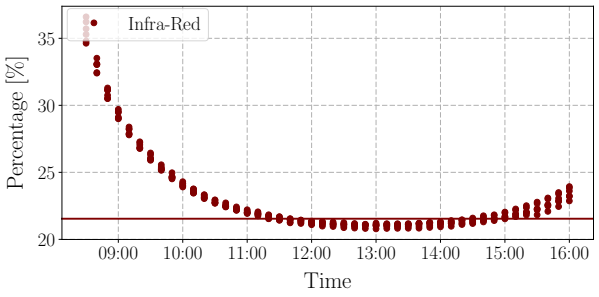

Figure 4.38: Infra-Red light band percentage in the spectrum

A result from this band plot of the spectrum shows that the standard AM1.5 global differs from the actual measurements. In some bands the percentage that contributes to the irradiance is less and in others it is more. This also changes for each band throughout the day. The percentage of each band in the AM1.5 global spectrum is shown as a line on each graph. It is evident that the spectrum does not follow this reference line where the solar module's parameters are tested by manufacturers.

The blue light band is inversely proportional to the infra-red band. The red band is also inversely proportional to the ultra-violet band. This is an interesting observation as the spectrum bands are opposite to each other in the spectrum.

4.6.2 Average Photon Energy

The APE of the clear days in the data measured is presented in Figure 4.39. It is clear that the APE starts low when the direct irradiance reaches the spectrometer, which indicates a redder spectrum. The APE indicates that as solar noon is reached, the bluer the spectrum becomes. After solar noon, the spectrum is shifted towards the red side again. In the transition and diffused light times in the morning and afternoon, the scattered measurements result in a bluer spectrum shift. This is a confirmation that blue light scatters more than red light [15]. In Figure 4.40, the APE of the cloudy days are shown. When a cloud is in the path of the rays and the measuring equipment, the spectrum is shifted more to the red side. This is because the higher frequencies of the blue side become scattered by the water particles in the clouds, thus losing energy [48]. The low frequencies of the red light pass through the cloud with little direction change [25]. Figure 4.40 shows that the APE value indicates blue and red scattering of the spectrum. It is important to look at this result, knowing that this is only a part of the spectrum as defined, and not the full range of the spectrum.

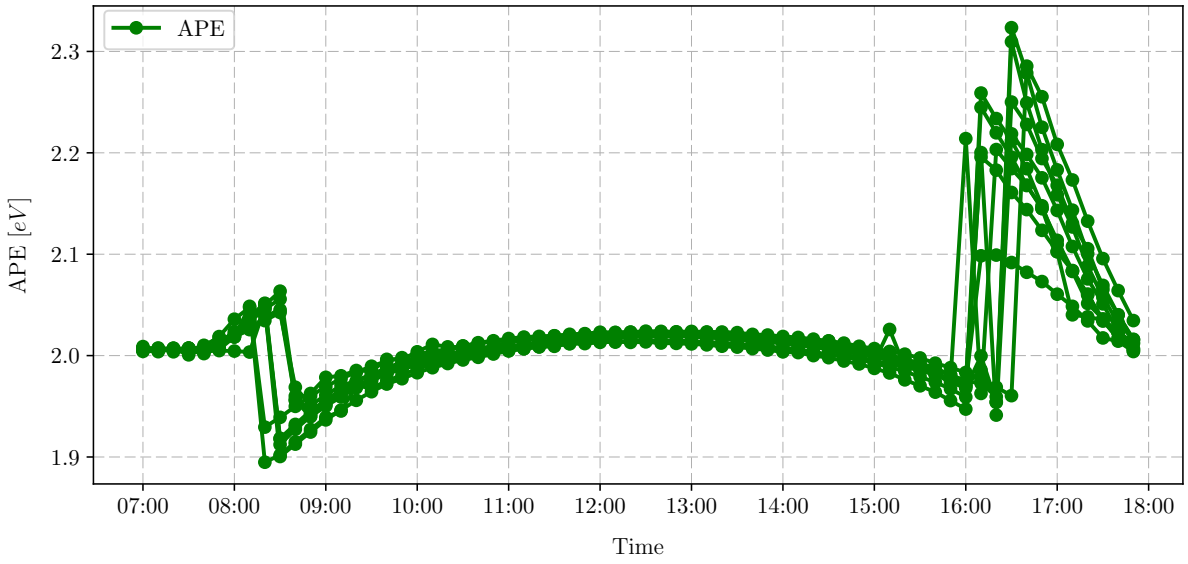

Figure 4.39: APE of clear days in the data

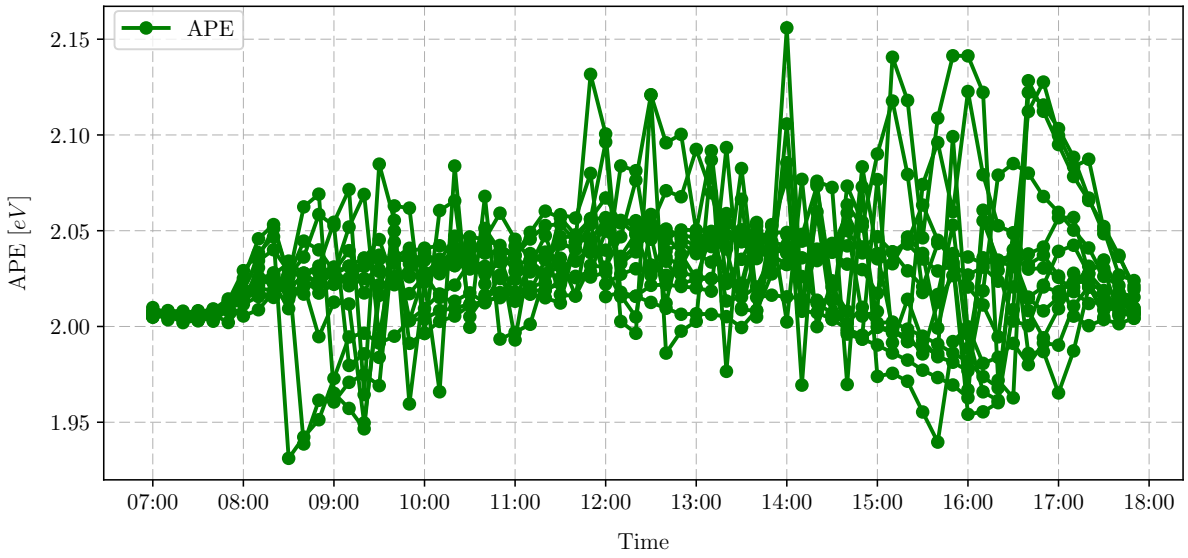

Figure 4.40: APE of cloudy days in the data

The APE is compared to the open circuit voltage and the short-circuit current of the solar module to see the relationship between the shift of the spectrum and the performance of the solar module. Figure 4.41 shows the comparison between the APE of a clear day and the current produced by the solar module. The current has a proportional relationship to the APE in the direct radiation timeslot. Thus the bluer the light, the higher the current. Figure 4.42 shows the voltage and the APE comparison of the same day. Here the APE has an indirect proportional relationship to the voltage. The redder the spectrum, the higher the voltage. It is evident from the results that the APE has a different relationship if the light is diffused before and after direct irradiance.

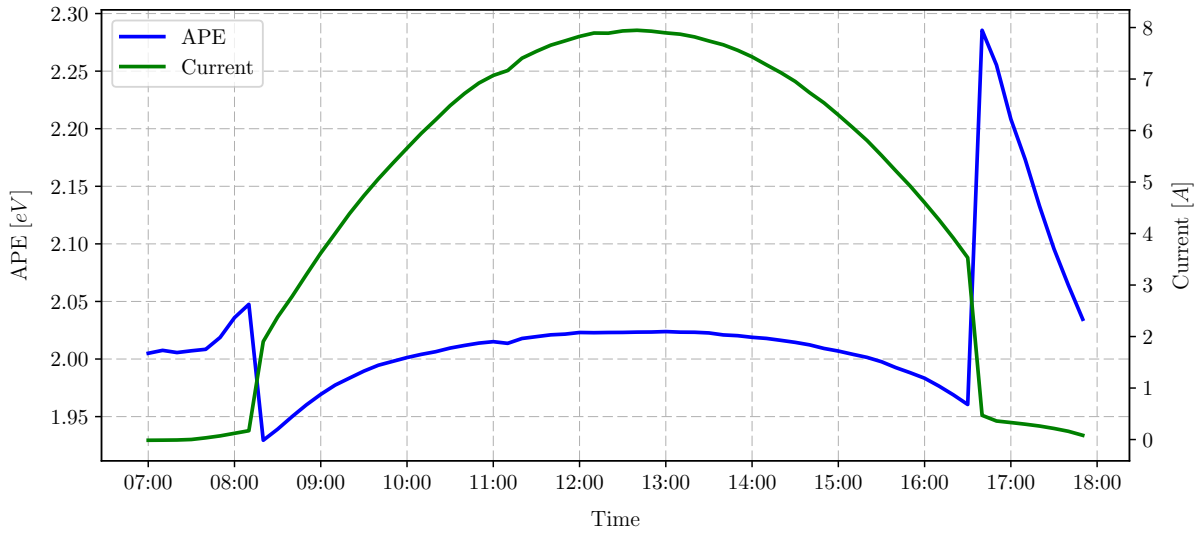

Figure 4.41: APE of a clear day compared to the produced current

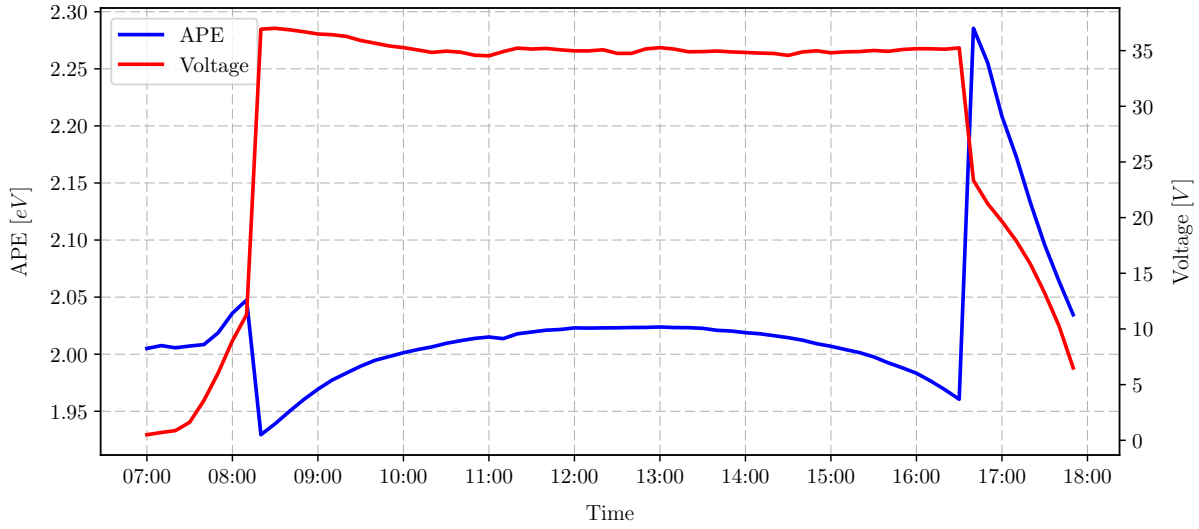

Figure 4.42: APE of a clear day compared to the produced voltage

4.6.3 Temperature analysis of a clear day

The temperature of the module is analysed for a full day in Figure 4.43. It is seen that the module temperature climbs and then after 12:00 the temperature drops. If one looks at the ambient temperature, the temperature stayed constant. The wind speed is the factor which plays a role here. If one looks at the wind speed, it picked up just before 12:00. This explains the drop in module temperature. After 16:00, the shadow of the building falls onto the set-up, thus the temperature drops rapidly.

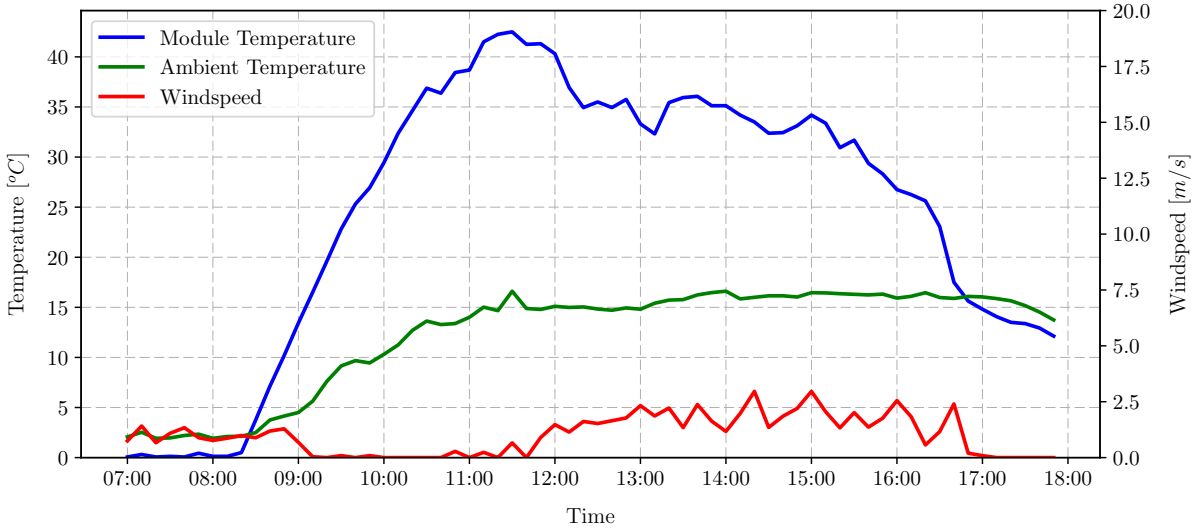

Figure 4.43: Temperature analysis of a full day

4.6.4 Bypass diode observation

A specific measurement in the data measured on the active load is interesting. The shadow that the building casts after 16:00 on the solar module was able to activate the bypass diodes. Figure 4.44 shows the IV-curve that was measured.

These measurements of the IV curve correlate with typical module shading and the activated bypass diodes are shown which in turn again shows the validation of the measurement data.

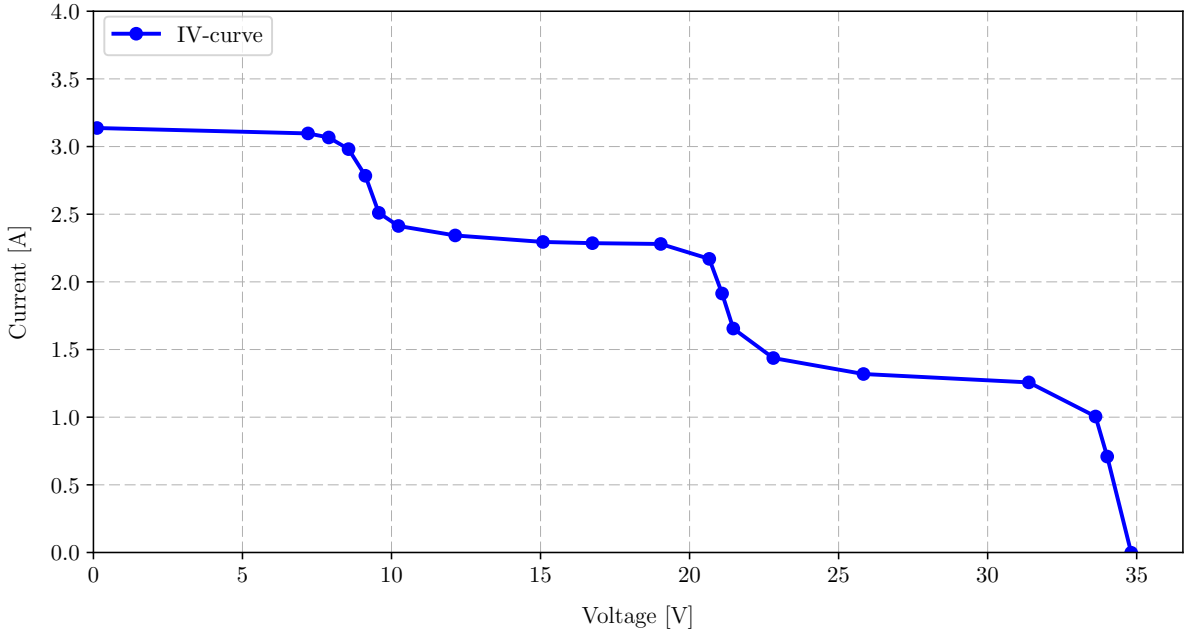

Figure 4.44: IV-curve of shading on the solar module

The solar module used in this study has 60 cells with three bypass diodes for each series string of 20 cells that are connected in 3 parallel branches. Thus each branch has a bypass

diode. Cells are wired in series by the manufacturer to achieve the desired voltage. If one cell is shaded in a series string of cells, it is the limiting factor for the current that the string can produce. The shaded cell acts as a load and current that flows through the cell causing the cell to heat up. The result of excessive shading is the so called "hot-spot" phenomenon. The solution for this problem is a bypass diode across the cell that is shaded. The current will flow through the bypass diode instead of through the shaded cell. The bypass diode is forward biased when a cell is shaded, because the shaded cell causes a voltage drop across the diode [18].

So what is happening in this case? The building is partially shading the solar module. The bypass diodes are connected to prevent that the series connected strings go into reverse bias. The active load starts to extract the IV-curve from the module. The IV-curve is extracted by changing a load resistor to change the current and voltage of the solar module. So when the active load is demanding current from the shaded solar module, and the current is above the current of the string containing the shaded cells, the bypass diode will be activated. Thus, when the load is increased, the current that is required increases above the ability of the shaded string. The bypass diode is then activated, reducing the total amount of current. This occurs at two of the diodes when the IV-curve is measured, because of the way the shadow is cast onto the module shown in Figure 4.45.

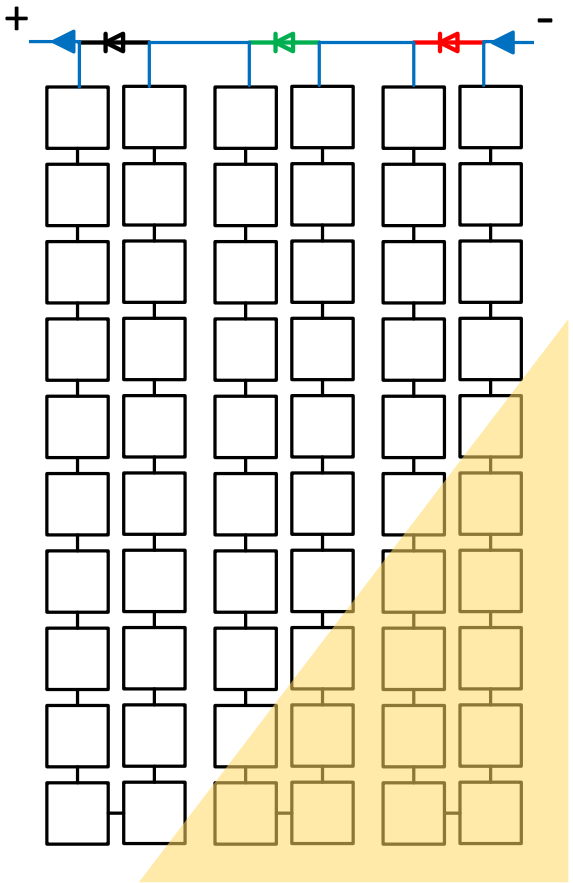

Figure 4.45: Possible shading on the solar module

4.7 Summary

In this chapter, the different quantification methods used to quantify the solar spectrum are discussed. Key aspects of the SR and QE of the semiconductor material type are shown as well as the response they have when the material is subjected to radiation.

An automated system is designed and integrated with a database to store the measured data. The automated system is specifically designed for this study and serves as a guideline for further studies in this field. The utilisation of a local database and the hardware used to ensure redundancy is given. The solar spectrum is measured with the IV-curve. All the software around the system is explained with the GUI to give the user live spectral monitoring.

The data measured is validated with reference spectra and other weather stations near the measuring location. Results show that the different colour components within the measured spectra differ throughout the day. An important observation is that the components differ with the standard AM1.5 global the solar modules are tested at by manufacturers. This is of concern as the performance and parameters supplied by the manufacturer is never reached. The test conditions need to be adjusted to give the user an accurate reference with regards to physical conditions to which the module will be subjected.

Important shading analysis is shown that is observed. This is physically measured and is part of the dataset. The data is an indication that the data measured is valid and that the module is subjected to field conditions to observe the problems they observe.

Chapter 5

Conclusion

This chapter contains an overall summary of findings of the work done in this thesis. The results in each chapter are discussed in summary. The work's conclusions and recommendations are divided into two main groups: the parameter extraction (Chapter 3) and the spectral analysis (Chapter 4).

5.1 Parameter extraction

In this part of the thesis, IV-curve parameter extraction is compared to De Soto's method of parameter extraction. De Soto's method's MPP is adjusted with an adjustment function. The individual parameters are investigated and new extraction equations are presented.

5.1.1 Conclusion and remarks

The implementation of De Soto's method results in an error of 13.71% on the MPP extraction. The adjustment on De Soto's result resulted in an increase in accuracy of the MPP of De Soto's method. The error of the adjustment function to the actual parameters were only -2.99%. This function gave an error of only -0.062% after the coefficients were optimised through linear optimisation.

The individual parameter study resulted in adjustments made to the equations that De Soto recommends in his parameter extraction equations. Each adjustment resulted in an increase in accuracy with regards to the actual parameters extracted from the IV-curve. The adjustments on all the parameters contributed to an improvement in accuracy at -1.73%. It is observed that the diode saturation current influences the error made with De Soto's method the most. In some parameters, it is important to decide if accuracy is more important than the computational time. The time to do calculations on the database's data took about two days, compared to using a constant value.

The optimisation of the adjustment function to De Soto's method to calculate the power accurately is recommended if the MPP is the only parameter that needs to be extracted and is of importance from the temperature and irradiance. If more specific parameters are required, the individual parameter equations can be used as presented. The new individual parameter equations describe the measured IV-curve's parameters better than De Soto's method.

With the increase in accuracy, this method can be used in forecast models to predict solar plant performance with only historical temperature and irradiance data. It is important to note that a year's data is needed to take seasonal change and weather data into account. Thus this method is ideal for prediction if specific environmental conditions are required to be tested for yield. It is an easy to use method that does not require more data than the temperature and irradiance to predict the performance of a solar module accurately and quicker for specific temperature and irradiance conditions. Other methods require more parameters, such as the open circuit voltage and short circuit current, to predict the module's yield.

5.1.2 Problems and possible improvements

- The improvement of De Soto's method must be verified with another dataset from another solar plant.
- Generic algorithms can be developed that automatically extract the adjustment function from only a short period of detailed solar plant data.
- Improvements on the parameter computational time is recommended. Some calculations took two days to run through the database to complete. This can be improved by using smarter code or a local database.

5.2 Spectral analysis

Spectral analysis is conducted with the use of an automated spectrum measurement data acquisition system. The system measure the solar spectrum and extracts the IV-curve of the solar module. This system gives important insights on the environmental conditions to which the module is subjected.

5.2.1 Conclusion and remarks

The colour bands in the spectrum showed that red is the dominating band in the spectrum that is measured. The difference in the clear and overcast day's data is very different with regards to the colour bands. The variation in cloud cover scatter the colour bands and lower the irradiance, in comparison to a clear day. The relationship of the APE of the irradiation and the output voltage and current of the solar module is shown. The current is proportional to the APE, but only in direct radiation conditions. The voltage is high at any form of direct light, thus in the morning when the sun rises from the mountain the voltage jumps to the rated open circuit voltage and drops when the shadow of the building is cast onto the module.

The comparison between the spectrum measured and the standard AM1.5 global spectrum that is used by manufacturers to test solar modules resulted in an important observation. The spectrum does not follow the trend of the AM1.5 global and varies throughout the day in terms of the amplitude and the spectral distribution. This is known, but the amount it varies is of concern. The standard AM1.5 global spectrum was also never observed, thus a more accurate actual field spectrum must be used by manufacturers to test the solar module to give an accurate performance in the data sheet of the module. A suggestion of multiple spectral variations from different parts of the world must be used

to test solar module performance. This will result in module selection that is optimal to the environmental conditions in a specific area.

From this study it is evident that the spectrum also plays a role in modelling of PV, especially when the conditions are not STC. The solar spectrum can change considerably and it is important to take it into consideration when accurate modelling of PV is conducted.

5.2.2 Problems and possible improvements

- The servo used for the shutter does not work sometimes after heavy rain and wind. The shutter design can be improved to enclose the servo to protect the servo from the environmental elements.
- The power failed for the reason that the power supply to the facility was in a plug with multiple users who tampered with the plug. A dedicated power supply can be used to reduce power failure issues that affect the data measurements.
- The active load used to measure the IV-curve has the habit of corrupting data after a power failure during a measurement. New improved systems are currently in the development process which can be used in future studies.

Appendices

Appendix A

Spectrometer Bracket Design

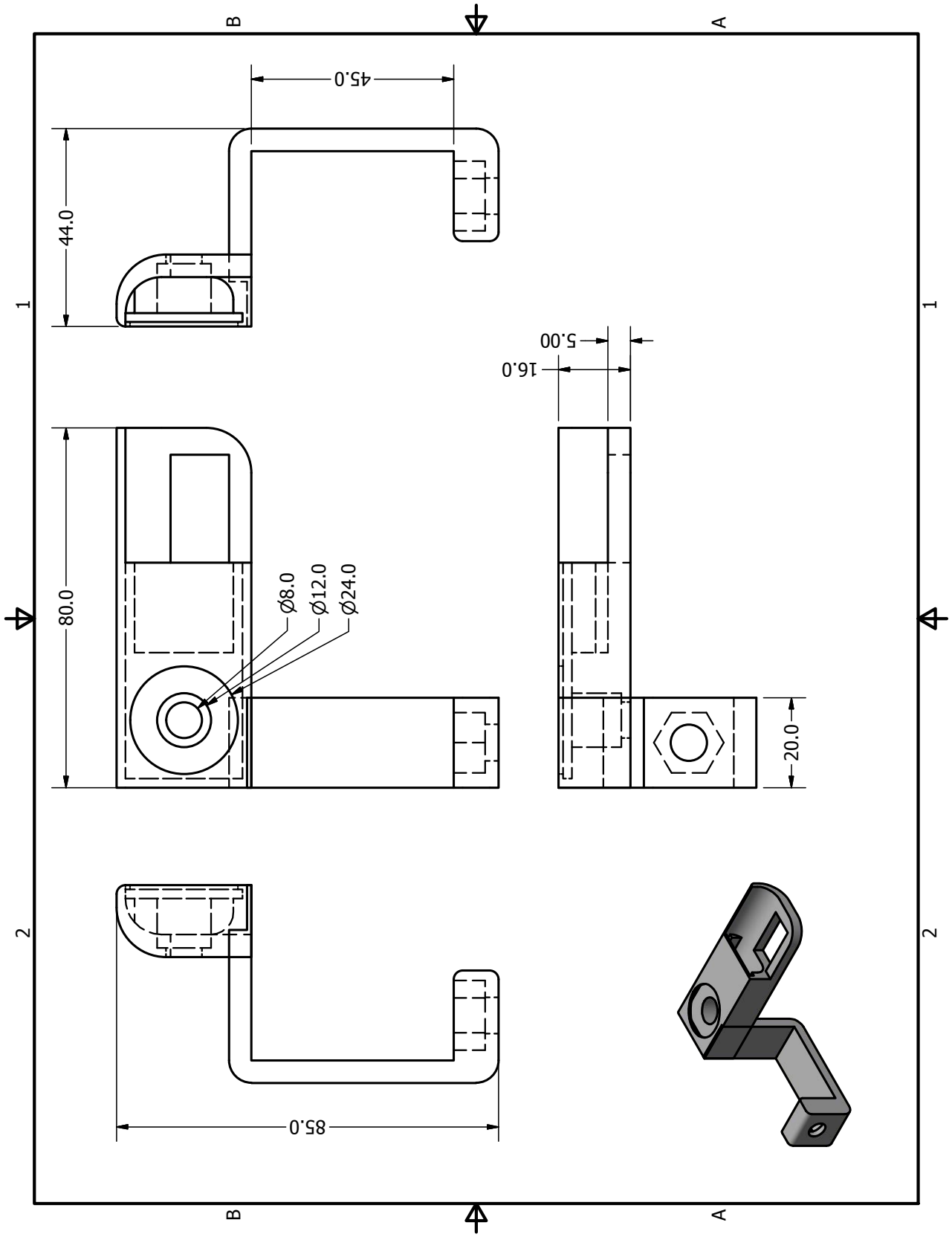

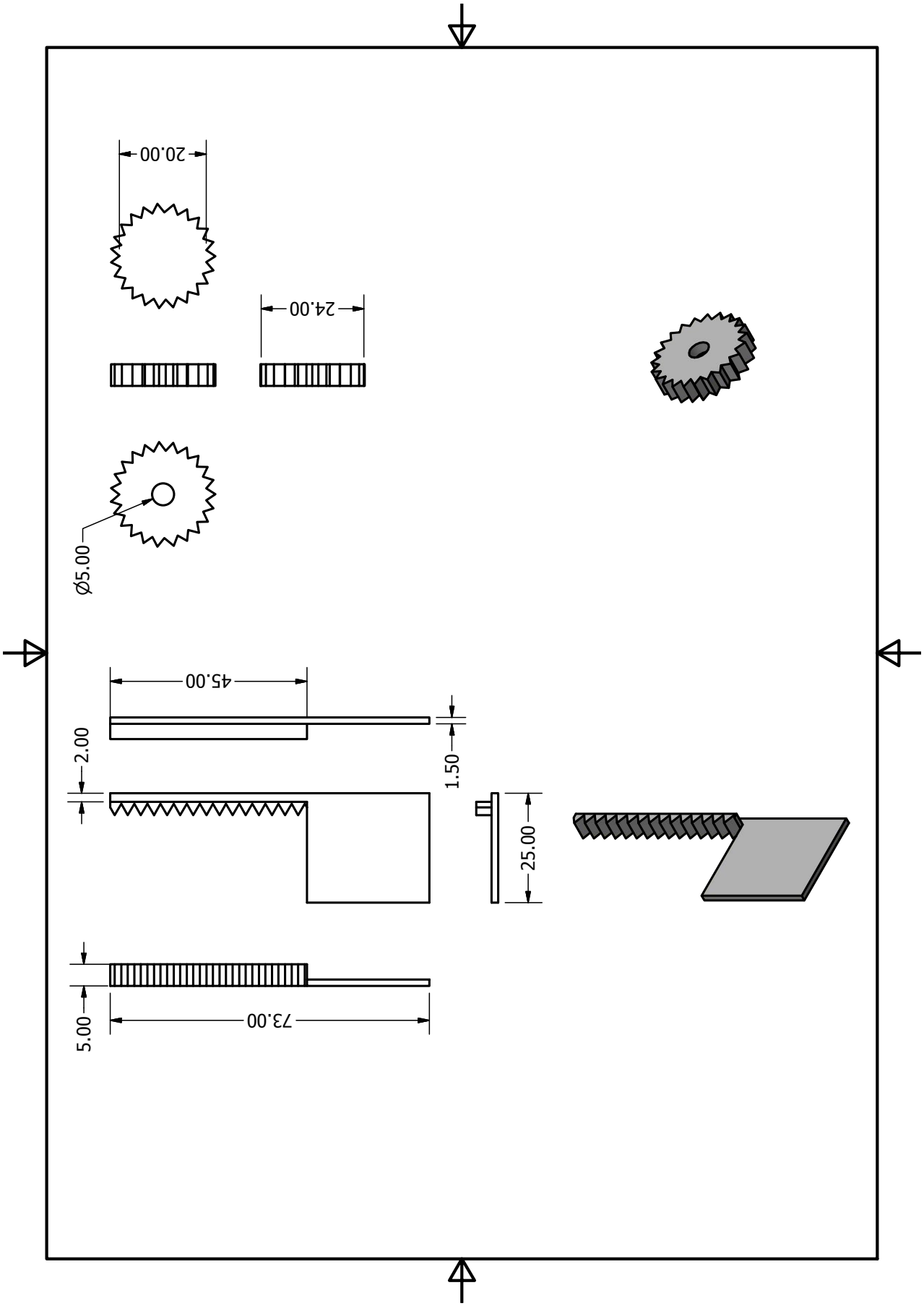

Appendix B

RAID1 Set-up Guide

B.1 Introduction

RAID is used in this application to prevent data loss if the hard-drive fails. A software RAID1 is configured with three hard-drives. The hardware is connected to the SATA ports on the motherboard. It is recommended that the hard-drives that are used for RAID is of the same size and manufacturer to avoid issues. This set-up was done with different hard-drive sizes, but is partitioned correctly. This can result in some issues or failing of the RAID, if not configured correctly. The rest of the set-up is done with software through the Ubuntu Server software installation. The guide that was followed, is adopted from the Ubuntu help community page [28].

B.2 RAID1 Set-up Guide

The set-up guide is basic and intended for persons that are familiar with command line commands in the Linux environment. Steps to configure the RAID are condensed, but all the steps you need to know about, are discussed.

B.2.1 Step 1

Create a bootable USB drive with Ubuntu server 17.04 on it. The software ISO can be requested from the Ubuntu site [31]. The bootable USB drive can be created with Rufus software [8], with the ISO file.

B.2.2 Step 2

Insert the USB drive into the server computer with the drives connected as required. Start the server and press F2 until the boot menu appears. Select the USB drive as the boot drive. The Ubuntu installation selection page will appear. Select "Install Ubuntu Server". At this stage it is important to know that all the data on the hard-drives will be repartitioned, thus all the data will be erased. Provide the installation with the information asked.

B.2.3 Step 3

This is the partition step. Select "Manual" when asked for the partition method. You must be able to see all the hard-drives connected to the computer. If there are previous partitions on the hard-drives, erase it and also the data on it. You need to know the amount of RAM the server has. The hard-drives need to have a partition on it that is twice the size of the RAM of the server, to use as SWAP memory. This is a general rule to ensure that the server software operates correctly. Select "Create a new empty partition table on this device?". Select the "FREE SPACE" on the drives to "Create a new partition". The size of the partition needs to be typed in. The rest available space on the hard-drive can be partitioned from "Ext4 journalling file system" to "Physical volume for RAID". You can finish the partition by "Done setting up partition". For this RAID, the drives must have exactly the same partitions on and configured as Primary drives and from the Beginning.

B.2.4 Step 4

The partition is now completed. The drives must have the same partitions on now. The "Configure Software RAID" can now be selected. RAID1 is going to be configured which include two parts: one for the SWAP and one for the file system, RAID. Choose the "Create MD device" option. Select the swap partitions on each hard-drive and select SWAP as the hard-disc type. Select the RAID partitions on each hard-drive and select the root directory "/" as the mount point. Select "Finish partitioning and write changes to disc ". The number of active drives will be asked and for spare devices you can say "0".

B.2.5 Step 5

The RAID1 configuration is now finished. The set-up of the server will continue. When the total installation is finished, the server will be able to start from any hard-drive, as the boot-loader is on all the drives with all the data.

B.3 RAID Status

The status of the raid can be checked with "cat /proc/mdstat" and the following should be the same as in Figure B.1 The server has three drives, thus the "sda1, sdb1, sdc1" for SWAP and "sda2, sdb2, sdc2" for the root directory. The "$[UUU]$" says that the drives are all synced and active. If one of the drives is faulty, the status will show, "$[UU\_]$". The syncing process can take time, but the status can be checked with "watch -n1 cat /proc/mdstat" command.

```
root@pvlab:/home/pvlabpvlab# cat /proc/mdstat
Personalities : [raid1] [linear] [multipath] [raid0] [raid6] [raid5] [raid4] [raid10]
md1 : active raid1 sdb2[1] sda2[0] sdc2[2]
      136587264 blocks super 1.2 [3/3] [UUU]
      bitmap: 1/2 pages [4KB], 65536KB chunk

md0 : active raid1 sdb1[1] sda1[0] sdc1[2]
      15616000 blocks super 1.2 [3/3] [UUU]

unused devices: <none>
```

Figure B.1: Command-line output for the RAID1 server for "cat /proc/mdstat"

Figure B.2 shows a photo of the server computer. The three hard-drives that are connected to the SATA ports on the motherboard can be seen. An extra fan was added to the case to help with the temperature in the case with the extra hardware.

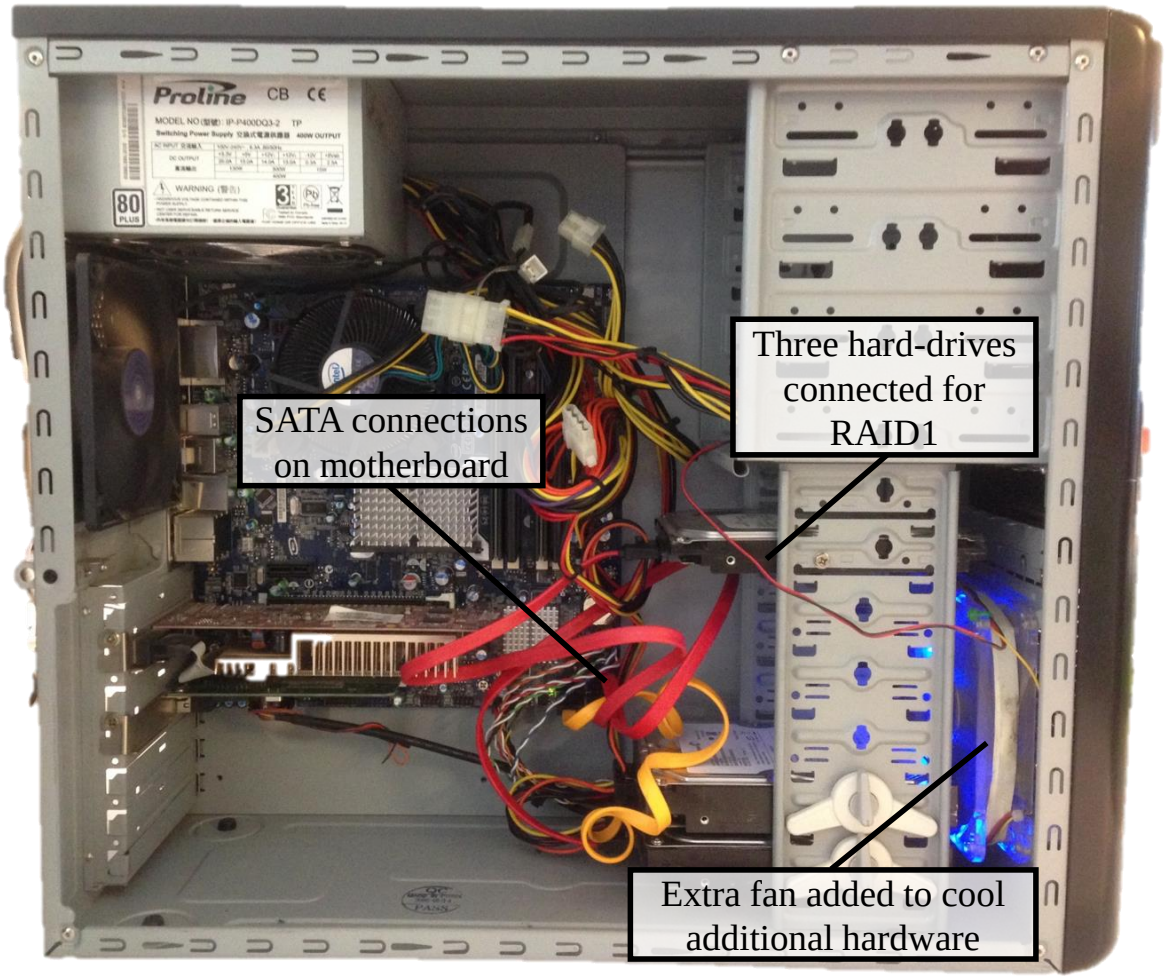

Figure B.2: Photo of the server hardware

List of References

[1] Africa, S. (2017). Rs components (sa). [Accessed 12 July 2017].
Available at: http://za.rs-online.com/web/

[2] Agafonkin, V. (2009). Suncalc. [Accessed 16 August 2017].
Available at: http://suncalc.net//-33.9285,18.8662,16/2017.08.04/13:17

[3] AGGARWAL, V. (2017). What are the most efficient solar panels on the market? [Accessed 23 July 2017].
Available at: http://news.energysage.com/what-are-the-most-efficient

[4] Association, E.E.P.I. (2015). Global market outlook for solar power. [Accessed 13 August 2017].
Available at: http://www.solarpowereurope.org/fileadmin

[5] Association, S.A.A.E. (2017). Exploring the south african green energy space. [Accessed 13 July 2017].
Available at: http://www.saaea.org/news/category/reipppp

[6] Bartlett, J. (2017). History of photovoltaic (pv) solar energy. [Accessed 5 July 2017].
Available at: http://ariseenergy.com/training-education/history

[7] Becquerel, A. (1839). Recherches sur les effets de la radiation chimique de la lumiere solaire au moyen des courants electriques. *Comptes Rendus de L´Academie des Sciences*, vol. 9, pp. 145–149.

[8] Bootable, R. (2017). Rufus bootable drive software. [Accessed 13 June 2017].
Available at: https://rufus.akeo.ie/

[9] Brochure, M. (2014). Met one instruments, inc. [Accessed 15 March 2017].
Available at: http://www.metone.com/brochure/

[10] Bunea, G., Wilson, K., Meydbray, Y., Campbell, M. and Ceuster, D.D. (2006 2006). Low light performance of mono-crystalline silicon solar cells. In: *4th World Conference on Photovoltaic Energy Conference*, p. 1312–1314. Waikoloa, HI.
Available at: http://ieeexplore.ieee.org/xpls/absall

[11] Cairns, J. (2016). Electrical efficiency of a solar cell. *Undergraduate Journal of Mathematical Modeling*, vol. 6, no. 2, pp. 1–11.
Available at: http://scholarcommons.usf.edu/ujmm/vol6/iss2/1

[12] Carr, G. (2015). Alternative energy will no longer be alternative. [Accessed 29 April 2017].
Available at: https://www.economist.com/news/alternative-energy

[13] Choi, C.Q. (8 February 2017). Earth's sun: Facts about the sun's age, size and history. [Accessed 8 February 2017].
Available at: http://www.space.com

[14] Ciulla, G., Brano, V.L., Dio, V.D. and Cipriani, G. (2014). A comparison of different one diode models for the representation of iv characteristic of a {PV} cell. *Renewable and Sustainable Energy Reviews*, vol. 32, pp. 684 – 696. ISSN 1364-0321. [Accessed 10 April 2017].
Available at: `http://www.sciencedirect.com/science/article/pii/S136`

[15] Corfidi, S.F. (2014). The colors of sunset and twilight at noaanws storm prediction center. [Accessed 29 July 2017].
Available at: `http://www.spc.noaa.gov/publications/corfidi/sunset/`

[16] Corkish, R., Green, M.A., Watt, M.E. and Wenham, S.R. (2013). *Applied Photovoltaics*. Routledge. ISBN 9781844074013.

[17] Cornaro, C. and Andreotti, A. (2012 February). Influence of average photon energy index on solar irradiance characteristics and outdoor performance of pv modules. *Progress in Photovoltaics: Research and Applications*, , no. 00133, pp. 1–12.

[18] Corporation, S. (2010 March). Guide to interpreting i-v curve measurements of pv arrays. In: *Solmetric Application Note PVA-600-1*, pp. 1–23.

[19] CYS (2011). Cys-s0009 9g analog servo. [Accessed 22 May 2017].
Available at: `http://www.cysmodel.com/showproducty.asp`

[20] du Plessis, D. (2015 December). Design and development. pp. 1–200. [Accessed 2 August 2017].
Available at: `http://www.analog.com/en/products/analog-to-digital`

[21] Electric, S. (2013). 160 years of photovoltaic technology. [Accessed 13 April 2017].
Available at: `http://www.sunlightelectric.com/pvhistory.php`

[22] Energy, S. (2012). Renesola virtus ii. [Accessed 29 July 2017].
Available at: `https://solaray.com.au/renesola-virtus-ii/`

[23] Hamadani, B.H., Roller, J., Dougherty, B. and Yoon, H.W. (2013 June). Fast and reliable spectral response measurements of pv cells using light emitting diodes. In: *2013 IEEE 39th Photovoltaic Specialists Conference (PVSC)*, pp. 0073–0075. ISSN 0160-8371.

[24] Hansen, C.W. (2013 June). Estimation of parameters for single diode models using measured iv curves. In: *2013 IEEE 39th Photovoltaic Specialists Conference (PVSC)*, pp. 0223–0228. ISSN 0160-8371.

[25] Henderson, B. (2016). Blue skies and red sunsets. [Accessed 29 May 2017].
Available at: `http://www.physicsclassroom.com/class/light/Lesson`

[26] House, M. ().

[27] Inc., A. (2017). Autodesk inventor professional 2016. [Accessed 18 January 2017].
Available at: `https://www.autodesk.com/education/home`

[28] Installation, A. (2017). Advanced installation guide. [Accessed 13 February 2017].
Available at: `https://help.ubuntu.com/lts/serverguide/advanced.html`

[29] Ishaque, K., Salam, Z., Taheri, H. and Shamsudin, A. (2011 April). Parameter extraction of photovoltaic cell using differential evolution method. In: *2011 IEEE Applied Power Electronics Colloquium (IAPEC)*, pp. 10–15.

[30] Ishii, T., Otani, K., Itagaki, A. and Utsunomiya, K. (2013 April). A simplified methodology for estimating solar spectral influence on photovoltaic energy yield using average photon energy. *National Institute of Advanced Industrial Science and Technology (AIST)*, , no. 305-8568, pp. 18–26.

[31] Jason, A. (2017). Ubuntu server iso. [Accessed 13 June 2017].
Available at: `https://www.ubuntu.com/download/server`

[32] Joanna Lewis, A.S. and Tian, T. (2009 January). International motivations for solar photovoltaic market support: Findings from the united states, japan, germany and spain. In: *Prepared for the Center for Resource Solutions and the Energy Foundation China Sustainable Energy Program*, pp. 1–12.

[33] Krawczynski, M., Strobel, M.B., T.R.Betts and Gottschalg, R. (2010 March). Spectral influences on estimations of useful irradiance for different pv technologies. *Loughborough University Institutional Repository*, , no. 24-26th, p. 5.

[34] Laboratory, U.S.R.M. (2007). Sun path chart program. [Accessed 16 August 2017].
Available at: `http://solardat.uoregon.edu/SunChartProgram.html`

[35] Lineykin, S., Averbukh, M. and Kuperman, A. (2014). An improved approach to extract the single-diode equivalent circuit parameters of a photovoltaic cell/panel. *Renewable and Sustainable Energy Reviews*, vol. 30, pp. 282 – 289. ISSN 1364-0321. [Accessed 15 March 2017].
Available at: `http://www.sciencedirect.com/science/article/pii/S136`

[36] LLC, A. (2017). Altium designer 13.
Available at: `http://www.altium.com/`

[37] Louwen, A., de Waal, A.C., Schropp, R.E.I., Faaij, A.P.C. and van Sark, W.G.J.H.M. (2017). Comprehensive characterisation and analysis of pv module performance under real operating conditions. *Progress in Photovoltaics: Research and Applications*, vol. 25, no. 3, pp. 218–232. ISSN 1099-159X. Pip.2848.
Available at: `http://dx.doi.org/10.1002/pip.2848`

[38] Lugue, A. and Hegedus, S. (2003). *Handbook of Photovoltaic Science and Engineering*. Wiley. ISBN 0471491969.

[39] Ma, X., Bader, S. and Oelmann, B. (2016 November). Solar panel modelling for low illuminance indoor conditions. In: *2016 IEEE Nordic Circuits and Systems Conference (NORCAS)*, pp. 1–6.

[40] Majdoul, R., Abdelmounim, E., Aboulfatah, M., Touati, A.W., Moutabir, A. and Abouloifa, A. (2015 March). Combined analytical and numerical approach to determine the four parameters of the photovoltaic cells models. In: *2015 International Conference on Electrical and Information Technologies (ICEIT)*, pp. 263–268.

[41] Masters, G.M. (2013). *Renewable and Efficient Electric Power Systems*. Wiley.

[42] Meintjies, J. (2016). Stellenbosch weather. [Accessed 26 July 2017].
Available at: `http://weather.sun.ac.za/`

[43] Messenger, R. and Abtahi, A. (2010). *Photovoltaic Systems Engineering, Third Edition*. CRC Press.

[44] Miller, M., Martinot, E., Cox, S., Speer, B., Zinaman, O., Booth, S., Zissler, R., Cochran, J., Soonee, S., Audinet, P., Munuera, L. and Arent, D. (2015 04). Status report on power system transformation.

[45] Mutiara, L., Pegels, K. and Reinders, A. (2015 June). Evaluation of spectrally distributed irradiance in the netherlands regarding the energy performance of various pv technologies. In: *2015 IEEE 42nd Photovoltaic Specialist Conference (PVSC)*, pp. 1–6.

[46] Ndapuka, A.T. (2015 December). Design and development of a monitoring station for the long-term investigation of dust pollution effects on the performance of pv panels. pp. 1–139. [Accessed 14 August 2017].
Available at: `http://scholar.sun.ac.za/handle/10019.1/97823`

[47] Nells, M. (8 February 2017). Solar irradiance. *National Geographic*. [Accessed 8 February 2017].
Available at: `http://science.nationalgeographic.com/science/space/`

[48] Nofuentes, G., Gueymard, C., Aguilera, J., PÃ©rez-Godoy, M. and Charte, F. (2017). Is the average photon energy a unique characteristic of the spectral distribution of global irradiance? *Solar Energy*, vol. 149, pp. 32 – 43. ISSN 0038-092X. [Accessed 2 July 2017].
Available at: `http://www.sciencedirect.com/science/article/pii/S0038`

[49] Norton, M., Amillo, A.G. and Galleano, R. (2015 June). Comparison of solar spectral irradiance measurements using the average photon energy parameter. *European Commission, Joint Research Centre*, vol. 21027, no. 2749, pp. 338–344.

[50] Paul, C.R. (2000). *Fundamentals of Circuit Analysis*. Wiley. ISBN 0471371955.

[51] Plessis, A.D. (2014 March). The influence of dust soiling on the performance of photovoltaic modules in the semi-arid areas of south africa. pp. 1–220.
Available at: `http://scholar.sun.ac.za/handle/10019.1/101028`

[52] Russo, J.M., Zhang, D., Gordon, M., Vorndran, S., Wu, Y. and Kostuk, R.K. (2014 March). Spectrum splitting metrics and effect of filter characteristics on photovoltaic system performance. *Department of Electrical and Computer Engineering The University of Arizona*, , no. S2 Vol 22, pp. 10–26.

[53] Sampaio, P. and GonzÃ¡lez, M. (2017 07). Photovoltaic solar energy: Conceptual framework. vol. 74, pp. 590–601.

[54] Sara, I., Betts, T.R. and Gottschalg, R. (2013). Determining spectral response of a photovoltaic device using polychromatic filters. *Proceedings of the 9th Photovoltaic Science, Application and Technology (PVSAT) Conference*, vol. 8, no. 5, pp. 463–473. ISSN 10.1049.

[55] Sauer, K.J., Roessler, T. and Hansen, C.W. (2015 January). Modeling the irradiance and temperature dependence of photovoltaic modules in pvsyst. *IEEE Journal of Photovoltaics*, vol. 5, no. 1, pp. 152–158. ISSN 2156-3381.

[56] Sera, D., Teodorescu, R. and Rodriguez, P. (2007 June). Pv panel model based on datasheet values. In: *2007 IEEE International Symposium on Industrial Electronics*, pp. 2392–2396. ISSN 2163-5137.

[57] Soto, W.D., Klein, S. and Beckman, W. (2006). Improvement and validation of a model for photovoltaic array performance. *Solar Energy*, vol. 80, no. 1, pp. 78 – 88. ISSN 0038-092X. [Accessed 15 February 2017].
Available at: `http://www.sciencedirect.com/science/article/pii/S003`

[58] Total, P.E. (2017). The growth of photovoltaic solar around the world. [Accessed 12 April 2017].
Available at: `http://www.planete-energies.com/en/medias/close/growth`

[59] Vashishtha, D.S. (2012). Differentiate between the dni, dhi and ghi. *Firstgreen Energy*. [Accessed 27 August 2017].
Available at: `https://firstgreenconsulting.wordpress.com/2012/04/26/`

[60] Villalva, M.G., Gazoli, J.R. and Filho, E.R. (2009 May). Comprehensive approach to modeling and simulation of photovoltaic arrays. *IEEE Transactions on Power Electronics*, vol. 24, no. 5, pp. 1198–1208. ISSN 0885-8993.

[61] w3schools.com (2017). Sql tutorial. [Accessed 8 February 2017].
Available at: `https://www.w3schools.com/sql/default.asp`

[62] Weather2 (2017). Historical monthly averages for june in stellenbosch. [Accessed 18 August 2017].
Available at: `http://www.myweather2.com/City-Town/South-Africa/`

[63] Weisstein, E.W. (2007 June). Newton's method. In: *MathWorld*, pp. 95–104.
Available at: `http://mathworld.wolfram.com/NewtonsMethod.html`

[64] Wesoff, E. (2017 April). Iea: Global installed pv capacity leaps to 303 gigawatts. vol. 27, pp. 1–2.

[65] Yetayew, T.T. and Jyothsna, T.R. (2013 December). Improved single diode modeling approach for photovoltaic modules using data sheet. In: *2013 Annual IEEE India Conference (INDICON)*, pp. 1–6. ISSN 2325-940X.

[66] Zell, H. (31 July 2015). Solar irradiance. *NASA*. [Accessed 7 July 2017].
Available at: `https://www.nasa.gov/missionpages/sdo/science/solar.html`